

# Search for direct production of sleptons in proton-proton collisions at $\sqrt{s} = 13$ TeV with the ATLAS detector

Even Simonsen Håland



Thesis submitted for the degree of  
Master in Subatomic Physics  
60 credits

Department of Physics  
Faculty of mathematics and natural sciences

UNIVERSITY OF OSLO

Spring 2017



# Search for direct production of sleptons in proton-proton collisions at $\sqrt{s} = 13$ TeV with the ATLAS detector

Even Simonsen Håland

© 2017 Even Simonsen Håland

Search for direct production of sleptons in proton-proton collisions at  $\sqrt{s} = 13$  TeV with the ATLAS detector

<http://www.duo.uio.no/>

Printed: Reprocentralen, University of Oslo

# Abstract

The Standard Model of particle physics is currently the best theory for describing elementary particles and their interactions, but there are several problems and open questions related to it. For instance it does not incorporate gravity, and it does not explain dark matter, hence there is a need for new fundamental theories of nature beyond the current theory. A theory that addresses some of the problems with the Standard Model is Supersymmetry, as a symmetry between fermions and bosons, which predicts a superpartner for each Standard Model particle.

The work done in this thesis is a search for direct production of sleptons, which are the supersymmetric partners of the leptons. The sleptons are assumed to decay to leptons and neutralinos, where the latter is considered to be a good dark matter candidate particle. The data set used in this analysis consists of an integrated luminosity of  $36.1 \text{ fb}^{-1}$  from proton-proton collisions at 13 TeV centre-of-mass energy collected by the ATLAS experiment at the Large Hadron collider at CERN in 2015 and 2016. No significant excess above the expected Standard Model background is observed.



# Acknowledgements

When I started at this masters degree, the LHC had just started running after being upgraded, and for the last two years the ATLAS experiment has collected data beyond expectations. Taking this into account, the timing of this thesis couldn't possibly have been better. I have found the work with the thesis extremely interesting, I have certainly learned a lot, and several people deserves to be acknowledged for making this a great experience.

First of all I would like to give a huge thanks to my main supervisor, Farid Ould-Saada, for suggesting a very nice, interesting and challenging project, for sharing his profound knowledge and experience, and for always pushing the analysis and the thesis in the right direction. A great thanks should also be given to my second supervisor, Eirik Gramstad, for always having a solution to my analysis problems, for good answers to all my questions, and for having written a very nice PhD thesis which I continuously consulted for inspiration and tips. It has been a pleasure working with both of you, Farid and Eirik!

I would like to give a general thanks to the HEPP group at UiO, for being a nice and funny group to be part of as a master student! In particular I would like to thank Knut Oddvar Høie Vadla, whom I have interrupted an endless number of times with questions about software as well as analysis approach and physics, and who has always given patient and helpful answers. I would also like to thank my fellow master students, Anders Huse Pedersen and Anne-Marthe Hovda, for many nice discussions and good cooperation, both during the work with the courses and the work with our master theses.

I would also like to mention my friends back in my beautiful home place Klepp in Rogaland. It is always enjoyable to come home and get my mind drawn away from particle physics and analysis code for a moment.

Last but not least I would like to thank my parents, who are always supportive, both of my educational choices and otherwise.



# Contents

<b>Introduction</b>	<b>12</b>
<b>Notation and Conventions</b>	<b>14</b>
<b>1 The Standard Model</b>	<b>16</b>
1.1 The content of the Standard Model . . . . .	16
1.1.1 Forces . . . . .	17
1.1.2 Fermions . . . . .	18
1.1.3 Symmetries and conservation laws . . . . .	19
1.2 Quantum Field Theory . . . . .	20
1.2.1 Lagrangian formalism . . . . .	21
1.2.2 The gauge principle . . . . .	21
1.2.3 Interpretation of the Lagrangian . . . . .	22
1.3 Quantum Chromodynamics . . . . .	23
1.4 Glashow-Weinberg-Salam Theory . . . . .	24
1.4.1 Chirality and the gauge group . . . . .	24
1.4.2 Applying the gauge principle . . . . .	26
1.4.3 Spontaneous symmetry breaking . . . . .	27
1.4.4 Brout-Englert-Higgs mechanism . . . . .	29
1.4.5 The full GWS Lagrangian . . . . .	32
1.5 Limitations of the Standard Model . . . . .	33
<b>2 Supersymmetry</b>	<b>36</b>
2.1 Introduction to Supersymmetry . . . . .	36
2.2 The Minimal Supersymmetric Standard Model . . . . .	37
2.2.1 Soft SUSY breaking . . . . .	39
2.3 Direct slepton production . . . . .	40
<b>3 Proton-Proton Collisions</b>	<b>43</b>
3.1 Kinematics . . . . .	43
3.1.1 The two particle collision . . . . .	44
3.1.2 The products of the collision . . . . .	45
3.2 Proton-Proton interactions . . . . .	46
3.2.1 Parton distribution functions . . . . .	48
3.2.2 Hadronization . . . . .	48
3.3 Luminosity and pile-up . . . . .	49

<b>4 The Large Hadron Collider and the ATLAS experiment</b>	<b>51</b>
4.1 CERN . . . . .	51
4.2 The Large Hadron Collider . . . . .	52
4.3 The ATLAS detector . . . . .	53
4.3.1 Inner detector . . . . .	55
4.3.2 Calorimeters . . . . .	57
4.3.3 Muon spectrometer . . . . .	58
4.3.4 Magnets . . . . .	59
4.3.5 Trigger system . . . . .	60
<b>5 Direct Slepton Search Procedure</b>	<b>61</b>
5.1 Kinematics . . . . .	61
5.2 Object reconstruction and identification . . . . .	63
5.2.1 Electrons . . . . .	63
5.2.2 Muons . . . . .	64
5.2.3 Jets . . . . .	64
5.2.4 Missing transverse energy . . . . .	66
5.3 Object definitions . . . . .	66
5.3.1 Electrons . . . . .	66
5.3.2 Muons . . . . .	66
5.3.3 Jets . . . . .	67
5.3.4 Missing $E_T$ . . . . .	68
5.3.5 Overlap removal . . . . .	68
5.4 Data files and software tools . . . . .	68
5.5 SUSY signal samples . . . . .	70
5.6 Standard Model backgrounds . . . . .	70
5.6.1 $Z + \text{jets}$ . . . . .	71
5.6.2 Di-bosons . . . . .	72
5.6.3 $V + \gamma$ . . . . .	73
5.6.4 Drell-Yan . . . . .	73
5.6.5 $t\bar{t}$ . . . . .	74
5.6.6 $W + \text{jets}$ . . . . .	75
5.6.7 Single top . . . . .	75
5.6.8 $t\bar{t} + V$ . . . . .	76
5.6.9 Higgs . . . . .	76
5.6.10 Tri-bosons . . . . .	77
5.6.11 Fake leptons . . . . .	78
5.6.12 Weighting and scaling . . . . .	78
5.7 Baseline selection . . . . .	79
5.8 Pre-selection . . . . .	81
5.9 Comparison of Sherpa versions . . . . .	82
<b>6 Results of the Search for Direct Production of Sleptons</b>	<b>86</b>
6.1 How to interpret results . . . . .	86
6.1.1 Significance . . . . .	87
6.1.2 Exclusion . . . . .	88

6.2	Final selection and definition of signal regions . . . . .	88
6.2.1	Inclusive SRs . . . . .	89
6.2.2	Optimisation of inclusive SRs . . . . .	93
6.2.3	Exclusive SRs . . . . .	99
6.3	Background estimation . . . . .	103
6.3.1	Control regions . . . . .	104
6.3.2	Fake background estimation . . . . .	107
6.3.3	Validation regions . . . . .	108
6.4	Results . . . . .	110
6.4.1	Inclusive SRs . . . . .	111
6.4.2	Exclusive SRs . . . . .	112
6.4.3	Concluding remarks . . . . .	112
<b>Summary and Conclusions</b>		<b>114</b>
<b>A Lists of MC samples</b>		<b>115</b>
A.1	Background samples . . . . .	115
A.2	Signal samples . . . . .	120
<b>Bibliography</b>		<b>121</b>

# Introduction

The Standard Model of particle physics [1, 2, 3, 4, 5, 6], which was developed between the early 1960s and the mid 1970s, is a theoretical framework that describes matter particles (quarks and leptons) and the fundamental forces mediated by gauge bosons. The theory has been incredibly successful in explaining observations made in particle physics experiments, as well as predicting the existence of undiscovered particles. The last and perhaps most famous success of the Standard Model was the discovery of the Higgs boson by the ATLAS [20] and CMS [21] experiments at CERN. This discovery completed the Standard Model, in the sense that all the particles it predicts now have been discovered.

Despite the enormous success of the Standard Model there is an urgent need for new theories of Nature, because it does not include numerous known phenomena. The simplest example is gravity, which is well described by General Relativity at macroscopic scales, but is not at all understood at the quantum level. A so-called *theory of everything* is expected to unify the Standard Model and General Relativity. Another disturbing fact is that the Standard Model only describes about 5% of the observable universe, while the rest is dark matter ( $\sim 25\%$ ) and dark energy ( $\sim 70\%$ ) [7], which are both some of the great puzzles of physics. In particular dark matter is at the moment a very "hot" topic amongst both experimental and theoretical physicists.

A possible way to extend the Standard Model is through Supersymmetry, which predicts that for every known particle there exists another particle that has not yet been discovered. Supersymmetry, which relates fermions and bosons, is a very attractive theory, in the sense that it for instance solves the *hierarchy problem* [8] in a natural way, and it also provides a candidate particle for dark matter.

The data analysis performed in this master thesis presents a search for *sleptons*, which are the supersymmetric partners of the leptons. The sleptons are assumed to decay to leptons and another supersymmetric particle called the neutralino, which is a candidate particle for dark matter. The analysis is done by using  $36.1 \text{ fb}^{-1}$  of data collected by the ATLAS experiment from 13 TeV center-of-mass energy proton-proton collisions at the Large Hadron Collider at CERN in 2015 and 2016.

In the first two chapters of the thesis an introduction to the necessary theoretical framework is given. Chapter 1 introduces the particles and forces of the Standard Model in a qualitative way, before moving to a more mathematical approach, and an introduction to the gauge groups of the Standard Model, as well as the Brout-Englert-Higgs mechanism. Chapter 2 gives a brief introduction to Supersymmetry, with emphasis on its particle content and why it is (for many people) a preferred theory. The process that is targeted by the analysis is also introduced in this

chapter.

In Chapter 3 and 4 we start moving towards the experimental part of the thesis. Chapter 3 gives an overview of the kinematics and phenomenology of proton-proton collisions, while Chapter 4 describes the experimental set-up, namely the Large Hadron Collider and the ATLAS detector.

Chapter 5 describes all the "ingredients" that are prerequisites of the analysis. This includes kinematic variables, reconstruction and definition of objects (i.e. electrons, muons and jets), a first selection of events, as well as a discussion of the different Standard Model backgrounds considered in the analysis. At last, Chapter 6 details the analysis procedure, which includes sensitivity studies, background estimation, and finally the results of the search.

# Notation and Conventions

In the following the most relevant notation and conventions used in the thesis are listed, along with definitions of some important matrices.

- **Natural units:** Quantities in particle physics are given in natural units, which means that  $\hbar = c = 1$ , where  $\hbar$  is Planck's constant and  $c$  is the speed of light. In these units energy, momentum and mass are all given in electronvolts (eV), usually with some prefix, i.e. MeV or GeV.
- **Vectors:** Three-vectors are written in bold symbols, i.e.  $\mathbf{x} = (x, y, z)$  for spatial coordinates and  $\mathbf{p} = (p_x, p_y, p_z)$  for momentum. The contravariant (Lorentz) four-vectors for space-time and momentum are given by

$$x = x^\mu = (t, \mathbf{x}) \quad \text{and} \quad p = p^\mu = (E, \mathbf{p}),$$

where  $t$  is time and  $E$  is energy, and  $\mu = 0, 1, 2, 3$ . For a general contravariant four-vector,  $a^\mu$ , the corresponding covariant vector,  $a_\mu$ , is given by

$$a_\mu = g_{\mu\nu} a^\nu,$$

where  $g_{\mu\nu}$  is the Minkowski metric given by

$$g_{\mu\nu} = \begin{pmatrix} 1 & 0 & 0 & 0 \\ 0 & -1 & 0 & 0 \\ 0 & 0 & -1 & 0 \\ 0 & 0 & 0 & -1 \end{pmatrix}.$$

- **Time:** In Feynman diagrams the direction of time is from left to right.
- **Dirac matrices:** The Dirac gamma matrices,  $\gamma^\mu$ , which are commonly used in the mathematical formulation of the Standard Model, are given by

$$\gamma^0 = \begin{pmatrix} 1 & 0 & 0 & 0 \\ 0 & 1 & 0 & 0 \\ 0 & 0 & -1 & 0 \\ 0 & 0 & 0 & -1 \end{pmatrix}, \quad \gamma^1 = \begin{pmatrix} 0 & 0 & 0 & 1 \\ 0 & 0 & 1 & 0 \\ 0 & -1 & 0 & 0 \\ -1 & 0 & 0 & 0 \end{pmatrix},$$

$$\gamma^2 = \begin{pmatrix} 0 & 0 & 0 & -i \\ 0 & 0 & i & 0 \\ 0 & i & 0 & 0 \\ -i & 0 & 0 & 0 \end{pmatrix}, \quad \gamma^3 = \begin{pmatrix} 0 & 0 & 1 & 0 \\ 0 & 0 & 0 & -1 \\ -1 & 0 & 0 & 0 \\ 0 & 1 & 0 & 0 \end{pmatrix},$$

and the fifth gamma matrix,  $\gamma^5$ , is defined as

$$\gamma^5 \equiv i\gamma^0\gamma^1\gamma^2\gamma^3.$$

- **Gell-Mann matrices:** When considering Quantum Chromodynamics we run into the eight Gell-Mann matrices,  $\lambda^a$ , which are given by

$$\begin{aligned}\lambda^1 &= \begin{pmatrix} 0 & 1 & 0 \\ 1 & 0 & 0 \\ 0 & 0 & 0 \end{pmatrix}, & \lambda^2 &= \begin{pmatrix} 0 & -i & 0 \\ i & 0 & 0 \\ 0 & 0 & 0 \end{pmatrix}, & \lambda^3 &= \begin{pmatrix} 1 & 0 & 0 \\ 0 & -1 & 0 \\ 0 & 0 & 0 \end{pmatrix}, \\ \lambda^4 &= \begin{pmatrix} 0 & 0 & 1 \\ 0 & 0 & 0 \\ 1 & 0 & 0 \end{pmatrix}, & \lambda^5 &= \begin{pmatrix} 0 & 0 & -i \\ 0 & 0 & 0 \\ i & 0 & 0 \end{pmatrix}, & \lambda^6 &= \begin{pmatrix} 0 & 0 & 0 \\ 0 & 0 & 1 \\ 0 & 1 & 0 \end{pmatrix}, \\ \lambda^7 &= \begin{pmatrix} 0 & 0 & 0 \\ 0 & 0 & -i \\ 0 & i & 0 \end{pmatrix}, & \lambda^8 &= \frac{1}{\sqrt{3}} \begin{pmatrix} 1 & 0 & 0 \\ 0 & 1 & 0 \\ 0 & 0 & -2 \end{pmatrix},\end{aligned}$$

- **Pauli matrices:** In the theory of electroweak interactions we need the Pauli matrices,  $\sigma$ , given by

$$\sigma_x = \begin{pmatrix} 0 & 1 \\ 1 & 0 \end{pmatrix}, \quad \sigma_y = \begin{pmatrix} 0 & -i \\ i & 0 \end{pmatrix}, \quad \sigma_z = \begin{pmatrix} 1 & 0 \\ 0 & -1 \end{pmatrix}.$$

# Chapter 1

## The Standard Model

When doing experimental physics it is important with a working understanding of the theory you are investigating. Therefore the first chapter of this thesis is devoted to an introduction to the Standard Model (SM) of particle physics, which today is the best available theory for describing elementary<sup>1</sup> particles and their interactions.

We will start with a simple and qualitative description of the particles and forces contained in the SM. However, to get the full picture of the SM it is necessary with an introduction to some elements from Quantum Field Theory (QFT), including the role of symmetries and the Lagrangian formalism. Then we move on to describing the structure of the SM in a somewhat more mathematical way, including the group structure of the SM and the Brout-Englert-Higgs mechanism. The chapter will be finished off by discussing some problems with the SM and the need for extensions.

For a more thorough introduction to particle physics than given in this chapter the reader is referred to refs. [9] and [10], while ref. [11] is recommended for a deeper introduction to QFT.

### 1.1 The content of the Standard Model

The particle content of the Standard Model is shown in Figure 1.1. Each particle is suited with a set of quantum numbers (where only a few of them are given in Figure 1.1), and they are often classified according to these quantum numbers. For instance, the particles can be divided in two groups based on their spin. Particles with integer spin are called *bosons*, while particles with half-integer spin are called *fermions*. The fermions are often referred to as "matter particles", since ordinary matter are made of (some of) these, while the bosons (with spin-1) are mediators of the forces described by the SM. The Higgs boson (with spin-0) has a somewhat special role related to how particles acquire their masses, which will be discussed more carefully in Section 1.4.4.

---

<sup>1</sup>The particles described by the SM are in this thesis referred to as elementary, even though we strictly speaking cannot know for sure that they really are elementary at some lower scale/higher energy. No experiment has indicated that they are not elementary, which means that this should be a safe assumption in this context.

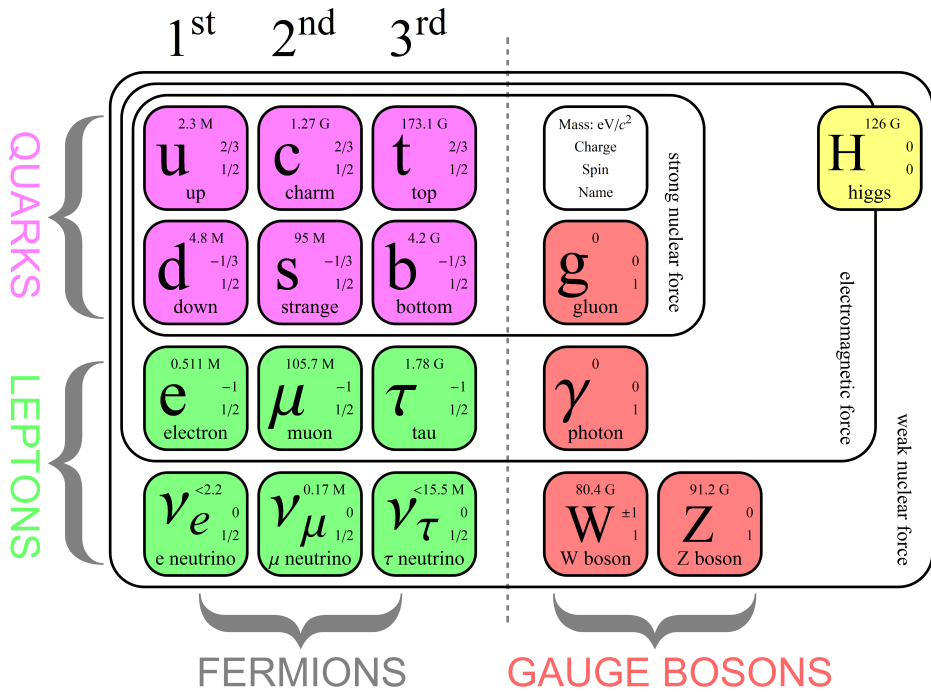


Figure 1.1: The content of the Standard Model, taken from ref. [12]

### 1.1.1 Forces

There are four fundamental forces of nature, of which three of them are described by the SM, namely the electromagnetic force, the strong force and the weak force. The only known fundamental force not described by the SM is gravity. On macroscopic scales gravity is well described by Einstein's General Theory of Relativity, but so far no one has managed to develop a successful theory of quantum gravity. Despite this it is a common assumption that gravity is also mediated by a boson often referred to as a *graviton*. However, compared to the other forces gravity is incredibly weak, and therefore negligible in the context of particle physics, unless some extra space-dimensions would show up at the LHC. This means that we can safely leave gravity at this stage, and rather move on to discussing the three other forces.

The only force apart from gravity that is important at macroscopic scales is the electromagnetic force, which is mediated by the photon,  $\gamma$ . The quantum number associated with the electromagnetic force is the electric charge,  $Q$ , thus only particles with  $Q \neq 0$  are able to interact electromagnetically. Particles with opposite electric charge attract each other, and it is this force that is responsible for holding electrons in place around the nucleus of an atom.

The weak interaction<sup>2</sup> is associated with the *weak isospin* quantum number,  $I_W$  (which will be more carefully discussed in Section 1.4), and is for several reasons a quite special interaction. For instance it is the only interaction capable of changing the flavour of a quark, which allows for nuclear  $\beta$ -decays. Also, the mediators ( $W^+$ ,

<sup>2</sup>The terms "interaction" and "force" are often used interchangeably. However, the weak force is *not* a force in the sense that it causes particles to repel/attract each other, hence "interaction" is a more precise term in this case.

$W^-$  and  $Z^0$ ) are heavy particles, whereas the mediators of the electromagnetic and strong forces are massless.

The strong force is responsible for binding quarks together to form particles like protons and neutrons, and it is also responsible for holding protons and neutrons together in a nucleus. It is mediated by eight different gluons. The characteristic quantum number of the strong interaction is colour charge,  $C$ .

It is worth noting that the bosons not only mediate interactions between fermions, but some of them can also interact with each other, which is referred to as gauge boson *self-interactions*. For instance the  $W^\pm$ -bosons are electrically charged, which means that they can interact electromagnetically, while gluons carry colour charge, which means that they can interact with each other via the strong force. On the other hand, photons are electrically neutral and cannot interact with each other. These differences arises from the underlying group structures of the different interactions, which will be discussed in Sections 1.2-1.4.

### 1.1.2 Fermions

Now that we have mentioned the different forces and the bosons they are mediated by, it is time to move on to the fermions. It has already been mentioned that they all are spin- $\frac{1}{2}$  particles, but, as indicated in Figure 1.1, it is possible to further divide the fermions into two groups, namely *quarks* and *leptons*. They can both be separated into three different *generations* with two particles in each generation differing by 1 unit in electric charge.

Before we go into further details about quarks and leptons we should mention that all particles, both fermions and bosons, are accompanied by antiparticles. An antiparticle has the same mass as the particle, but opposite electric charge and other additive quantum numbers. Neutral particles could then in principle be identical to their antiparticles, which is indeed the case for some bosons such as  $\gamma$  and  $Z^0$ . Fermions that act as their own antiparticles are called *Majorana* fermions. The only Majorana candidates in the SM are the neutrinos, but it is in fact not clear whether or not they actually are Majorana particles or Dirac particles, for which the latter implies that particles and anti-particles are distinct.

#### Quarks

The quarks are the fermions that carry colour charge, which means that they are able to interact via the strong force. There are six different quarks (or quark flavours) named *up* ( $u$ ), *down* ( $d$ ), *charm* ( $c$ ), *strange* ( $s$ ), *top* ( $t$ ) and *bottom* ( $b$ ). They come in three different colours<sup>3</sup>; red ( $r$ ), green ( $g$ ) and blue ( $b$ ). (Anti-quarks carry anti-colour, denoted by  $\bar{r}$ ,  $\bar{g}$ , and  $\bar{b}$ .) However, the nature of the strong force is such that coloured objects are not "allowed" in nature, hence quarks have never been observed as free particles, but rather in colorless multi-particle states called *hadrons*. Colourlessness can be achieved either by combining three (anti-)quarks with different (anti-)colours (i.e.  $rgb$  or  $\bar{r}\bar{g}\bar{b}$ ), or by combining colour with anti-colour

---

<sup>3</sup>Note that the term "colour" has nothing to do with actual colours. It is just a name given to the property that make particles able to feel the strong force.

(i.e.  $r\bar{r}$ ,  $g\bar{g}$  or  $b\bar{b}$ ). Three-particle states are called *baryons*, while two-particle states are referred to as *mesons*. The most famous examples of hadrons are the proton ( $uud$ ) and the neutron ( $udd$ ), which make up the atomic nuclei.

The only quark that can be observed as a free particle is the top quark, which is the heaviest of the SM particles. Because of its large mass its average lifetime is shorter than the average interaction time of the strong interaction, meaning that it will typically decay after  $\sim 10^{-25}$  s, before getting a chance to form hadronic states.

## Leptons

The leptons are the fermions that do not carry colour charge. Each generation consists of a charged lepton ( $e$ ,  $\mu$  or  $\tau$ ) and the associated neutrino flavour eigenstate ( $\nu_e$ ,  $\nu_\mu$  or  $\nu_\tau$ ). Of the charged leptons the electron is the only one that is stable, while muons and taus relatively quickly decay via the weak interaction, hence all the matter we are surrounded by is made entirely out of three particles; the electron, and the  $u$ - and  $d$ -quarks.

Strictly speaking we are also surrounded by *a lot* of neutrinos, but the neutrinos only interact by the weak interaction, meaning that they mostly just pass through what ever comes in their way. For this reason neutrinos are very hard to study experimentally, and there are several unsolved "mysteries" related to the neutrinos. One of these is the already mentioned issue of whether or not they are Majorana particles.

Some other open questions are related to the neutrino masses. For a long time it was believed that they were massless. This was proved not to be the case when *neutrino oscillations* were discovered in 1998 [13], a phenomenon that makes it possible for a neutrino to turn into another flavour eigenstate, i.e. a neutrino created as  $\nu_e$  can later show up as  $\nu_\mu$ . This is *only* possible if each flavour eigenstate is a mix of different mass eigenstates (denoted  $\nu_1$ ,  $\nu_2$  and  $\nu_3$ ), and the mass differences between these eigenstates are non-zero, hence the observation of neutrino oscillations is direct evidence that the neutrinos are not massless. Exactly what the masses are, which of the mass eigenstates are the heaviest and lightest, and whether the leptonic sector exhibit CP-violation as the quark sector, are still not fully understood.

### 1.1.3 Symmetries and conservation laws

The interactions and dynamics of the particles are governed by different symmetries and conservation laws, and the most important ones should be mentioned here.

First of all, like in classical (Newtonian) physics, energy,  $E$ , and three-momentum,  $\mathbf{p}$ , are conserved, as well as the total angular momentum,  $J$ . A ground breaking result from Special Relativity is however that (rest) mass,  $m$ , is not conserved, which is the reason why we are able to produce heavier particles than we started out with in particle colliders.

A fundamental result of Quantum Field Theory is that all physical processes are symmetric under *CPT*-transformations, which is the combination of charge conjugation ( $C$ ; particle $\rightarrow$ antiparticle), parity ( $P$ ;  $\mathbf{x} \rightarrow -\mathbf{x}$ ) and time-reversal ( $T$ ;  $t \rightarrow -t$ ). Strong and electromagnetic interactions also respects  $C$ -,  $P$ -,  $T$ - and  $CP$ -symmetries, while these are found to be violated by the weak interactions.

Each of the different interactions is also closely related to conservation of a certain quantum number, which arises from the gauge symmetries that will be discussed in the next sections. In fact these quantum numbers have already been mentioned. For electromagnetic interactions it is the electric charge, for weak interactions it is the weak isospin and for strong interactions it is the colour charge.

The last conservation laws we should mention are conservation of baryon number,  $B$ , and lepton number,  $L_x$ , where  $x$  denotes the lepton flavour. Baryons are assigned  $B = 1$ , anti-baryons  $B = -1$  and everything else (including mesons) have  $B = 0$ . Consequently quarks have  $B = \frac{1}{3}$  and anti-quarks  $B = -\frac{1}{3}$ . The total baryon number is always conserved in an interaction.

Lepton numbers are assigned depending on the lepton flavour, i.e. the  $e^-$  and  $\nu_e$  have  $L_e = 1$ , while  $e^+$  and  $\bar{\nu}_e$  have  $L_e = -1$ . All other particles have  $L_e = 0$ , and similarly for  $L_\mu$  and  $L_\tau$ . Each of these lepton numbers is conserved in any interaction. An exception to this rule arises from neutrino oscillations, since neutrinos are able to oscillate from one flavour to another. However, such oscillations take place over large distances, which means that the effect is infinitely small at the scale of particle interactions.

## 1.2 Quantum Field Theory

Quantum Field Theory (QFT) is the unification of Quantum Mechanics (QM) and Special Relativity (SR). In a very simplified way we can say that QM deals with "small things" (i.e. atoms and elementary particles), while SR deals with "fast moving things" (i.e.  $v \rightarrow c$ ). When doing high energy particle physics we need to describe "small and fast moving things", hence we need both QM and SR. However, when trying to unify these two theories we soon run into several problems. For instance, the Schrödinger equation, which is the basic equation of QM, is not Lorentz invariant. We also get problems such as violation of causality, negative energy states and no possibility for creation of other particles. These issues are obviously very troubling, but they can be solved by taking some relatively simple actions, which can be summarized in the following two bullet points:

- **New equations:** The Schrödinger equation must be replaced by Lorentz invariant equations, namely the Klein-Gordon equation (for scalar particles) and the Dirac equation (for spin- $\frac{1}{2}$  particles).
- **Fields:** Instead of considering particles as point-like objects (which is the QM approach) we must consider them as *fields*, and give up the notion of empty vacuum.

These are the basic steps in the transition from QM to QFT, and we are now ready to start studying relativistic particles, and develop specific QFTs for different particles and their interactions. Throughout the rest of this section we will have a look at some of the most important features in the development of such theories. In doing so we will adopt the simplest QFT as an example, namely Quantum Electrodynamics (QED), which describes the electromagnetic interaction among fermion fields.

### 1.2.1 Lagrangian formalism

When studying field theory the Lagrangian formalism is very practical to use. In classical mechanics the Lagrangian,  $L$ , is defined as  $L = T - U$ , where  $T$  and  $U$  are the kinetic and potential energies. For a general coordinate,  $q$ , the equation of motion is found by using the Euler-Lagrange equation

$$\frac{d}{dt} \left( \frac{\partial L}{\partial \dot{q}} \right) - \frac{\partial L}{\partial q} = 0. \quad (1.1)$$

The Euler-Lagrange equation can be obtained by minimizing the action,  $S$ , defined as  $S = \int L dt$ . In field theory we work with the Lagrangian *density*,  $\mathcal{L}$ , which is a function of fields,  $\phi$ , and their derivatives,  $\partial_\mu \phi$ .  $L$  itself is the spacial integral over  $\mathcal{L}$ , hence the action can be written as

$$S = \int \mathcal{L}(\phi, \partial_\mu \phi) d^4x, \quad (1.2)$$

and the Euler-Lagrange equation becomes

$$\partial_\mu \left( \frac{\mathcal{L}}{\partial(\partial_\mu \phi)} \right) - \frac{\partial \mathcal{L}}{\partial \phi} = 0. \quad (1.3)$$

From now on we will *only* work with Lagrangian densities, so for simplicity  $\mathcal{L}$  will be referred to as the Lagrangian.

For a free fermion field,  $\psi = \psi(x)$ , the Lagrangian is given as

$$\mathcal{L} = \bar{\psi} (i\gamma^\mu \partial_\mu - m) \psi, \quad (1.4)$$

where the adjoint spinor  $\bar{\psi}$  is defined as  $\bar{\psi} = \psi^\dagger \gamma^0$ . The first term of Equation 1.4 is referred to as the kinetic term, while the second term is called the mass term. By inserting this in Equation 1.3 we arrive to the Dirac equation,

$$(i\gamma^\mu \partial_\mu - m) \psi = 0, \quad (1.5)$$

which is the equation of motion for a free fermion field.

### 1.2.2 The gauge principle

We are now capable of describing a free fermion field, so the question is now how we should proceed to obtain a theory that contains interactions. This is done by identifying a global gauge symmetry of the theory in question, which leaves the Lagrangian  $\mathcal{L}$  invariant, and then require  $\mathcal{L}$  to also stay invariant under the corresponding *local gauge transformation*. This is referred to as the *gauge principle*. Such transformations are described by symmetry groups, and the symmetry group related to a certain theory is called the *gauge group* of that theory.

The gauge group of QED is  $U(1)$ , which means that we must require Equation 1.4 to be invariant under a local  $U(1)$  transformation,

$$\psi \rightarrow e^{i\alpha(x)} \psi. \quad (1.6)$$

Because of the derivative in the kinetic term the Lagrangian is not invariant under this transformation, but this can be fixed by replacing the derivative by a so-called covariant derivative,

$$\partial_\mu \rightarrow D_\mu = \partial_\mu - ieA_\mu(x), \quad (1.7)$$

where we have introduced a vector field,  $A_\mu(x)$ , often referred to as a *gauge field*. In order to make the theory invariant we must require this field to transform as

$$A_\mu(x) \rightarrow A_\mu(x) + \frac{1}{e}\partial_\mu\alpha(x). \quad (1.8)$$

To complete the Lagrangian we must also add a gauge invariant kinetic term for  $A_\mu(x)$  which is constructed from the field strength tensor

$$F_{\mu\nu} = \partial_\mu A_\nu - \partial_\nu A_\mu. \quad (1.9)$$

The complete QED Lagrangian can then be written as

$$\mathcal{L}_{QED} = \bar{\psi}(i\gamma^\mu\partial_\mu - m)\psi + e\bar{\psi}\gamma^\mu\psi A_\mu - \frac{1}{4}F_{\mu\nu}F^{\mu\nu}. \quad (1.10)$$

### 1.2.3 Interpretation of the Lagrangian

The first term of the QED Lagrangian (Eq. 1.10), is the free fermion Lagrangian (Eq. 1.4). As already mentioned it is referred to as the kinetic and mass terms of the fermion field. In general, a kinetic term is quadratic (i.e. involves  $\psi$  and  $\bar{\psi}$ ) and involves first derivatives of the field, while a mass term is a quadratic term with no derivatives. The constant of the mass term is (not surprisingly) interpreted as the mass of the field.

The new field,  $A_\mu$ , is interpreted as the photon field, which is a massless field, since Equation 1.10 does not contain any mass terms for this field. Finally  $F_{\mu\nu}$  corresponds to the electromagnetic field strength tensor. Interesting to note is that by defining a four-vector current  $j^\mu = -e\bar{\psi}\gamma^\mu\psi$ , and using the Euler-Lagrange equation with derivatives with respect to  $A_\mu$ , we will actually arrive to Maxwell's equations,

$$\partial_\mu F^{\mu\nu} = j^\nu, \quad (1.11)$$

meaning that the whole theory of electromagnetism can be derived just from the requirement of local  $U(1)$  invariance, and all of Maxwell's equations are summarized in one equation!

The third term of the QED Lagrangian,  $e\bar{\psi}\gamma^\mu\psi A_\mu$ , is the only one involving both the fermion field and the photon field. This is the *interaction term*, which describes the interaction between these fields. The constant  $e$  is the elementary charge, and gives the coupling between the fields. It is related to the electric charge,  $q$ , of a particle by  $q = Qe$ , where  $Q$  is the charge quantum number.

The interaction is pictured as a Feynman graph in Figure 1.2, where  $f$  and  $\bar{f}$  are the charged fermion and anti-fermion respectively, and  $\gamma$  is the photon. Note that the vertex can be rotated to describe a (anti-)fermion emitting a photon, or to a photon splitting into  $f\bar{f}$ . All electromagnetic interactions can be described by combining these vertices.

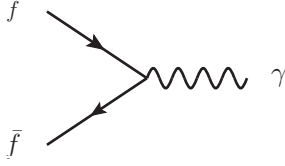


Figure 1.2: A basic QED vertex.

By using perturbation theory it is possible to derive so-called *Feynman rules*, which can be used to calculate the transition amplitude,  $\mathcal{M}$ , for a certain process. The resulting probability amplitude is further used to calculate cross-sections and decay rates. For this reason the Lagrangian (for a general theory) is extremely useful, since it allows us to see which interactions the theory permits, and how the fields are coupled to each other.

### 1.3 Quantum Chromodynamics

Quantum Chromodynamics (QCD) is the theory that describes the strong interaction. While QED is related to conservation of one single (electric) charge, QCD is related to conservation of three separately conserved (colour) charges, hence the gauge transformations must take place in the three dimensional colour space. The gauge group of QCD is therefore  $SU(3)_C$ , where the  $C$  stands for "colour". A local  $SU(3)$  transformation of  $\psi = \psi(x)$  is given by

$$\psi \rightarrow \exp \left[ ig_s \boldsymbol{\alpha}(x) \cdot \hat{\mathbf{T}} \right] \psi, \quad (1.12)$$

where  $g_s$  is the strong coupling constant,  $\hat{\mathbf{T}} = \{T^a\}$  are the eight generators ( $a = 1, 2, \dots, 8$ ) of  $SU(3)$  given by  $T^a = \frac{1}{2}\lambda^a$ , where  $\lambda^a$  are the Gell-Mann matrices. In order for Equation 1.4 to stay invariant under this transformation we must (as for QED) replace the derivative by a covariant derivative, which is now given by

$$D_\mu = \partial_\mu + ig_s G_\mu^a(x) T^a, \quad (1.13)$$

where we have introduced eight new gauge fields,  $G_\mu^a$ , which must transform as

$$G_\mu^k \rightarrow G_\mu^{k'} = G_\mu^k - \partial_\mu a_k - g_s f_{ijk} \alpha^i G_\mu^j, \quad (1.14)$$

where  $f_{ijk}$  are the so-called structure constants of  $SU(3)$ , which are defined from the commutation relation  $[\lambda_i, \lambda_j] = 2i f_{ijk} \lambda_k$ . Since this relation is non-zero we say that  $SU(3)$  is a *non-Abelian* group, or equivalently, that QCD is a non-Abelian gauge theory. This is a significant difference from QED (which is an Abelian theory), because it is this property that leads to self-interactions between the gauge fields of QCD. This can be seen from the field strength tensor, which is given as

$$G_{\mu\nu}^i = \partial_\mu G_\nu^i - \partial_\nu G_\mu^i - g_s f_{ijk} G_\mu^j G_\nu^k, \quad (1.15)$$

hence the kinetic term,  $-\frac{1}{4}G_{\mu\nu}G^{\mu\nu}$ , contains vertices with both three and four gauge fields.

The full QCD Lagrangian is given by

$$\mathcal{L}_{QCD} = \bar{\psi} (i\gamma^\mu \partial_\mu - m) \psi - g_s \bar{\psi} \gamma^\mu T_a \psi G_\mu^a - \frac{1}{4} G_{\mu\nu} G^{\mu\nu}, \quad (1.16)$$

where  $\psi$  now is a fermion field with colour charge (i.e. a quark field), and the gauge fields correspond to the eight gluon fields. The elementary Feynman vertices of QCD are shown in Figure 1.3, where  $q$  is a quark field and  $g$  is a gluon field.

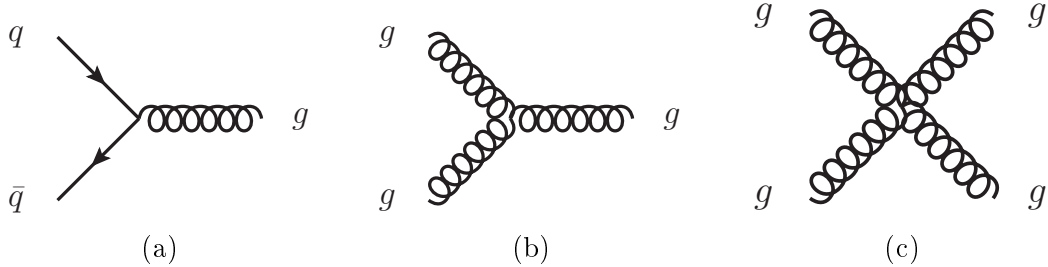


Figure 1.3: The elementary vertices of QCD.

As already mentioned the gluons carry colour charge, and since colour must be conserved in all interactions they must carry both colour and anti-colour at the same time. As we already know, there are eight different gluon fields, and in terms of colour they can be written as

$$r\bar{g}, g\bar{r}, r\bar{b}, b\bar{r}, g\bar{b}, b\bar{g}, \frac{1}{\sqrt{2}}(r\bar{r} - g\bar{g}) \text{ and } \frac{1}{\sqrt{6}}(r\bar{r} + g\bar{g} - 2b\bar{b}). \quad (1.17)$$

## 1.4 Glashow-Weinberg-Salam Theory

Instead of describing the weak interaction separately we will jump straight to the theory that describes the weak and the electromagnetic interaction in a unified way. This theory was developed by Glashow [1], Weinberg [2] and Salam [3] in the 1960's (which earned them the Nobel Prize in Physics in 1979), and is referred to as Glashow-Weinberg-Salam (GWS) theory, or just the *electroweak* theory. For several reasons, which will be discussed throughout the rest of this section, GWS theory is a lot more complicated than QCD and QED.

### 1.4.1 Chirality and the gauge group

The first complication we meet is that we have to take into account that fermion fields exist as left- and right-handed *chirality* states,  $\psi_L$  and  $\psi_R$ , given by

$$\psi_L = \frac{1 - \gamma_5}{2} \psi \quad \text{and} \quad \psi_R = \frac{1 + \gamma_5}{2} \psi, \quad (1.18)$$

where  $\psi$  is a fermion field. The nature of the weak interaction is such that only left-handed states couple to the  $W$ -boson. For this reason the previously mentioned

weak isospin,  $I_W$ , is introduced. Left-handed fermions have  $I_W = \frac{1}{2}$  and appears in isospin doublets, i.e.

$$\ell_L = \begin{pmatrix} \nu_\ell \\ \ell^- \end{pmatrix} \quad \text{or} \quad q_L = \begin{pmatrix} u \\ d \end{pmatrix},$$

while right-handed fermions have  $I_W = 0$  and are isospin singlets, i.e

$$\ell_R, u_R \text{ or } d_R.$$

Worth mentioning at this point is that the quarks in the weak isospin doublet are not exactly the same as the quarks described by QCD. The strongly interacting quarks are mass eigenstates, while the weakly interacting quarks are superpositions of the mass eigenstates. It is common practice to choose a basis such that only down-type quarks ( $d, s, b$ ) are mixed states, while the up-type quarks ( $u, c, t$ ) are both weak and strong eigenstates. The weak eigenstates of the down-type quarks are denoted  $d', s'$  and  $b'$ , and the mixing with the strong eigenstates is described by the Cabibbo-Kobayashi-Maskawa (CKM) matrix as

$$\begin{pmatrix} d' \\ s' \\ b' \end{pmatrix} = \begin{pmatrix} V_{ud} & V_{us} & V_{ub} \\ V_{cd} & V_{cs} & V_{cb} \\ V_{td} & V_{ts} & V_{tb} \end{pmatrix} \begin{pmatrix} d \\ s \\ b \end{pmatrix}, \quad (1.19)$$

where  $V_{xy}$  denotes the probability of a transition from quark type  $x$  to quark type  $y$  by emission or absorption of a charged  $W$ -boson.

The gauge group of the weak interaction is  $SU(2)_L$ , where the  $L$  indicates the "left-handedness" of this interaction. In order to unify the weak and the electromagnetic interaction we put  $SU(2)_L$  together with  $U(1)_Y$ , which is written as  $SU(2)_L \times U(1)_Y$ . From QED we are already familiar with  $U(1)$ , but now the electric charge is replaced by the *weak hypercharge*,  $Y$ . However, it turns out that  $Y$  and the third component of  $I_W$  are related to electric charge,  $Q$ , by

$$Q = \frac{Y}{2} + I_W^3. \quad (1.20)$$

Two particles in a weak isospin doublet have the same weak hypercharge ( $-1$  for leptons and  $\frac{1}{3}$  for quarks), and differ by one unit in weak isospin ( $\frac{1}{2}$  for neutrinos and up-type quarks, and  $-\frac{1}{2}$  for charged leptons and down-type quarks). For right-handed particles we have  $Q = \frac{Y}{2}$  since  $I_W = 0$ .

A local  $SU(2)_L \times U(1)_Y$  gauge transformation of  $\psi$  is written as

$$\psi \rightarrow \exp \left[ i \frac{Y}{2} \alpha(x) + i I_W \beta(x) \boldsymbol{\sigma} \right] \psi, \quad (1.21)$$

where  $\beta(x)$  is a three-dimensional function and  $\boldsymbol{\sigma}$  are the Pauli matrices, which generates  $SU(2)_L$  when they are multiplied by  $\frac{1}{2}$ .

### 1.4.2 Applying the gauge principle

Now we can once again apply the gauge principle. However, this doesn't work out quite as smoothly as in QED and QCD. Because the gauge transformation acts differently on left-handed and right-handed fields,

$$\psi_L \rightarrow \psi'_L = \exp \left[ i \frac{Y}{2} \alpha(x) + i I_W \boldsymbol{\beta}(x) \boldsymbol{\sigma} \right] \psi_L \quad (1.22)$$

and

$$\psi_R \rightarrow \psi'_R = \exp \left[ i \frac{Y}{2} \alpha(x) \right] \psi_R, \quad (1.23)$$

we must split the Lagrangian in parts, one for left-handed fermions and one for right-handed fermions. Because of this we must actually abandon the fermion mass term, since this term mixes left- and right-handed fields, and destroys gauge invariance. This is obviously a major problem, since we know for a fact that fermions are not massless. However, the problem has a solution which we will return to in Section 1.4.4, but for now let us continue applying the gauge principle, and see how it turns out.

The covariant derivative takes the form

$$D_\mu = \partial_\mu + ig' \frac{Y}{2} B_\mu(x) + ig I_W \boldsymbol{\sigma} \mathbf{W}_\mu(x), \quad (1.24)$$

where we have introduced one gauge field,  $B_\mu$ , corresponding to the  $U(1)_Y$  symmetry and three gauge fields,  $\mathbf{W}_\mu$ , corresponding to the  $SU(2)_L$  symmetry. These are however not the physical fields corresponding to the gauge bosons, which are mixed states given as

$$A_\mu = B_\mu \cos \theta_W + W_\mu^3 \sin \theta_W, \quad (1.25)$$

$$Z_\mu = -B_\mu \sin \theta_W + W_\mu^3 \cos \theta_W, \quad (1.26)$$

$$W_\mu^\pm = \frac{1}{\sqrt{2}} (W_\mu^1 \mp W_\mu^2), \quad (1.27)$$

for the photon, the  $Z$ -boson and the  $W^\pm$ -bosons respectively. The angle  $\theta_W$  is the *weak mixing angle*, which can only be determined experimentally, and relates the couplings  $g$  and  $g'$  to the elementary charge,  $e$ , by

$$e = g \sin \theta_W = g' \cos \theta_W. \quad (1.28)$$

The fields strength tensors for  $B_\mu$  and  $\mathbf{W}_\mu$  are given as

$$B_{\mu\nu} = \partial_\mu B_\nu - \partial_\nu B_\mu$$

and

$$\mathbf{W}_{\mu\nu} = \partial_\mu \mathbf{W}_\nu - \partial_\nu \mathbf{W}_\mu - g \mathbf{W}_\mu \times \mathbf{W}_\nu.$$

Using these to construct kinetic terms for the gauge fields we can write down a preliminary electroweak Lagrangian as

$$\begin{aligned}\mathcal{L}_{EW} = & \bar{\psi}_L \gamma^\mu \left[ i\partial_\mu - \frac{g}{2} \boldsymbol{\sigma} \mathbf{W}_\mu - \frac{g'Y}{2} B_\mu \right] \psi_L + \bar{\psi}_R \gamma^\mu \left[ i\partial_\mu - \frac{g'Y}{2} B_\mu \right] \psi_R \\ & - \frac{1}{4} B^{\mu\nu} B_{\mu\nu} - \frac{1}{4} \mathbf{W}^{\mu\nu} \mathbf{W}_{\mu\nu}.\end{aligned}\quad (1.29)$$

The elementary (physical) vertices of Equation 1.29 are given in Figure 1.4. The photon and the  $Z$ -boson couple to both left-handed and right-handed fermions, while  $W$ -bosons only couple to left-handed fermions. In addition to the fermion vertices we have some vertices involving only the gauge bosons, which comes from the last term of the Lagrangian. So, from the standard approach of applying the gauge principle we are actually able to describe the interactions between the fields, but as mentioned the Lagrangian does not contain fermion mass terms, as such terms would ruin the gauge invariance. Further more we know from experiments that the weak gauge bosons ( $Z, W^\pm$ ) also are massive, and adding mass terms for these would also destroy the gauge symmetry. Clearly a crucial part is missing for the theory to be satisfactory, and that part is the concept of *spontaneous symmetry breaking*, which allows us to include massive particles through the *Brout-Englert-Higgs (BEH) mechanism* [4, 5].

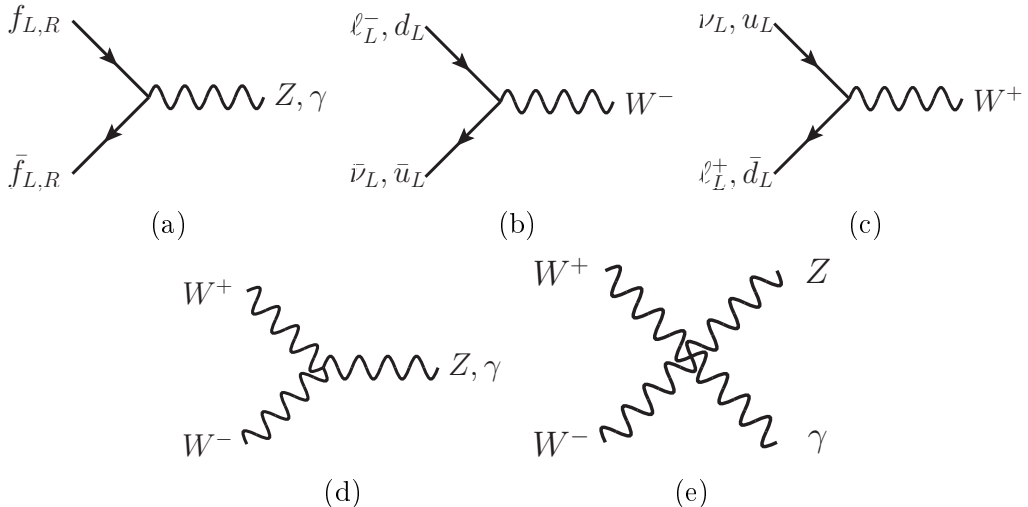


Figure 1.4: The elementary electroweak Feynman vertices.

### 1.4.3 Spontaneous symmetry breaking

#### Real scalar field

Assume that we have a real scalar field,  $\phi$ , and the Lagrangian describing this field is given as

$$\mathcal{L} = \frac{1}{2} (\partial_\mu \phi) (\partial^\mu \phi) - \mu^2 \phi^2 - \frac{1}{4} \lambda \phi^4,\quad (1.30)$$

with  $\lambda > 0$ . This means that we are dealing with a field with mass<sup>4</sup>  $\sqrt{2}\mu$  if  $\mu^2 > 0$ , and a quartic self-coupling term with coupling constant  $\lambda$ . Important to notice is also that the theory is invariant under the transformation  $\phi \rightarrow -\phi$ .

Remember that the Lagrangian is defined as kinetic terms minus potential terms, meaning that the potential is here given as

$$V(\phi) = \mu^2\phi^2 + \frac{1}{4}\lambda\phi^4. \quad (1.31)$$

The minimum of the potential is referred to as the *vacuum expectation value* of the field, and is found at  $\phi = 0$ .

Assume in the following that  $\mu^2 < 0$ . The potential and the Lagrangian are still symmetric under  $\phi \rightarrow -\phi$ , but we have introduced two important changes to the theory: The quadratic term can no longer be interpreted as a mass term, and the vacuum expectation value is now at  $\phi = \pm\frac{\mu}{\lambda}$ . To be able to do perturbation theory we must express the field by deviations from a ground state, meaning a state with vacuum expectation value at zero. This can be achieved by introducing a new field,  $\eta$ , defined as<sup>5</sup>

$$\eta \equiv \phi \pm \frac{\mu}{\lambda}. \quad (1.32)$$

The Lagrangian then becomes

$$\mathcal{L} = \frac{1}{2}(\partial_\mu\eta)(\partial^\mu\eta) - \mu^2\eta^2 \pm \mu\lambda\eta^3 - \frac{1}{4}\lambda\phi^4 \quad (1.33)$$

which now describes a field with mass  $\sqrt{2}\mu$  and two self-coupling terms. (Strictly speaking the Lagrangian also gets a constant term involving only  $\mu$  and  $\lambda$ , but such terms are always ignored because they will never contribute to the equations of motion.) This Lagrangian is **no longer symmetric** under the field transformation  $\eta \rightarrow -\eta$  because of the cubic term. This is referred to as spontaneous symmetry breaking. The word "spontaneous" is used simply because the symmetry is not broken by any "external influence", but simply because the ground states of the field do not obey the same symmetry as the Lagrangian.

## Complex scalar field

Another slightly more relevant example of spontaneous symmetry breaking can be given by considering a complex scalar field

$$\phi = \frac{1}{\sqrt{2}}(\phi_1 + i\phi_2),$$

with the corresponding Lagrangian

$$\mathcal{L} = (\partial_\mu\phi^*)(\partial^\mu\phi) - \mu^2(\phi^*\phi) + \lambda(\phi^*\phi)^2, \quad (1.34)$$

---

<sup>4</sup>Notice that the mass term of a scalar field is accompanied by a factor  $\frac{1}{2}$  in the Lagrangian, which is not the case for fermions. If such a factor is not explicitly written in the Lagrangian it must be included when writing down the mass of the scalar field.

<sup>5</sup>The ground state is chosen to be *one* of the two possible definitions of  $\eta$ .

still with  $\lambda > 0$ . This Lagrangian is symmetric under global  $U(1)$  transformations, but the ground state again depends on whether  $\mu^2$  is larger or smaller than zero. If  $\mu^2 < 0$  the potential has an infinite set of minima given by

$$\phi_1^2 + \phi_2^2 = -\frac{\mu^2}{\lambda^2} = v^2,$$

i.e. a circle in the  $\phi_1, \phi_2$ -plane. This potential is often referred to as the "Mexican hat" potential, as illustrated in Figure 1.5. The corresponding ground state breaks the global  $U(1)$  symmetry.

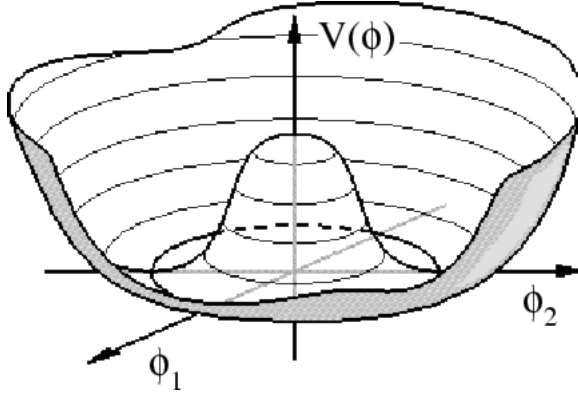


Figure 1.5: The scalar ("Mexican hat") potential as function of  $\phi_1$  and  $\phi_2$ , taken from ref. [14].

A convenient choice of ground state is  $\phi_1 = v$  and  $\phi_2 = 0$ . Then we can define two new fields,  $\eta$  and  $\xi$ , with vacuum expectation values corresponding to the ground state, so  $\phi_1(x) = \eta(x) + v$  and  $\phi_2(x) = \xi(x)$ , hence

$$\phi = \frac{1}{\sqrt{2}}(\eta + v + i\xi). \quad (1.35)$$

Finally this leads to a Lagrangian of the form

$$\mathcal{L} = \frac{1}{2}(\partial_\mu \eta)(\partial^\mu \eta) + \frac{1}{2}(\partial_\mu \xi)(\partial^\mu \xi) - \lambda v^2 \eta^2 + V_{int}(\eta, \xi), \quad (1.36)$$

where  $V_{int}(\eta, \xi)$  represents the interaction terms for the two fields. We have now ended up with a massive  $\eta$  field ( $m_\eta = \sqrt{2\lambda}v$ ) and a massless  $\xi$  field. The *Goldstone theorem* [15] states that a massless field will appear whenever a continuous symmetry is spontaneously broken, and such a field is referred to as a *Goldstone boson*.

#### 1.4.4 Brout-Englert-Higgs mechanism

We have now considered spontaneous breaking of a discrete symmetry for the real scalar field and a global (and continuous) symmetry for the complex scalar field. The next step is to include spontaneous symmetry breaking in the *local* electroweak

gauge theory we have been studying, which will eventually lead to a theory with massive gauge bosons. For instructive reasons we first consider spontaneous breaking of local  $U(1)$  symmetry, and then move on to the full  $SU(2)_L \times U(1)_Y$  gauge group.

### Local $U(1)$ symmetry breaking

Once again we start with a complex scalar field,  $\phi$ , with potential

$$V(\phi) = \mu^2\phi^2 + \lambda\phi^4,$$

and require the Lagrangian to be invariant under a local  $U(1)$  transformation,

$$\phi \rightarrow e^{ig\chi(x)}\phi, \quad (1.37)$$

which means that we must replace the derivative with a covariant derivative,

$$D_\mu = \partial_\mu + igB_\mu,$$

leading to the Lagrangian

$$\mathcal{L} = (D_\mu\phi)^*(D^\mu\phi) - \mu^2\phi^2 - \lambda\phi^4 - \frac{1}{4}F^{\mu\nu}F_{\mu\nu}, \quad (1.38)$$

with  $F_{\mu\nu} = \partial_\mu B_\nu - \partial_\nu B_\mu$ . This is essentially QED for a scalar field, except from the  $\phi$  self-coupling term. Now we proceed in a very similar way as previously. We realize that by choosing  $\mu^2 < 0$  the  $U(1)$  symmetry will be spontaneously broken by the vacuum state. By choosing the vacuum state to be  $\phi_1 = v$  and  $\phi_2 = 0$ , the field can be written as

$$\phi = \frac{1}{\sqrt{2}}(v + \eta + i\xi),$$

which leads to the Lagrangian

$$\begin{aligned} \mathcal{L} = & \frac{1}{2}(\partial_\mu\eta)(\partial^\mu\eta) + \frac{1}{2}(\partial_\mu\xi)(\partial^\mu\xi) - \lambda v^2\eta^2 + \frac{1}{2}g^2v^2B_\mu B^\mu - \frac{1}{4}F^{\mu\nu}F_{\mu\nu} \\ & + V_{int}(\eta, \xi, B) + gvB_\mu(\partial^\mu\xi), \end{aligned} \quad (1.39)$$

where  $V_{int}(\eta, \xi, B)$  represents the interaction terms of  $\eta$ ,  $\xi$  and  $B$ . Again we are left with a massive  $\eta$  field and a massless Goldstone boson ( $\xi$ ), but we have also produced a mass term for the gauge field.

However, we are not quite finished yet, because there are some problems with Equation 1.39. First, we seem to have gotten an additional degree of freedom since the gauge field has acquired a mass, and second, the last term of Equation 1.39 suggests that the spin-1 gauge boson can transform directly into the scalar  $\xi$ . These problems can actually be solved by choosing the gauge as  $\chi(x) = -\frac{\xi(x)}{gv}$ , which is called the *unitary* gauge. By approximating  $\phi$  as

$$\phi \approx \frac{1}{\sqrt{2}}(v + \eta)e^{i\xi/v}$$

we get that  $\phi$  now transforms under  $U(1)$  as

$$\phi \rightarrow \frac{1}{\sqrt{2}}(v + \eta) \equiv \frac{1}{\sqrt{2}}(v + h).$$

By also making a gauge transformation

$$B_\mu \rightarrow B_\mu + \frac{1}{gv} \partial_\mu \xi,$$

we end up with the Lagrangian

$$\mathcal{L} = \frac{1}{2}(\partial_\mu h)(\partial^\mu h) - \lambda v^2 h^2 + \frac{1}{2}g^2 v^2 B_\mu B^\mu - \frac{1}{4}F^{\mu\nu}F_{\mu\nu} + V_{int}(h, B), \quad (1.40)$$

which contains a massive scalar field,  $h$ , and a massive gauge field,  $B$ .  $V_{int}$  contains interactions between  $h$  and  $B$ , as well as  $h$  self-interactions. The Goldstone boson no longer appears in the Lagrangian, and we say that it has been "eaten" by the gauge boson.

### Local $SU(2)_L \times U(1)_Y$ symmetry breaking

In order to implement the BEH mechanism for the full gauge group of GWS theory we must introduce two complex scalar fields in a weak isospin doublet,

$$\phi = \begin{pmatrix} \phi^+ \\ \phi^0 \end{pmatrix} = \frac{1}{\sqrt{2}} \begin{pmatrix} \phi_1 + i\phi_2 \\ \phi_3 + i\phi_4 \end{pmatrix} \quad (1.41)$$

where the upper and lower component differs by one unit in charge. The Lagrangian is now written as

$$\mathcal{L} = (D_\mu \phi)^\dagger (D^\mu \phi) - \mu^2 \phi^\dagger \phi - \lambda (\phi^\dagger \phi)^2, \quad (1.42)$$

and the potential is referred to as the Higgs potential. Once again we realize that the ground state breaks the symmetry for  $\mu^2 < 0$ , and by following the same procedure as above we realize that  $\phi$  can be written in unitary gauge as

$$\phi = \frac{1}{\sqrt{2}} \begin{pmatrix} 0 \\ v + h \end{pmatrix}, \quad (1.43)$$

where  $v^2 = -\mu^2/\lambda$ . The derivative in the Lagrangian is then replaced by the covariant derivative of GWS theory given in Equation 1.24, which leads to three massive gauge fields ( $W_\mu^\pm, Z_\mu$ ), one massless gauge field ( $A_\mu$ ) and a massive scalar field ( $h$ ). The masses of the gauge bosons are given by

$$m_W = \frac{1}{2}gv \quad \text{and} \quad m_Z = \frac{1}{2}v\sqrt{g^2 + g'^2} \quad (1.44)$$

and the mass of the Higgs boson is given by

$$m_H = \sqrt{2\lambda}v. \quad (1.45)$$

In addition to the couplings pictured in Figure 1.4 the GWS theory now also contains the couplings given in Figure 1.6, namely couplings between the Higgs boson and the massive gauge bosons as well as the Higgs self-interactions. The couplings between the Higgs boson and the gauge bosons are proportional to the squared mass of the gauge bosons.

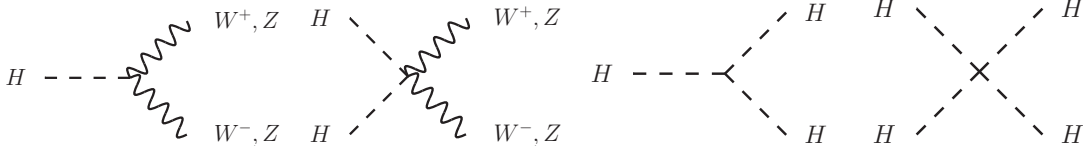


Figure 1.6: Couplings between the Higgs boson and the massive gauge bosons, as well as the Higgs self-couplings.

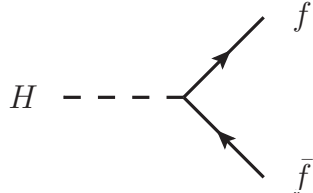


Figure 1.7: The Yukawa coupling between fermions and the Higgs boson.

### Fermion masses

Now only a small (but important) part is missing, namely the fermion masses. It turns out that the BEH mechanism with spontaneous breaking of the  $SU(2)_L \times U(1)_Y$  symmetry can be used also to generate fermion masses. The Lagrangian for down-type fermions (i.e. lower element in the isospin doublet) becomes

$$\mathcal{L} = -\frac{g_f v}{\sqrt{2}}(\bar{\psi}_L \psi_R + \bar{\psi}_R \psi_L) - \frac{g_f h}{\sqrt{2}}(\bar{\psi}_L \psi_R + \bar{\psi}_R \psi_L), \quad (1.46)$$

which describes fermions with mass

$$m_f = \frac{g_f v}{\sqrt{2}},$$

and the coupling between fermions and the Higgs field, which is pictured in Figure 1.7. The constant  $g_f$  is referred to as the Yukawa coupling constant. Interesting to notice is that both the Yukawa couplings and the Higgs couplings to the heavy gauge bosons involves the mass of the particles, which ultimately means that the Higgs boson favours couplings to heavy particles.

In order to generate mass for the up-type fermions one needs to replace the scalar doublet in Equation 1.43 by  $\phi_c = -i\sigma_2\phi^*$ , which transforms in the same way as  $\phi$ .

### 1.4.5 The full GWS Lagrangian

Just to put all the pieces of GWS theory together the full Lagrangian is presented in Equation 1.47. Here  $\psi_L$  is a left-handed isospin doublet and  $\psi_R$  is a right-handed isospin singlet. The first line contains the couplings between fermions and the gauge fields and kinetic terms for the fermion fields. The second line contains the kinetic terms for the gauge fields and the BEH field, the couplings between the gauge field and the BEH field, and the couplings between the gauge fields. The third line

contains the scalar potential, the Yukawa coupling terms and the fermion mass terms.

$$\begin{aligned} \mathcal{L}_{GWS} = & \bar{\psi}_L \gamma^\mu \left[ i\partial_\mu - \frac{g}{2} \boldsymbol{\sigma} \mathbf{W}_\mu - \frac{g'Y}{2} B_\mu \right] \psi_L + \bar{\psi}_R \gamma^\mu \left[ i\partial_\mu - \frac{g'Y}{2} B_\mu \right] \psi_R \\ & - \frac{1}{4} B^{\mu\nu} B_{\mu\nu} - \frac{1}{4} \mathbf{W}^{\mu\nu} \mathbf{W}_{\mu\nu} + \left| \left( i\partial_\mu - \frac{g}{2} \boldsymbol{\sigma} \mathbf{W}_\mu - \frac{g'Y}{2} B_\mu \right) \phi \right|^2 \\ & - V(\phi) - (g_f \bar{\psi}_L \phi \psi_R + G'_f \bar{\psi}_L \phi_c \psi_R + h.c.) \end{aligned} \quad (1.47)$$

## 1.5 Limitations of the Standard Model

The full SM is the combination between GWS theory and QCD, and the SM gauge group is written as  $SU(3)_C \times SU(2)_L \times U(1)_Y$ . This is undoubtedly an incredibly successful theory, which has so far never failed to explain the outcome of a particle physics experiment. Amongst its greatest successes is the discovery of the  $W$ - and  $Z$ -bosons by the UA1 and UA2 experiments [17, 18, 19], and the discovery of the Higgs boson by the ATLAS [20] and CMS [21] experiments. It also worth mentioning that QCD is able to explain data (e.g. from the LHC) at TeV scale. The fact that the SM has shown to be such a successful theory is actually a bit surprising, given that there are a lot of problems and open questions related to it. Some of these problems are related to observations on astronomical scales that the SM is unable to account for, while some problems are of a more theoretical nature.

One of the most obvious problems was mentioned in the introduction, namely that the SM only accounts for  $\sim 5\%$  of the universe, and the rest is believed to be dark matter and dark energy. Dark energy is introduced to explain the accelerating expansion of the universe, and is often assumed to be associated with the vacuum expectation value of some quantum field, but the nature of this field is a mystery. Dark matter, on the other hand, is a little more "concrete", in the sense that it is usually assumed to consist of weakly interacting massive particles (WIMPs), which are particles that only couple weakly (or not at all) to the SM particles. The existence of dark matter is inferred from observations of the motion of stars and galaxies, which cannot be explained by gravitational interactions with only ordinary matter. Many physicists are kept busy trying to figure out what dark matter is, and several experiments are done (or planned) to produce and/or detect dark matter particles. So far without any luck.

Another observational fact is that the universe has an excess of matter over antimatter, meaning that the  $CP$  symmetry must be violated. Of the SM interactions it is only the weak interaction that is capable of violating this symmetry, but it is actually not clear whether or not  $CP$  symmetry is sufficiently violated in the SM to explain the matter-antimatter asymmetry of the universe. Several experiments are doing precision measurements related to this, but if it turns out that  $CP$  violation is too small in the SM there is an obvious need for new physics to explain this.

Another problem with the SM is that it contains 25 free parameters, i.e. parameters that can only be determined by experimental measurements. These parameters include the fermion masses, the coupling constants, the vacuum expectation value of the BEH field ( $v$ ) and the Higgs mass, and the parameters describing the mixing between mass eigenstates and weak eigenstates of neutrinos and quarks respectively. In a more complete theory the values of these parameters would be predicted by the theory itself.

The three coupling constants of the SM are so-called *running couplings*, meaning that they depend on the energy scale at which the interaction takes place. This is shown in Figure 1.8, where  $\alpha_1$ ,  $\alpha_2$  and  $\alpha_3$  are related to  $SU(3)_C$ ,  $SU(2)_L$  and  $U(1)_Y$  respectively. Some theories called Grand Unified Theories (GUTs) predict that all three forces should be unified at high energies, meaning that all three coupling constants should meet in one single point. From Figure 1.8 we see that this is obviously not the case in the SM.

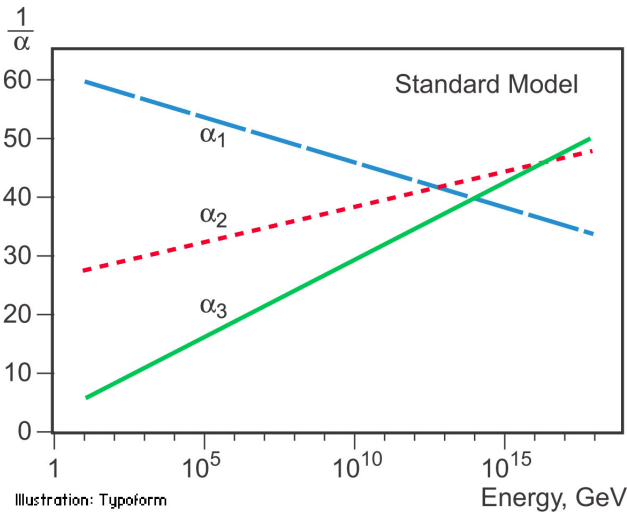


Figure 1.8: The running coupling constants of the Standard Model, from ref. [22].

The last problem with the SM that will be discussed is related to the mass of the Higgs boson. When discussing different QFTs we have actually only considered contributions at leading order in perturbation theory. If we include higher-order terms, so-called *loop corrections*, we will for instance get corrections in the expression for the  $W$ -mass (Eq. 1.44) and the Higgs mass (Eq. 1.45). Examples of such loops for the Higgs boson are shown in Figure 1.9. For the Higgs mass these corrections are divergent, i.e. at high energies they get very large, and it seems impossible to keep the Higgs mass at the electroweak scale. This is known as the *hierarchy problem*, and is one of the main motivations for Supersymmetry, which will be discussed in the next chapter.

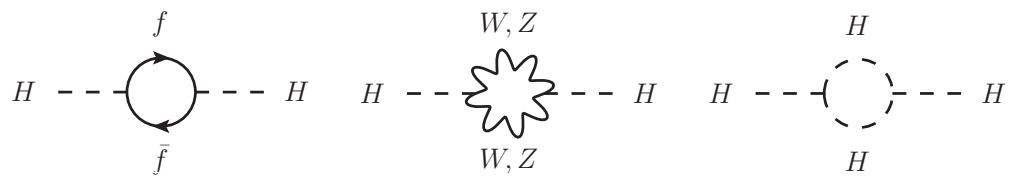


Figure 1.9: Examples of loop corrections to the Higgs mass.

# Chapter 2

## Supersymmetry

This chapter gives a brief overview of the most relevant and necessary features of Supersymmetry (SUSY). We start off by short a introduction explaining what SUSY is, and then we move on to describing a supersymmetric model called the Minimal Supersymmetric Standard Model, with most emphasis on its particle content and how it solves some of the problems with the SM. Towards the end of the chapter we discuss the particular process that is subject of the analysis in this thesis, namely direct production of sleptons.

More complete introductions to SUSY can be found for instance in refs. [23, 24], while the review given in this chapter is mostly based on refs. [25, 26].

### 2.1 Introduction to Supersymmetry

SUSY is a symmetry relating fermions and bosons. It states that every SM particle has a so-called *superpartner* (or SUSY partner), whose spin differ by  $\frac{1}{2}$ . The fermions have spin-0 (scalar) superpartners, while the bosons have spin- $\frac{1}{2}$  (fermionic) superpartners. If SUSY were an exact symmetry its particles (often referred to as *sparticles*) would have exactly the same mass and other properties as their SM partners, except from the difference in spin. If that was the case SUSY would have been discovered a long time ago. This means that if SUSY exists it must be a broken symmetry, in the sense that the sparticles must be much heavier than their SM partners, hence out of reach for experiments so far.

An attractive property of SUSY is that we don't need to introduce any new gauge groups, hence no new fundamental forces. Instead we introduce a SUSY operator,  $\hat{Q}$ , that commutes with the gauge transformations of the SM, and relates fermions and bosons by

$$\hat{Q} | \text{fermion} \rangle = | \text{boson} \rangle \quad \text{and} \quad \hat{Q} | \text{boson} \rangle = | \text{fermion} \rangle .$$

The fundamental representations of the SM gauge groups (i.e. colour triplets or weak isospin doublets) together with their superpartners form *supermultiplets*. Left-handed and right-handed fermions belong to different supermultiplets since they are organised in isospin doublets and singlets respectively. This means that left- and right-handed fermions have distinct superpartners, even though their scalar superpartners don't have handedness.

The superpartners of fermions are called *sfermions*, and the names of the individual sfermions follow the same name prescription, so the superpartner of the leptons are called *sleptons* and the superpartners of the quarks are called *squarks*. Further the superpartner of an electron is called a *selectron*, the superpartner of a top quark is called *stop*, and so on. They are denoted with a tilde above their names, so  $\tilde{e}$  is a selectron and  $\tilde{t}$  is a stop.

The superpartners of gauge bosons are called *gauginos*, and are also denoted with a tilde. The *winos* ( $\tilde{W}$ ) and the *binos* ( $\tilde{B}$ ) are superpartners of the  $W$ -bosons and the  $B$ -boson (see for instance Eq. 1.29), while the superpartners of the gluons are called *gluinos* ( $\tilde{g}$ ). The Higgs boson is also accompanied by superpartners called *higgsinos*.

## 2.2 The Minimal Supersymmetric Standard Model

In the Minimal Supersymmetric Standard Model (MSSM) a minimal number of sparticles are introduced, so we basically just introduce one superpartner for each SM particle, following the naming scheme presented in the previous section. This might seem very straight forward, but there is a complication to this approach, namely the Higgs sector. In GWS theory we introduced one scalar doublet with four degrees of freedom, where three of these gave mass to  $W^\pm$  and  $Z$ , while the last degree of freedom materialized as the massive Higgs boson, and we used the charge conjugate ( $\phi_c$ ) of the scalar doublet to give mass to the up-type fermions. However, charge conjugate fields are not allowed in SUSY since they would ruin the invariance under gauge and SUSY transformations. For this reason we need to introduce two scalar doublets, which means that we have eight degrees of freedom, leading to five different Higgs bosons instead of one. These are two charged ( $H^\pm$ ), one heavy CP-even ( $H^0$ ), one heavy CP-odd ( $A^0$ ) and one light Higgs boson ( $h^0$ ).

The particle content of the MSSM is given in Figure 2.1, where spontaneous electroweak symmetry breaking is assumed, such that it is the mass eigenstates that are given in the figure. The neutral gauge bosons (bino and neutral wino) and the neutral higgsinos ( $\tilde{H}^0$  and  $\tilde{h}^0$ ) mix to form four *neutralinos* ( $\tilde{\chi}_1^0$ ,  $\tilde{\chi}_2^0$ ,  $\tilde{\chi}_3^0$  and  $\tilde{\chi}_4^0$ ), while the charged winos and the charged higgsinos mix to form four *charginos* ( $\tilde{\chi}_1^\pm$  and  $\tilde{\chi}_2^\pm$ ). Also the right-handed and left-handed sleptons and squarks mix to form mass states that are different from the weak eigenstates. In Figure 2.1 this is indicated with subscript 1, 2 only for the third generation, because the mixing is negligible for the first two generations.

The potential that describes the dynamics of a SUSY model is referred to as the *superpotential*. Details about this will not be given here, but it is worth mentioning that in the MSSM the superpotential involves terms that seemingly violate conservation of baryon and lepton number. This is a big problem because it for instance allows the proton to decay at an unusual rate ruled out by experiments. To fix this one introduces a new multiplicative quantum number called *R-parity*, given by

$$P_R = (-1)^{3(B-L)+2s}, \quad (2.1)$$

where  $B$  and  $L$  are the baryon and lepton number respectively, and  $s$  is spin. It follows that all particles have  $P_R = +1$ , while sparticles have  $P_R = -1$ . We then

	Particles			Spin	Sparticles			
quarks	$u_{L,R}$	$c_{L,R}$	$t_{L,R}$	1/2	0	$\tilde{t}_{1,2}$	$\tilde{c}_{L,R}$	$\tilde{u}_{L,R}$
	$d_{L,R}$	$s_{L,R}$	$b_{L,R}$	1/2	0	$\tilde{b}_{1,2}$	$\tilde{s}_{L,R}$	$\tilde{d}_{L,R}$
leptons	$\nu_e$	$\nu_\mu$	$\nu_\tau$	1/2	0	$\tilde{\nu}_\tau$	$\tilde{\nu}_\mu$	$\tilde{\nu}_e$
	$e_{L,R}$	$\mu_{L,R}$	$\tau_{L,R}$	1/2	0	$\tilde{\tau}_{1,2}$	$\tilde{\mu}_{L,R}$	$\tilde{e}_{L,R}$
gauge bosons	$g$			1	1/2	$\tilde{g}$		
	$W^\pm, Z^0$			1	1/2	Neutralinos $\tilde{\chi}^{0,1-4}$		
	$\gamma$			1	1/2	Charginos $\tilde{\chi}^{\pm,1-2}$		
	$H^\pm, H^0, A^0, h^0$			0				

Figure 2.1: Particle content of the MSSM, taken from ref. [26].

require R-parity to be conserved, which has some interesting consequences. First of all SUSY particles will *always* be produced in pairs in particle colliders, i.e. a sparticle and an anti-sparticle. Second (and maybe most exciting) the lightest supersymmetric particle (LSP) must be stable. If the LSP is massive and only weakly interacting (i.e. a WIMP) it is a good dark matter candidate particle, meaning that the MSSM could provide a solution to the dark matter problem.

Another very attractive feature of the MSSM is the evolution of the running coupling constants. In Section 1.5, we discussed that GUTs predicts unification of the forces at high energies, but we saw in Figure 1.8 that this does not happen in the SM. In Figure 2.2 we can see that in the MSSM the coupling constants do meet in one single point. This is due to the various SUSY particles showing up in the loop corrections and altering the relative evolutions of the three fundamental coupling constants.

Dark matter candidate particles and unification of coupling constants are indeed nice properties and motivations for SUSY (and the MSSM in particular). However, there is an even greater motivation for the MSSM, which is that it solves the hierarchy problem in a perfectly natural way. At the end of Section 1.5 we said that the hierarchy problem is caused by the diverging loop corrections to, for example, the Higgs mass. In the MSSM we also get loops (like in Figure 1.9) involving sparticles, and it actually turns out that the particle loop corrections and the sparticle loop corrections (mathematically) nearly cancel each other out, meaning that we do not get the divergent corrections to the Higgs mass.

Although SUSY provides solutions to several of the SM problems it is most

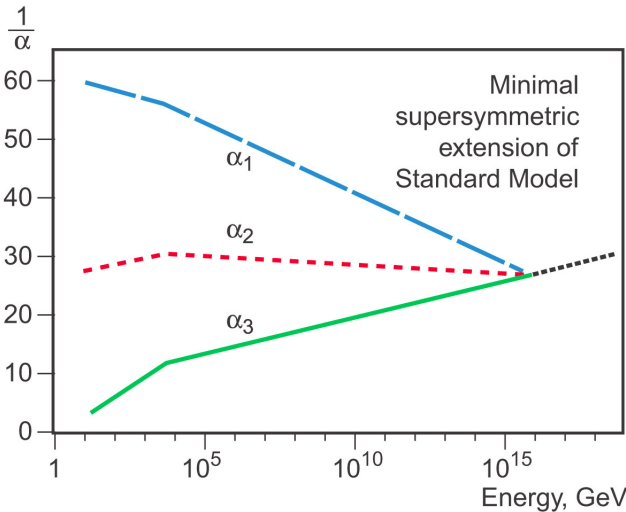


Figure 2.2: Running coupling constants of the MSSM, taken from ref. [22]

certainly not the "ultimate" theory of nature. For instance the MSSM has a spectacular number of free parameters (124 in total), and like the SM it does not include gravity. It should be mentioned that proposed quantum theories of gravity (such as string theory) requires SUSY, and SUSY might therefore be a necessary ingredient towards a complete theory of nature.

### 2.2.1 Soft SUSY breaking

Probably the most striking problem with SUSY is however that no experiment has so far seen any sign of it, which means that it must be a broken symmetry, in the sense that sparticles are heavier than their SM partners. But to still be able to solve the hierarchy problem the sparticle masses should not be much larger than 1 TeV, which is referred to as *soft* SUSY breaking. It is assumed that the symmetry breaking is spontaneous, but it is not clear what the mechanism behind the symmetry breaking is. It is expected that once the mechanism is known it is possible to reduce the number of free parameters from 124 to only a few at some higher energy scale (i.e. GUT scale).

One of the possible models explaining SUSY breaking is supergravity (SUGRA), which introduces gravitational interactions between the MSSM fields and fields in a hidden sector. The simplest of such models is called minimal supergravity (mSUGRA), which at GUT scale only depends on five parameters. These are

$$m_0, m_{\frac{1}{2}}, A_0, \tan \beta \text{ and } \text{sgn}(\mu),$$

where  $m_0$  is a common mass of scalar particles,  $m_{\frac{1}{2}}$  is a common mass of gauginos,  $A_0$  is the tri-linear (Yukawa) coupling between the Higgs boson and fermions,  $\tan \beta$  is the ratio between vacuum expectation values of the up and down Higgs doublets and  $\text{sgn}(\mu)$  is the sign of the Higgs/Higgsino mass term. The sparticle masses at the electroweak scale are then obtained by using so-called Renormalization Group

Equations (RGEs). The evolution of the mSUGRA parameters are shown in Figure 2.3.

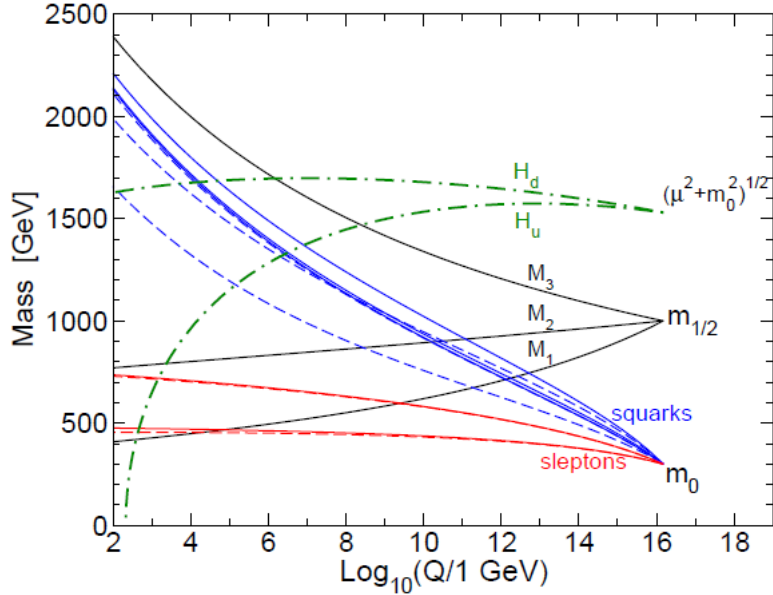


Figure 2.3: Evolution of the mass parameters of the MSSM in mSUGRA, taken from ref. [24].

Another model for SUSY breaking is Gauge-Mediated SUSY Breaking (GMSB), where symmetry is broken by the usual gauge interactions. In this model a new set of supermultiplets called "messenger fields" is introduced, which couple both to the source of SUSY breaking in a hidden sector and to sparticles. A minimal GMSB is also described by five parameters at GUT scale, namely

$$F_m, M_m, N, \tan \beta \text{ and } \text{sgn}(\mu),$$

where  $F_m$  is the energy scale where SUSY is broken,  $M_m$  is the mass scale of the messenger fields,  $N$  is the number of messenger fields (or messenger supermultiplets), and  $\tan \beta$  and  $\text{sgn}(\mu)$  are the same as in mSUGRA above.

## 2.3 Direct slepton production

Now that we have introduced the necessary theory the upcoming chapters will focus more on the experimental aspects, but before we move on we should have a look at the specific processes targeted by the analysis carried out in this thesis. The processes to be considered are referred to as *direct slepton production*, and is pictured in Figure 2.4, where sparticles are drawn in red colour. Figure 2.4a shows how a pair of sleptons can be produced through quark-antiquark annihilation, while Figure 2.4b shows how the sleptons are assumed to decay.

Because of charge conservation and lepton number conservation the two sleptons must have opposite signed charge and same lepton flavour, so either  $\tilde{e}^+ \tilde{e}^-$ ,  $\tilde{\mu}^+ \tilde{\mu}^-$  or

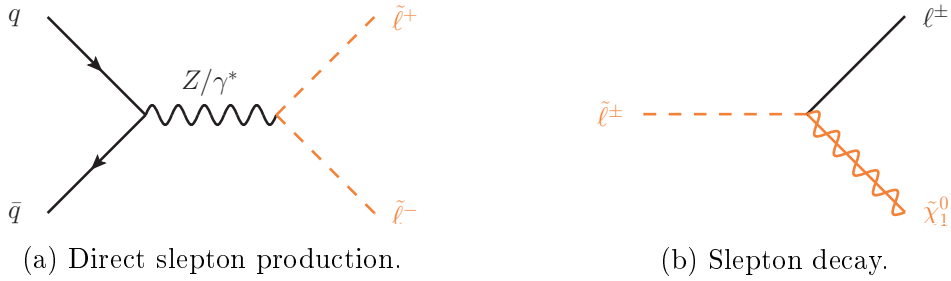


Figure 2.4: Feynman diagrams for production and decay of sleptons.

$\tilde{\tau}^+ \tilde{\tau}^-$ . By considering the mentioned conservation laws again we realize that each slepton must decay to their corresponding SM partner accompanied by another (neutral) fermion. In the model we consider we assume this fermion to be the lightest neutralino,  $\tilde{\chi}_1^0$ , and we also assume that this is the LSP, and hence stable because of R-parity conservation. In SUSY searches one typically makes use of *simplified* models [27] where the masses and the coupling constants of the sparticles targeted by the search are the only free parameters. In the model we consider the slepton mass,  $m_{\tilde{\ell}}$ , and the neutralino mass,  $m_{\tilde{\chi}_1^0}$ , are the only free parameters, and the sleptons are assumed to decay to  $\ell \tilde{\chi}_1^0$  with 100% branching ratio.

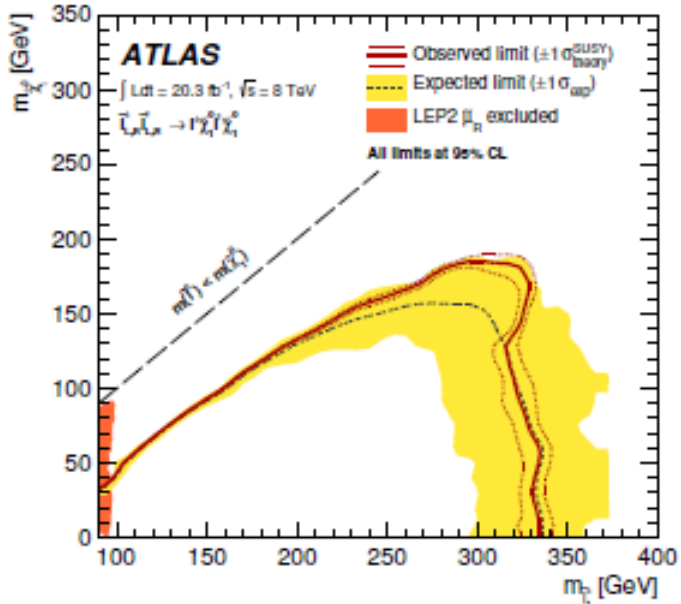


Figure 2.5: Exclusion limits on sleptons and neutralinos set by ATLAS in Run 1 of the LHC. [30]

The neutralinos will not leave any traces in a particle detector, which means that the events we study in the analysis should contain only two leptons with same flavour and opposite signed charge, i.e. a pair of electrons,  $e^+ e^-$ , or a pair of muons,  $\mu^+ \mu^-$ . Tau leptons are not explicitly considered in the analysis because they have a very short lifetime ( $\sim 3 \cdot 10^{-13}$  s [29]), and will therefore decay very close to the

interaction point in the experiment, unlike muons which can travel a considerable distance before decaying. With the ATLAS detector it is to some extent possible to reconstruct  $\tau$ 's [28], but this requires hadronic  $\tau$  decays, hence not giving two lepton final states. However, if both  $\tau$ 's decay leptonically they could be included in the analysis if the resulting leptons fulfil the requirements given in Sections 5.2 and 5.3.

Searches for direct slepton production was also performed using Run 1 LHC data at 8 TeV centre of mass energy, and the exclusion limits on the slepton mass and the neutralino mass set by the ATLAS experiment are shown in Figure 2.5. Slepton masses up to about 350 GeV were excluded for a light  $\tilde{\chi}_1^0$ .

# Chapter 3

## Proton-Proton Collisions

The data set used for this thesis is produced by colliding protons with each other in the ATLAS detector at the Large Hadron Collider. (See Chapter 4 for an introduction to ATLAS and the LHC.) Since the proton is *not* an elementary particle a proton-proton ( $pp$ ) collision is a somewhat complex business. This chapter is devoted to a description of the most important aspects and features of such collisions.

### 3.1 Kinematics

The kinematics of a particle is described by the particles momentum,  $\mathbf{p} = (p_x, p_y, p_z)$ , energy,  $E$ , and rest mass,  $m$ . From special relativity momentum and energy are given as

$$\mathbf{p} = \beta \gamma m \quad \text{and} \quad E = \gamma m \tag{3.1}$$

respectively, where

$$\gamma = \frac{1}{\sqrt{1 - \beta^2}} \quad \text{and} \quad \beta = \frac{v}{c}.$$

The four-momentum is defined as  $P^\mu = (E, \mathbf{p})$ , from which we can construct the Lorentz invariant  $P^2 = P^\mu P_\mu$ , and by also making use of Equation 3.1 we get

$$\begin{aligned} P^2 &= E^2 - \mathbf{p}^2 \\ &= \gamma^2 m^2 - \beta^2 \gamma^2 m^2 \\ &= m^2 \gamma^2 (1 - \beta^2) \\ &= m^2, \end{aligned}$$

hence we have arrived to the famous Einstein energy-momentum formula,

$$E^2 = m^2 + \mathbf{p}^2, \tag{3.2}$$

which turns out to be a very useful result when studying particle collisions.

### 3.1.1 The two particle collision

In particle collider experiments the reference frame of the laboratory often corresponds to the Centre-of-Mass (CM) frame of the two colliding particles (i.e. two protons in the LHC). The CM frame is defined as the reference frame where sum of three-momenta is zero, so for two particles, 1 and 2, this means that  $\mathbf{p}_1 = -\mathbf{p}_2 \equiv \mathbf{p}$ . If the rest masses of the two particles also are equal we get (from Equation 3.2)  $E_1 = E_2 \equiv E$ . The sum of four-momenta is then given as

$$(P_1 + P_2)^\mu = (2E, \mathbf{0}). \quad (3.3)$$

The Mandelstam variable  $s$  is defined as the squared sum of four-momenta, so in this case

$$s = (P_1 + P_2)^2 = 4E^2,$$

which means that  $\sqrt{s} = 2E$  is the total energy in the CM system. This is a key figure when describing the performance of a particle collider.

In the derivation of Equation 3.2 we saw that  $P^2 = m^2$ . Now, assume for a moment that the particles we collide are elementary. Since  $s$  is the squared four-momentum of the two colliding particles,  $\sqrt{s}$  can be interpreted as the energy available for production of heavier particles, i.e. for a particle with mass  $M$  produced in the collision we must have  $M \leq \sqrt{s}$ .

However, the proton is *not* elementary, but made up of quarks and gluons, commonly referred to as *partons*. This means that in a  $pp$  collision it is actually two partons that collide, and each parton carries only a certain fraction of the total momentum of the proton.

The direction of the proton beams is usually defined to be the  $z$ -direction, such that  $\mathbf{p} = (0, 0, p)$ . Assuming that  $p \gg m_p$ , where  $m_p$  is the mass of the proton, we get from Equation 3.2 that  $E \approx p$ , which means that the proton four-momenta can be written as  $P_1^\mu = (E, 0, 0, E)$  and  $P_2^\mu = (E, 0, 0, -E)$ .

The momenta carried by the two colliding partons are denoted  $\mathbf{q}_1$  and  $\mathbf{q}_2$ . In principle the partons can carry momenta also in the  $x$ - and  $y$ -directions, but we assume that these components are small enough to be neglected, such that  $\mathbf{q}_1 = (0, 0, q_1)$  and  $\mathbf{q}_2 = (0, 0, q_2)$ <sup>1</sup>. By also neglecting the parton masses the four-momenta of the partons are  $Q_1^\mu = (q_1, 0, 0, q_1)$  and  $Q_2^\mu = (q_2, 0, 0, q_2)$ . Further we define  $x_1$  and  $x_2$  as the fractions of momentum carried by the partons, so

$$x_1 = \frac{q_1}{E} \quad \text{and} \quad x_2 = \frac{q_2}{E}, \quad (3.4)$$

which means that the parton four-momenta can be written as

$$Q_1^\mu = x_1(E, 0, 0, E) \quad \text{and} \quad Q_2^\mu = x_2(E, 0, 0, -E). \quad (3.5)$$

---

<sup>1</sup>Note that when we move to the parton reference frame the lab-frame does in general **not** correspond to the CM frame of the two partons, so we can **not** say that  $q_1 = -q_2$

The maximal rest mass of a particle we can produce in the collision is now given by

$$\begin{aligned} M^2 &\leq (Q_1 + Q_2)^2 \\ &= [(x_1 + x_2)^2 - (x_1 - x_2)^2]E^2 \\ &= 4x_1 x_2 E^2 \\ &= x_1 x_2 s. \end{aligned}$$

How the momentum in the proton is distributed between the partons (i.e. the values of  $x_1$  and  $x_2$ ) is described by so-called *parton distribution functions*, which are discussed in Section 3.2.1.

### 3.1.2 The products of the collision

From describing the collision itself we now move on to describing the kinematics of the particles that are produced in the collision. As previously we take the  $z$ -direction to be the direction of the beam, while the positive  $y$ -direction is upwards and the positive  $x$ -direction points towards the centre of the accelerator ring. The  $xy$ -plane is usually referred to as the *transverse* plane, and the plane going through the  $z$ -axis as the *longitudinal* plane.

The kinematic variables we consider are usually defined in spherical coordinates, with  $\phi$  as the azimuthal angle and  $\theta$  as the polar angle, which is illustrated in Figure 3.1. Since the collision takes place in the  $z$ -direction it is often quite handy to work with kinematics only in the transverse plane. The magnitude of the transverse momentum vector,  $\mathbf{p}_T$ , is given as

$$p_T = \sqrt{p_x^2 + p_y^2} = p \sin \theta, \quad (3.6)$$

while the transverse energy is given as

$$E_T = \sqrt{m^2 + p_T^2}, \quad (3.7)$$

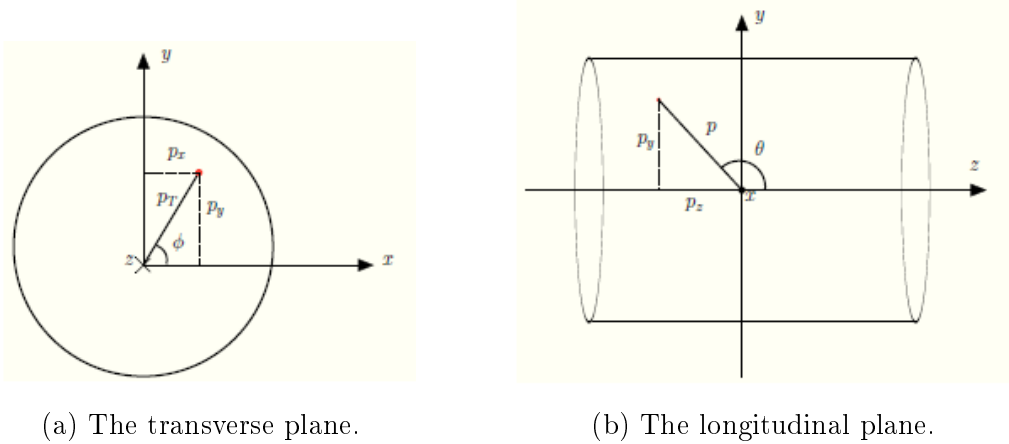
which is found by restricting 3.2 to the transverse plane.

The particles that are produced in the collision are often boosted in the  $z$ -direction because of the difference in the momenta of the colliding partons. For this reason we like to make use of a variable called *rapidity*,  $y$ , defined as

$$y = \frac{1}{2} \ln \left( \frac{E + p_z}{E - p_z} \right). \quad (3.8)$$

The benefit of this variable is that differences in  $y$  are invariant under Lorentz boosts in the  $z$ -direction, which is not the case for  $\theta$ . If the mass of the particle is small compared to  $p_z$  (which is usually a good approximation) we have  $p_z \sim E \cos \theta$ , which leads to

$$\begin{aligned} y &\approx \frac{1}{2} \ln \left( \frac{1 + \cos \theta}{1 - \cos \theta} \right) \\ &= \frac{1}{2} \ln(\cot^2 \frac{\theta}{2}) \\ &= -\ln(\tan \frac{\theta}{2}) \equiv \eta, \end{aligned} \quad (3.9)$$



(a) The transverse plane.

(b) The longitudinal plane.

Figure 3.1: Illustration of *a*) the transverse plane and *b*) the longitudinal plane. The origin is the collision point, and the cylinder illustrates how a detector typically is placed around the collision point. Both figures are taken from ref. [25].

where  $\eta$  is called the *pseudo-rapidity*. Values of  $\eta$  for a few different  $\theta$ -values is shown in Figure 3.2. Together  $p_T$ ,  $\phi$  and  $\eta$  make up the set of variables that are most commonly used when describing the kinematics of a particle in a detector.

The distance,  $\Delta R$ , between two particles is often given as separation in the  $\phi\eta$ -space, so we define

$$\Delta R = \sqrt{(\Delta\phi)^2 + (\Delta\eta)^2}, \quad (3.10)$$

where  $\Delta\phi$  and  $\Delta\eta$  are the differences in  $\phi$  and  $\eta$  between the two particles.

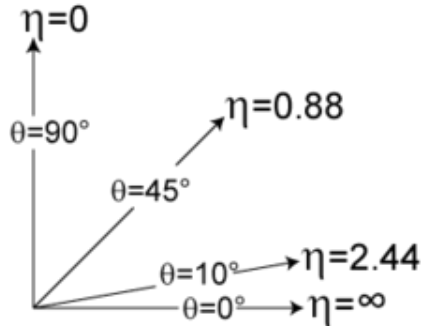


Figure 3.2: Pseudo-rapidity for various values of  $\theta$ , taken from ref. [31].

## 3.2 Proton-Proton interactions

The proton-proton interactions taking place in a collider can roughly be divided into three groups; *elastic*, *diffractive* and *non-diffractive* processes. A process is called elastic if both protons remains unchanged, while in the diffractive processes one or both of the protons are fragmented. Both elastic and diffractive processes are non-perturbative processes (i.e. cross sections can't be calculated by using perturbation

theory), and the mediator is a colour singlet state called a *pomeron*, hence there is no colour exchange between the protons. Also the final state particles tend to move very close to the beams line, thus they are difficult to detect. The present analysis targets processes involving production of heavy particles and final states with high- $p_T$  particles, meaning that elastic and diffractive processes are not considered very interesting. However, they do contribute to the total  $pp$  cross section, and dedicated experiments measure these processes using *minimum bias*<sup>2</sup> events.

The processes we are interested in are non-diffractive events and involve exchange of colour between the partons taking part in the interaction. For producing heavy particles non-diffractive processes with high momentum transfer are of particular interest. These are known as *hard scattering* processes. An example is shown in Figure 3.3, where the result of the hard scattering is two partons with high  $p_T$ .

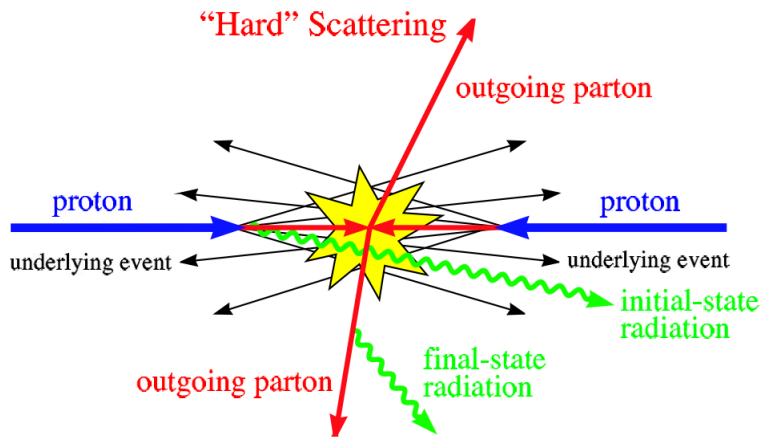


Figure 3.3: Illustration of how a  $pp$  collision might take place, taken from ref. [32].

Figure 3.3 illustrates some other important features of  $pp$  collisions, namely initial-state radiation (ISR), final-state radiation (FSR) and the *underlying event*. By ISR we mean radiation of a gluon or a photon (or in principle also a weak gauge boson) from one of the partons before the hard scattering, while FSR is such radiation from one of the particles produced in the hard interaction. The underlying event, on the other hand, refers to interactions between the partons that are not involved in the hard scattering. These interactions are typically non-perturbative, with resulting particles (not all) moving longitudinally and out of reach of the detector. This means that it is usually not possible to determine the full longitudinal momentum in an event, which is the main reason why we prefer to work only with transverse momentum in analyses, allowing the application of energy-momentum conservation.

---

<sup>2</sup>A minimum bias event is an event where no requirements (i.e. no special triggers) to the final state are introduced.

### 3.2.1 Parton distribution functions

Usually one says that the proton consists of three quarks ( $u$ ,  $u$  and  $d$ ), which are called the *valence* quarks carrying the proton quantum numbers. When the protons are relativistic the quarks are likely to emit gluons, which again split into pairs of quarks and anti-quarks or into two gluons. These quarks are referred to as *sea* quarks.

Each of the proton constituents (valence quarks, sea quarks and gluons) carries a certain fraction of the total momentum of the proton, and the distribution of momentum is described by parton distribution functions (PDFs). These functions give the probability densities for a parton carrying a certain fraction,  $x$ , of the total momentum.

Unfortunately the PDFs cannot be calculated from QCD, and must be determined experimentally. This is usually done in Deep Inelastic Scattering (DIS) experiments, by colliding electrons (or positrons or neutrinos) with protons (or other hadrons). The cross section for  $ep$  DIS depends on the momentum transfer,  $Q^2$ , in the collision, the variable  $y$  given as

$$y = \frac{Q^2}{(s - m_p^2)x},$$

and the structure function  $F_2^{ep}(x)$ . The structure function can be written as

$$F_2^{ep} = x \sum_i Q_i^2 f_i(x), \quad (3.11)$$

where  $i$  is a (valence or sea) quark in the proton,  $Q_i$  is the charge of the quark and  $f_i(x)$  is the corresponding PDF. For a certain value of  $Q^2$  it is then possible to determine  $F_2^{ep}(x)$ . However, what we really are interested in are  $f(x)$  for each of the partons (including gluons). These can be obtained by combining results from different DIS experiments measuring different structure functions that are superpositions of the same  $f_i(x)$ 's. (More details about this can be found in chapter 8 of ref. [9], which this review is based on.) When the PDFs for the relevant quarks are obtained one can extract the gluon PDF from the fraction of momentum not "taken" by the quarks. PDFs for two different values of  $Q^2$  are shown in Figure 3.4. Notice that for large values of  $x$  the "carrier" is likely to be a valence quark, and that the PDFs for quark and anti-quark are equal for the non-valence quarks ( $s\bar{s}$ ,  $c\bar{c}$  and  $b\bar{b}$ ).

### 3.2.2 Hadronization

Quarks and gluons carry colour charge, which means that they are never observed as free particles<sup>3</sup>, but always as colourless objects. The nature of the strong force is such that it increases with distance, meaning that if we try to separate the quarks of a colourless state the energy of the colour field increases, and leads to creation

---

<sup>3</sup>The only exception to this is the top quark, which has a shorter life time than the QCD interaction time scale.

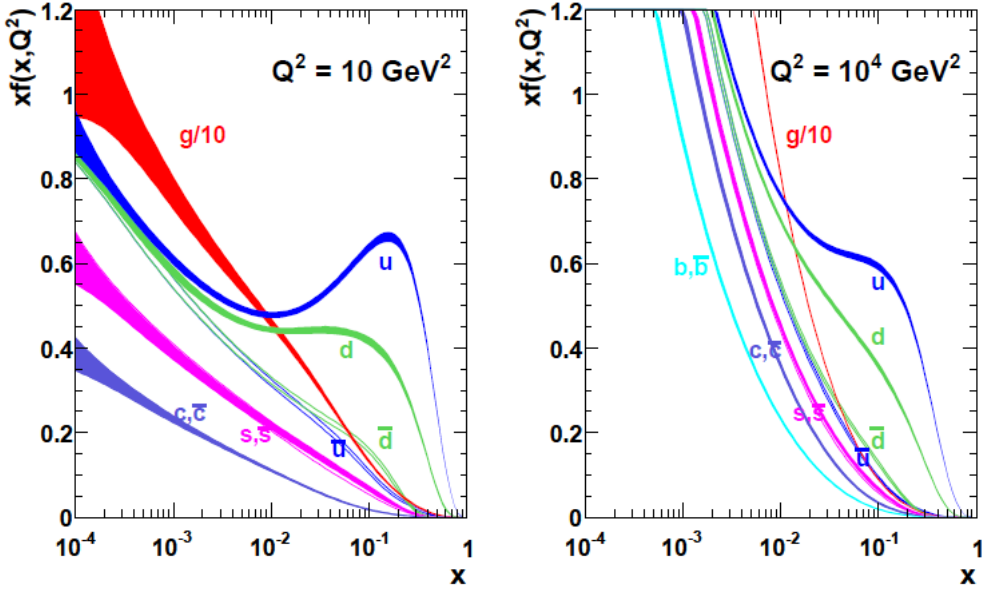


Figure 3.4:  $xf(x)$  for  $Q^2 = 10 \text{ GeV}^2$  and  $Q^2 = 10^4 \text{ GeV}^2$ , found in ref. [33].

of new partons. The quarks emit gluons, and the gluons split into a new pair of quark and anti-quark. This process continues until the partons that are created have low enough energy to form hadrons, hence the name *hadronization*. Usually many hadrons are created in these processes, hence they are often referred to as hadronic showers. An illustration of a hadronization process is shown in Figure 3.5.

In  $pp$  collisions hadronic showers are initiated by partons produced in the hard scattering, but also from the underlying event, as well as from ISR and FSR gluons. For this reason there is usually a lot of things going on in a  $pp$  collision, which makes them a lot more complicated to study than for instance  $e^+e^-$  collisions. In particle detectors the hadronic showers are observed as so-called *jets*, which are further discussed in Section 5.2.3.

### 3.3 Luminosity and pile-up

As mentioned previously  $\sqrt{s}$  is an important parameter when describing the performance of a particle collider. Another key parameter is the luminosity,  $\mathcal{L}$ , which gives the number of collisions per area per second as

$$\mathcal{L} = \frac{n_1 n_2}{4\pi\sigma_x\sigma_y} f, \quad (3.12)$$

where  $n_1$  and  $n_2$  are particles per bunch,  $\sigma_x$  and  $\sigma_y$  are the bunch size in  $x$ - and  $y$ -direction respectively, and  $f$  is the bunch crossing rate. For a certain process with cross section  $\sigma$  the rate,  $R$ , at which this process will occur in a particle collider is given by  $R = \sigma\mathcal{L}$ . A more interesting figure is how many times,  $N$ , this process will occur over a period of time, which is obtained by integrating the luminosity

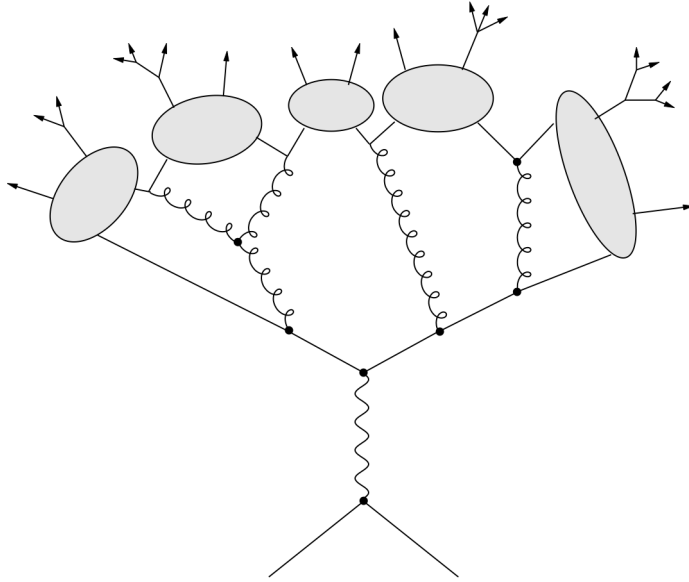


Figure 3.5: Example of how a hadronization process could proceed, found in ref. [35]. The grey ellipses represent the hadrons that are formed, and the arrows going out of them represent their decays into observed (reconstructed) particles.

over time, so

$$N = \sigma \int \mathcal{L} dt. \quad (3.13)$$

The integrated luminosity is commonly used as a measure of how much data a particle detector has collected over a period of time, but rather than sticking to the SI units one gives the number in *inverse femtobarns* ( $\text{fb}^{-1}$ ). This is a practical unit since cross sections also usually are given in barns (with some prefix). The cross section for inelastic  $pp$  collisions at the LHC at  $\sqrt{s} = 13$  TeV is measured by the ATLAS experiment to be about 78 mb [34], which means that an inverse femtobarn of data corresponds to  $\sim 10^{14}$  inelastic  $pp$  collisions.

In experiments at high luminosity it is common to have more than one collision each time two particle bunches cross each other inside the detector. This phenomenon is known as *pile-up*, and complicates the picture further. In events with pile-up it is particularly important with accurate measurements of the particle tracks to determine which collision the individual particles stem from. Usually only one collision per event is used in the analysis, and the vertex corresponding to this collision is known as the *primary vertex*. The requirements to primary vertices used in this analysis are mentioned in Section 5.7.

With the rough overview of  $pp$  collisions given in this chapter in mind, it is time to move on to describing how such collisions are produced by the LHC and recorded with the ATLAS detector.

# Chapter 4

## The Large Hadron Collider and the ATLAS experiment

The data used in this thesis is collected by the ATLAS experiment from proton-proton collisions at the LHC. This chapter gives an overview of the experimental set-up. This includes a short summary of how particles are accelerated and collided at the LHC, and how the ATLAS detector records the collisions, with a look at the main components of the detector. However, before these things are dealt with we should briefly introduce the organisation hosting the experiment, namely CERN.

### 4.1 CERN

CERN (European Organisation for Nuclear Research) is a physics laboratory near Geneva on the border between Switzerland and France. CERN was founded in 1954 [36], and has today 22 member states, with Norway as one of the members since the beginning. In the early years the research done at CERN was related to nuclear physics, as the name indicates. However, as our understanding of nature has developed the main research focus has been shifted towards particle physics, and most famously colliding particles at very high energies.

Amongst the most famous achievements at CERN are the discovery of the neutral currents mediated by the  $Z$ -boson in 1973 [16], the discovery of the  $W$ - and  $Z$ -boson [17, 18, 19], the determination of number of light neutrinos [37], creation and isolation of anti-hydrogen [38, 39], and most recently the discovery of the Higgs boson in 2012 [20, 21]. On the subject of achievements it is also worth mentioning the world wide web, which was developed at CERN by Tim Berners-Lee in the late 1980s [40].

Over the years several different particle accelerators have been built and used at CERN, both circular and linear. The  $W$ - and  $Z$ -boson were both discovered by the UA1 and UA2 experiments at the Super Proton Synchrotron (SPS) in 1983. Following this the Large Electron-Positron Collider (LEP) was built to perform precision measurements on the weak gauge bosons. LEP was operating between 1989 and 2000, and is to this day the largest and most powerful lepton collider ever built, with its  $\sim 27$  km circumference and maximal collision energy of 209 GeV. After LEP was shut down it was replaced by the LHC, which achieved its first

successful proton-proton collision in 2010.

## 4.2 The Large Hadron Collider

The Large Hadron Collider (LHC) [41] is the most powerful particle accelerator ever built. It is also the world's largest machine of any kind. It is most known for accelerating and colliding protons with each other, and this is also what preoccupies most of its time, but it also collides lead ions with each other, as well as lead ions with protons. As mentioned the first collisions took place in 2010, and between 2010 and 2013 the protons were collided at centre-of-mass energies of 7-8 TeV. When *Run 1* of the LHC ended in February 2013, an upgrade of the machine followed. In 2015 it was once again put into life, now able to perform proton-proton collisions at  $\sqrt{s} = 13$  TeV.

Two particle beams circulate in opposite directions in separate beam pipes which cross each other inside the detectors. The beams are guided around the circle by superconducting magnets. In order to acquire superconductivity the magnets are cooled down to  $-271.3^{\circ}\text{C}$  by liquid helium. The main steering is done by 1232 dipole magnets, each about 15 meter long. In addition to these 392 5-7 meter long quadrupole magnets focus the beam to increase the collision probability.

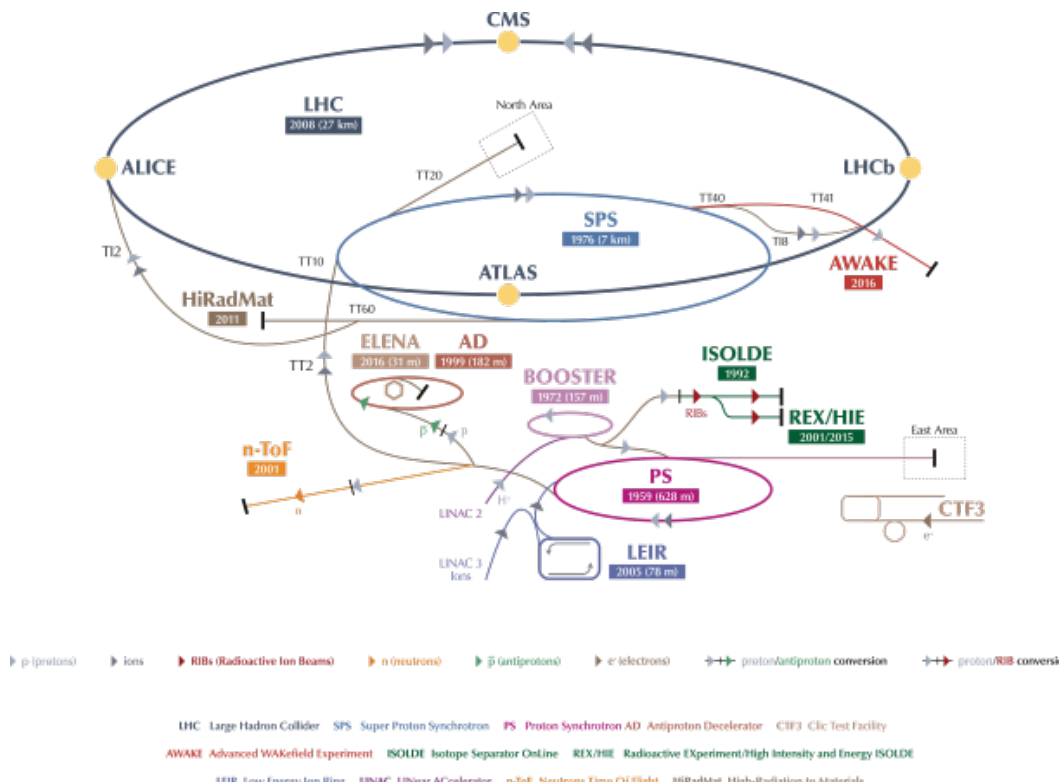


Figure 4.1: The CERN accelerator complex [42].

Because of the strong magnetic fields the particles need to have a certain energy when they enter the LHC. Low energy beams would just be thrown out of the orbit.

For this reason the beams are prepared through a chain of different accelerators [43]. The complete accelerator complex at CERN is shown in Figure 4.1, which also includes accelerators not part of the chain that feeds the LHC. The whole process starts with a bottle of hydrogen gas. Single protons are extracted by removing the electrons from the hydrogen atoms. Then the protons are injected in the LINAC 2 accelerator, which is the only linear accelerator in the chain. Here the protons are accelerated to 50 MeV. Then they enter the Proton Synchrotron Booster (PSB) where they are accelerated to 1.4 GeV. In the Proton Synchrotron (PS) the beam energy is increased to 26 GeV, and here the beam is also separated into bunches. The previously mentioned SPS increases the beam energy to 450 GeV, before the beam finally enters the LHC where the energy is ramped up to the desired energy of 7, 8, 13 and later 14 TeV.

The particles are mostly accelerated using radio frequency (RF) cavities [44]. An RF cavity is a metallic chamber containing an oscillating electromagnetic field. In the LHC these fields oscillate with a frequency of 400 MHz. This frequency is tuned so that particles having the desired energy should not feel any force when they pass through the cavity, while particles with slightly too low or too high energy are accelerated or slowed down respectively. This also ensures that the particles stay in bunches. The LHC is designed to operate with a maximum of 2808 bunches, with  $\sim 10^{11}$  protons per bunch and 25 ns bunch spacing. This corresponds to a luminosity of  $10^{34} \text{ cm}^{-1}\text{s}^{-1}$ . However, towards the end of the 2016 run the LHC was operating regularly about  $\sim 30\%$  [45] above the design luminosity.

Four main experiments are situated along the LHC, marked with yellow dots in Figure 4.1. Two of them, ATLAS (A Toroidal LHC ApparatuS) and CMS (Compact Muon Solenoid), are so-called multi-purpose experiments. These are mainly looking for signs of new physics, like supersymmetry and other exotic phenomena such as new space dimensions. They also have another objective of performing more precise measurements of the properties of the Higgs boson, which they discovered in Run 1.

The other two experiments, ALICE (A Large Ion Collider Experiment) and LHCb (Large Hadron Collider beauty), have more specific tasks. The main goal of ALICE is to study heavy ion collisions (lead-lead and lead-proton) in order to better understand the quark-gluon plasma, which is the state of matter assumed to have existed shortly after the Big Bang. LHCb, on the other hand, is specialised at studying physics processes related to  $b$ -quarks, as the "b" in the name indicates. The aim is to measure precisely  $CP$ -violating processes, and look for other sources of  $CP$ -violation, and hence gain better understanding of the asymmetry between matter and anti-matter in the universe.

### 4.3 The ATLAS detector

ATLAS [46] is the largest detector at the LHC, being 44 m long and 25 m high, and weighing about 7000 tons. It is shaped as a cylinder, covering *almost* a  $4\pi$  solid angle, only interrupted by the beam pipe. The detector can be divided into three parts. The central part is called the *barrel*, and covers the pseudo-rapidity range

up to  $|\eta| \lesssim 2$ , while the two end parts are called *end-caps* and cover  $|\eta| \gtrsim 2$ .

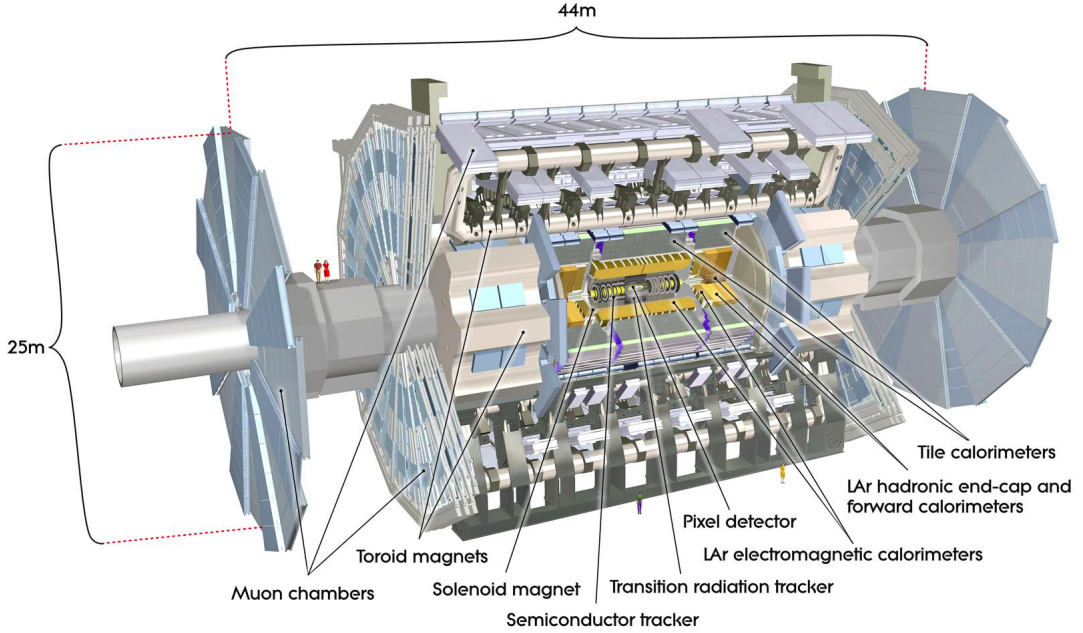


Figure 4.2: The ATLAS detector. [47]

The apparatus is designed to detect everything that is possible to detect from a  $pp$  collision. This requires several different technologies and sub-detectors. A sketch of the detector with pointers to the main components is shown in Figure 4.2. The silicon pixel detector along with the two other tracking detectors (silicon strips and transition radiation detectors) make up what is called the inner detector. The main task of the inner detector is to measure tracks of charged particles and event vertices. The inner detector is surrounded by a solenoid magnet. Then follows the calorimeters. The electromagnetic calorimeter stops electrons and photons, and measures their energy, while the hadronic (tile and LAr) calorimeters do the same for hadrons. The outermost part of the detector is the large toroid magnets and the muon spectrometer, where the muons are detected. An illustration of how the different particles behave in the different parts of the detector is shown in Figure 4.3.

Another very important part of the detector is the trigger system. Since collisions take place at an extremely high rate we can't afford to keep everything that is "seen" by the detector, and the trigger's task is, roughly explained, to decide which events should be kept and recorded, and which ones should be ignored. This, and all the other components mentioned above, will be more carefully discussed throughout the rest of this chapter.

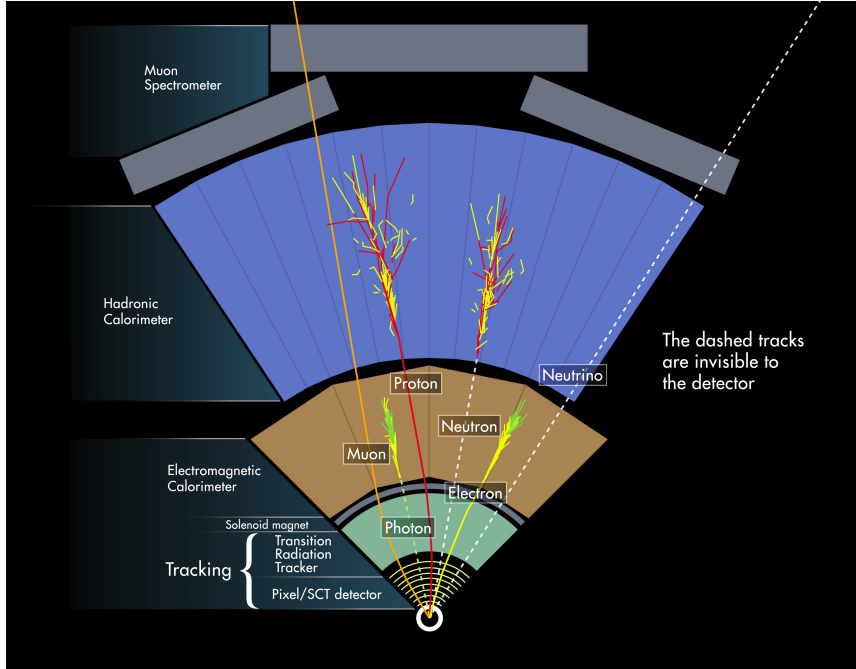


Figure 4.3: An illustration of how the different particles typically "look like" in the detector. [47]

#### 4.3.1 Inner detector

Figure 4.4 shows the inner detector (ID) in some more details. The ID covers the pseudo-rapidity range  $|\eta| < 2.5$ , measures the trajectories of charged particles, and hence reconstructs (primary and secondary) vertices. Since the ID is placed inside the solenoid magnet it is possible to determine the charge and momentum of the particles from the curvature of the tracks.

The resolution of the momentum measurements in the ID is  $\sigma_{pT}/pT = 0.05\% p_T \oplus 1\%$  [46]. The " $\oplus$ "-symbol indicates that the numbers are added in quadrature, i.e.  $a \oplus b = \sqrt{a^2 + b^2}$ . This means that for an electron with  $p_T = 25$  GeV the resolution is  $\sigma_{pT} = 0.4$  GeV. In Section 5.1 we define the invariant mass variable,  $m_{\ell\ell}$ , and we will see that  $m_{\ell\ell} \propto p_{T1}p_{T2}$ , where  $p_{T1}, p_{T2}$  are transverse momenta of two leptons. If i.e.  $p_{T1} = 25$  GeV and  $p_{T2} = 20$  GeV the resolution in invariant mass is  $\sigma_{m_{\ell\ell}}/m_{\ell\ell} \approx 2\%$ .

The part of the ID closest to the collision point is the pixel detector [48], which consists of four layers placed cylindrically around the collision point, and three end-cap disks in each end of the cylinders perpendicular to the beam pipe. The barrel layer closest to the collision point is placed at a radius only about 3 cm from the beam axis. This is called the Insertable B-Layer (IBL) [49] and was installed during the long shut-down of the LHC between 2013 and 2015, in order to be able to perform more precise vertexing, which is the main task of the pixel detector. In total the pixel detector now consists of 1,968 *modules*<sup>1</sup>, with 26,880 pixels per module in the IBL, and 47,232 pixels per module in the other layers of the pixel

---

<sup>1</sup>A module is the basic unit of a detector, consisting of sensors and the necessary readout electronics.

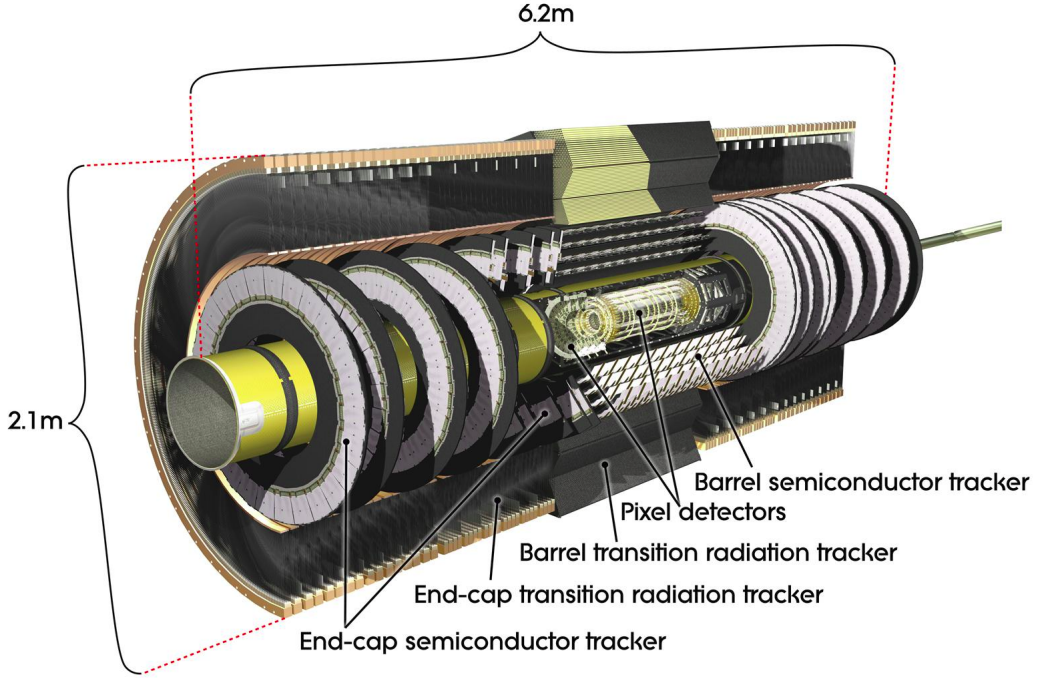


Figure 4.4: The inner detector. [47]

detector. The accuracies of the position measurement are  $10 \mu\text{m}$  in the  $R\phi$ -plane and  $115 \mu\text{m}$  in the  $z$ -plane for the barrel, and  $10 \mu\text{m}$  in the  $R\phi$ -plane and  $115 \mu\text{m}$  in the  $R$ -plane for the disks [46].

Outside the pixel detector follows the Semiconductor Tracker (SCT) [50], which has four barrel layers and nine layers at each end-cap, with a total of 4,088 modules made of silicon micro-strips. In each module two strips are glued together back-to-back at a 40 mrad angle, in order to provide two measurements per hit from a particle, which means that both  $R$  and  $\phi$  can be measured in one module. The accuracy of the measured position in the SCT is  $17 \mu\text{m}$  in the  $R\phi$ -plane and  $580 \mu\text{m}$  in the  $z$ -plane for the barrel, and  $17 \mu\text{m}$  in the  $R\phi$ -plane and  $580 \mu\text{m}$  in the  $R$ -plane for the disks [46].

The outermost part of the ID is the Transition Radiation Tracker (TRT) [51], which consists of 4 mm thick straw tubes filled with a mixture of Xenon,  $\text{CO}_2$  and  $\text{O}_2$ . The barrel has 52,544 144-cm-long tubes parallel to the beam axis, while each end-cap has 122,880 37-cm-long tubes perpendicular to beam. The principle of the TRT is that atoms in the gas are excited by particles passing through, and the resulting free electrons are picked up by a wire in the tube. The accuracy of the track measurements is  $130 \mu\text{m}$  in the  $R\phi$ -plane, which is less than the pixel and SCT detector, but the TRT has more layers, and performs up to 36 measurements per track.

The space between the straw tubes in the TRT is filled with either polymer fibres or foils. This is to make use of *transition radiation*, which is a form of radiation emitted by relativistic particles travelling between media with different dielectric

constants. The transition radiation is absorbed by the Xenon atoms, and gives much stronger signal than the ionisation signal, which means that it is possible to separate the two. The transition radiation depends on the particle's Lorentz factor,  $\gamma = \frac{E}{m}$ , which means that it for instance can be used to separate electrons and charged pions, since a pion with energy  $E$  has a much smaller  $\gamma$  than an electron with the same energy.

### 4.3.2 Calorimeters

The purpose of the calorimeters is to stop particles and measure their energies. For electrons/positrons and photons this happens in the electromagnetic calorimeters (ECal), while for hadrons it is done in the hadronic calorimeters (HCal). However, charged hadrons also deposit energy in the ECal, as well as photons from neutral pion decays. The full calorimeter system is shown in Figure 4.5. Like the inner detectors the calorimeters are also divided into a barrel part and two end-caps. The barrel part consists of an electromagnetic liquid argon (LAr) calorimeter and a hadronic tile calorimeter. The end-caps also have such calorimeters, in addition to a LAr and a forward HCal.

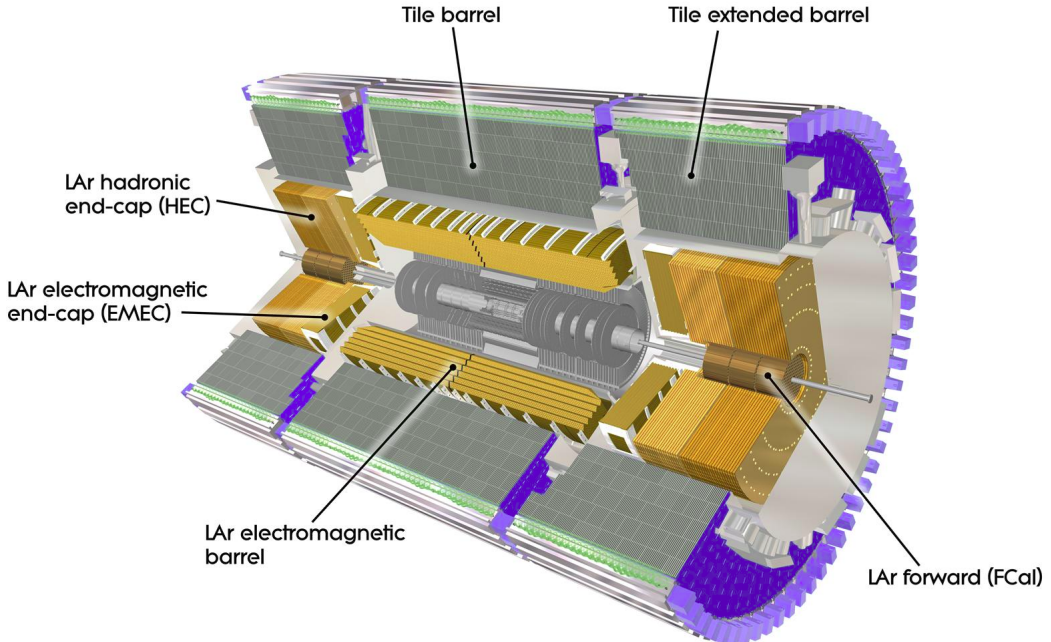


Figure 4.5: The ATLAS calorimeters. [47]

### Electromagnetic calorimeters

The barrel part of the ECal covers  $|\eta| < 1.475$ , while the end-caps cover  $1.375 < |\eta| < 3.2$ . The ECal is made of layers of lead, interleaved with liquid argon. Lead is

called the *passive* medium, while argon is the *active* medium, because interactions mostly take place in the lead layers, and particles produced in these interactions ionizes the argon atoms, and the free electrons are picked up by electrodes. Because of the large amount of energy deposited, both the barrel and the end-caps of the ECal are housed in cryostats to keep them cool.

The thickness of a calorimeter is usually given in *radiation lengths* (ECal) or *interactions lengths* (HCal). The radiation length,  $X_0$ , is the mean length required to reduce the energy,  $E$ , of a particle by a factor  $\frac{1}{E}$  in a certain material. The barrel part of the ECal is  $\geq 22X_0$ , while the end-caps are  $\geq 24X_0$  [46]. The energy resolution of the ECal measurements is  $\sigma_E/E = 10\%/\sqrt{E} \oplus 0.7\%$  [46], meaning that the energy resolution for i.e. a photon with  $E = 10$  GeV is  $\sigma_E = 0.3$  GeV.

The part of the ECal that covers  $|\eta| < 2.5$  is designed for precision measurements, which means that it has somewhat finer granularity in terms of number of detector cells, than the rest of the  $\eta$  range.

### **Hadronic calorimeters**

The hadronic calorimeter system contains three different parts. Two of them, the hadronic end-cap (HEC) and the forward calorimeter (FCal), make use of the same technology as the ECal. They are both housed in the same cryostats as the end-cap ECals, and use liquid argon as the active medium. The HEC is placed just outside the ECal end-caps, and uses copper as the passive medium. It covers the pseudo-rapidity range from  $|\eta| = 1.5$  to  $|\eta| = 3.2$ .

The FCal is "wrapped" around the beam pipe in each of the end-caps, and covers the range from  $|\eta| = 3.1$  and up to  $|\eta| = 4.9$ . Each FCal is divided in three modules. The first module uses copper as the absorbing material, and is optimised for electromagnetic measurements, while the two others use tungsten, and are designed for hadronic interactions.

Finally, the hadronic tile calorimeter consists of a barrel part and so-called "extended barrels" at each side of the barrel. The barrel covers  $|\eta| < 1.0$  and the extended barrels covers  $0.8 < |\eta| < 1.7$ . The absorbing material is steel, while the active material is scintillating tiles. The basic working principle is that atoms in the tiles are excited by the passing particles, and as the atoms fall back into their ground state they emit radiation that is detected by photomultiplier tubes. The interaction length,  $\lambda$ , is the mean distance a particle travels before interacting strongly with the material. The thickness of the tile calorimeter at  $\eta = 0$  is  $9.7\lambda$  [46].

The energy resolution for the barrel and HEC calorimeters is  $\sigma_E/E = 50\%/\sqrt{E} \oplus 3\%$ , while it is  $\sigma_E/E = 100\%/\sqrt{E} \oplus 10\%$  for the FCal [46]. The energy resolution in the barrel calorimeter for a jet with  $E = 20$  GeV is then  $\sigma_E = 2.3$  GeV. This is usually an important source of systematic uncertainties, in particular if the final state of the analysis involves jets.

### **4.3.3 Muon spectrometer**

The largest part of the ATLAS detector is the Muon Spectrometer (MS) [46], which is shown in Figure 4.6. As for the other parts of the detector the MS can be divided

in a barrel part and two end-caps. The barrel consists of three cylindrical layers located about 5 m, 7.5 m and 10 m from the beam axis, while each end-cap consists of three disks perpendicular to the beam axis located about 7 m, 14 m and 21 m from the interaction point.

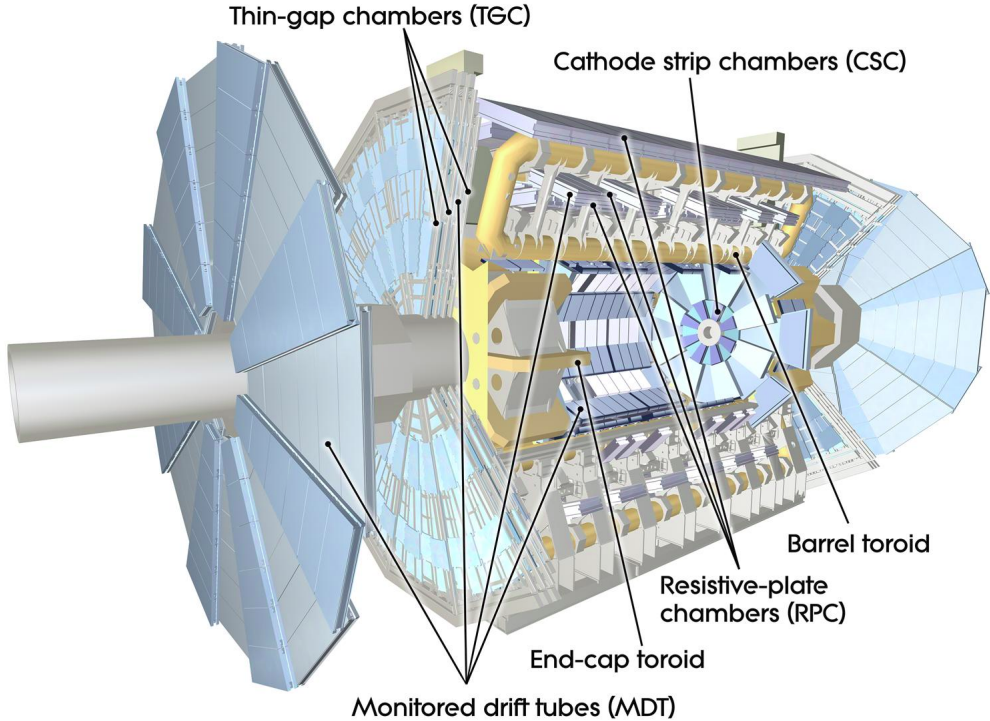


Figure 4.6: The ATLAS muon spectrometer. [47]

The purpose of the MS is to detect charged particles escaping the calorimeters. It is designed to both do precise measurements on such particles and to provide information allowing to trigger on them. The precision measurements are done in the Monitored Drift Tubes (MDT) and the Cathode Strip Chambers (CSC), which cover up to  $|\eta| = 2.7$ , while triggering is done in the Resistive Plate Chambers (RPC) and the Thin Gap Chambers (TGC), which cover the range  $|\eta| < 2.4$ . The momentum resolution of the MS is  $\sigma_{pT}/p_T = 10\%$  at  $p_T = 1 \text{ TeV}$  [46].

#### 4.3.4 Magnets

As mentioned in section 4.3.1 the ID is placed inside a solenoid magnet, providing the trajectories a 2 T magnetic field parallel to the beam line. This enables measurements of charge and momentum of particles transversing the ID.

In addition to the solenoid the ATLAS magnet system (Fig. 4.7) consists of three toroidal magnets; one barrel toroid and two end-cap toroids. The toroids serve the same purpose for the MS as the solenoid does for the ID. The barrel toroid is placed around the middle cylinder of the MS barrel (see Fig. 4.6), while the end-cap toroids are placed between the MS disks at 7 m and 14 m.

The barrel toroid sets up a magnetic field of 0.5 T that covers the range  $|\eta| < 1.4$ , while each end-cap toroid sets up a field of 1 T that covers  $1.6 < |\eta| < 2.7$ . The region  $1.4 < |\eta| < 1.6$  is covered by a combination of fields from end-caps and barrel.

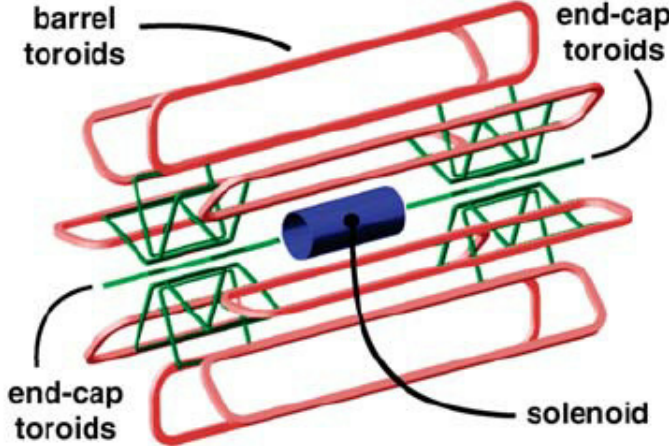


Figure 4.7: The magnet system in ATLAS [53].

#### 4.3.5 Trigger system

With bunch crossings every 25 ns the expected event rate is 40 MHz, but because of data storage capacity "only" about 1 kHz (i.e one in 40,000 events) can be kept for further detailed analysis [52]. This means that a system that decides which events can be regarded as interesting enough to keep is needed. This is exactly the purpose of the triggers. The trigger system consists of two different levels; the Level-1 (L1) trigger and the High-Level Trigger (HLT).

The L1 trigger reduces the event rate to about 100 kHz, and is implemented in the hardware of the detector. It uses information from the RPC, TGC and the calorimeters to search for events with muons, electrons, photons and jets with high transverse momentum, as well as tau leptons decaying hadronically and events with high total transverse momentum or large missing transverse energy. The L1 trigger also defines so-called Regions-of-Interest (RoI's), which are based on the  $\phi$  and  $\eta$  coordinates of the "stuff" it has defined as interesting.

The L1 trigger must decide whether or not an event is interesting *before* the next event occurs, i.e. within 25 ns, and the decision must be passed on within 2.5  $\mu$ s. If an event is accepted by the L1 trigger the event information is sent to the Read-Out-System (ROS) to be accessed by the software based HLT. The HLT makes use of the RoI's defined by the L1 trigger, and all the data from the different detector parts within the given RoI is extracted, and then used to further reduce the event rate to 1 kHz. The average HLT processing time is about 0.2 s per event [52]. Events that pass the HLT are stored for further processing off-line.

Now it is time to see what can be found in all the data collected by the ATLAS experiment over the past few years. This will be the topic of the remaining chapters.

# Chapter 5

## Direct Slepton Search Procedure

This chapter aims to describe in an appropriate detailed way all the necessary ingredients of the analysis. This includes which kinematic variables are used, which objects we consider and how they are defined, how the background is simulated, which data and simulated SUSY signals we use, and a first selection of events to be used in the analysis.

### 5.1 Kinematics

In Section 3.1 we introduced  $p_T$ ,  $\eta$  and  $\phi$  as the basic variables used for describing the kinematic properties of a particle. To describe collision events we use several variables that are calculated using the basic variables (possibly together with the mass,  $m$ , of the particle). One of these variables is the *missing transverse momentum*,  $\mathbf{p}_T^{miss}$ , which is defined as the negative sum of transverse momentum,  $\mathbf{p}_T$ , of all the particles in the event,

$$\mathbf{p}_T^{miss} = - \sum \mathbf{p}_T. \quad (5.1)$$

In this analysis we use the *missing transverse energy*, which is defined as the magnitude of the missing transverse momentum, i.e.  $E_T^{miss} = |\mathbf{p}_T^{miss}|$ .

One of the most important variables is the invariant mass, which is derived from the Einstein formula (Eq. 3.2) applied on a two-particle system, e.g. two leptons  $\ell^+$  and  $\ell^-$ . By rewriting the Einstein formula slightly we arrive to

$$m(\ell^+\ell^-) = \sqrt{(E_{\ell^+} + E_{\ell^-})^2 - (\mathbf{p}_{\ell^+} + \mathbf{p}_{\ell^-})^2} \equiv m_{\ell\ell}, \quad (5.2)$$

which can be expressed in terms of the standard variables  $p_T$ ,  $\eta$  and  $\phi$  as

$$m_{\ell\ell} = 2p_{T1}p_{T2}(\cosh(\eta_1 - \eta_2) - \cos(\phi_1 - \phi_2)), \quad (5.3)$$

where 1, 2 is just another way of labelling the two leptons.

A quantity closely related to the invariant mass is the *transverse mass*,  $m_T$ . This is a particular useful quantity if we have a two-particle system where one of the particles is undetectable in the experiment. The classical example is a  $W$ -boson decaying to a charged lepton,  $\ell$ , and a neutrino,  $\nu$ . The transverse mass is defined

by taking the invariant mass (e.g. equation 5.2), and restricting the variables to the transverse plane, so in the  $W$ -case it is given as

$$m_T = \sqrt{(E_{T,\ell} + E_{T,\nu})^2 - (\mathbf{p}_{T,\ell} + \mathbf{p}_{T,\nu})^2}. \quad (5.4)$$

By using the definition of transverse energy (Eq. 3.7), and substituting for  $E_{T,\ell}$  and  $E_{T,\nu}$  in Equation 5.4, we get

$$m_T = \sqrt{m_\ell^2 + m_\nu^2 + 2(E_{T,\ell}E_{T,\nu} - \mathbf{p}_{T,\ell}\mathbf{p}_{T,\nu})}. \quad (5.5)$$

By assuming that the lepton masses are negligible we get  $E_T = |\mathbf{p}_T|$ , hence

$$m_T = \sqrt{2E_{T,\ell}E_{T,\nu}(1 - \cos\phi_{\ell,\nu})}, \quad (5.6)$$

where  $\phi_{\ell,\nu}$  is the angle between the two particles in the transverse plane. The maximal value of  $m_T$  is the mass of the  $W$ -boson, given that  $\ell$  and  $\nu$  actually comes from a  $W$ .

To include systems with more than one invisible particle in the final state the transverse mass can be extended through the  $M_{T2}$  variable [54], which is sometimes referred to as the *stransverse* mass. This is a highly relevant variable in SUSY searches, as production of SUSY particles often leads to final states with two (invisible) neutralinos, which is also the case in the signal final state considered in this thesis, where we have  $\tilde{\ell}\tilde{\ell} \rightarrow \ell\tilde{\chi}_1^0\ell\tilde{\chi}_1^0$ . If we consider only one of the slepton decays ( $\ell \rightarrow \ell\tilde{\chi}_1^0$ ), we can write the transverse mass as

$$m_T(\mathbf{p}_T^\ell, \mathbf{q}_T^{\tilde{\chi}_1^0}; m_{\tilde{\chi}_1^0}) = \sqrt{m_\ell^2 + m_{\tilde{\chi}_1^0}^2 + 2(E_T^\ell E_T^{\tilde{\chi}_1^0} - \mathbf{p}_T^\ell \mathbf{p}_T^{\tilde{\chi}_1^0})}, \quad (5.7)$$

and we have  $m_T \leq m_{\tilde{\ell}}$ . Since we don't know the mass of the neutralino we have to introduce a test-mass,  $m_\chi$ , which is a free variable. Further more we don't know the momentum of the neutralino. The only thing we know about the neutralinos is the sum of transverse momenta,  $\mathbf{p}_T^{miss} = \mathbf{q}_T^{\chi_1} + \mathbf{q}_T^{\chi_2}$ , where  $\chi_1, \chi_2$  represents the two neutralinos.  $M_{T2}$  is defined as the largest of the two transverse masses, *after* a minimisation using all possible  $\mathbf{q}_T^{\chi_1}$  and  $\mathbf{q}_T^{\chi_2}$ . Mathematically this can be expressed as

$$M_{T2} \equiv \min_{\mathbf{p}_T^{miss} = \mathbf{q}_T^{\chi_1} + \mathbf{q}_T^{\chi_2}} \{ \max[m_T(\mathbf{p}_T^{\ell_1}, \mathbf{q}_T^{\chi_1}; m_\chi), m_T(\mathbf{p}_T^{\ell_2}, \mathbf{q}_T^{\chi_2}; m_\chi)] \}. \quad (5.8)$$

If  $m_\chi = m_{\tilde{\chi}_1^0}$  the  $M_{T2}$  variable works like transverse mass, in the sense that  $M_{T2} \leq m_{\tilde{\ell}}$  [54]. The algorithm [55] used for  $M_{T2}$  calculations in this thesis assumes  $m_\chi = 0$ , which is the most conservative choice given that  $m_{\tilde{\chi}_1^0}$  is unknown [56].

Another kinematic variable worth mentioning is the effective mass. In general the effective mass is the sum of missing transverse energy and transverse momentum of leptons and jets in the considered final state, so in this analysis

$$M_{eff} = p_{T1} + p_{T2} + E_T^{miss}. \quad (5.9)$$

Table 5.1 includes a range of other important variables and characteristics describing the particles and their tracks, as well as clusters and energy deposits. These

variables are not used directly in the analysis, but they are e.g. used in the definitions of the physics objects we consider. (See section 5.3.)

$z_0$	Longitudinal impact parameter. Distance along $z$ -axis between the primary vertex and the point where the track crosses the beam line ( $z$ -axis).
$d_0$	Transverse impact parameter. Distance in the transverse plane from the primary vertex to the point where the particle track is closest to the primary vertex.
$\theta$	Angle between the particle track and the beam line. Notice that $z_0 \sin \theta$ gives the closest distance between the track and the primary vertex in the longitudinal plane.
$q/p, \sigma(q/p)$	The charge divided by the momentum, and the related uncertainty $\sigma(q/p)$ .

Table 5.1: List of parameters characterising the particle tracks.

## 5.2 Object reconstruction and identification

Particles are registered by the ATLAS detector as electrical signals. A very important task is then to understand these signals, translate them into physics observables and determine what kind of particles caused them. Therefore we need a set of identification requirements for the different particles. This is a very complicated procedure, and only a brief summary concerning the details most relevant to this analysis is given in the following section.

### 5.2.1 Electrons

Electrons typically leave tracks in the ID, before they are stopped in the ECal. In the ECal the electrons initiate an electromagnetic shower through a phenomenon called *brehmsstrahlung*. This is a process where the electron emits a photon (i.e. loses energy). The photon typically pair-produces an  $e^+e^-$ , and these again emit brehmsstrahlung. This process continues until all the initial energy is entirely absorbed in the ECal. The electromagnetic showers cause a lot of energy deposits in the calorimeter, and a grouping of such deposits is called a *cluster*.

Clusters are compared to tracks in the ID using the  $\Delta R$  variable defined in Equation 3.10. If it is found that a cluster has a matching track in the ID it is an electron candidate. If the cluster does not match a track it is likely to come from a photon, which can also initiate electromagnetic showers.

Further, the identification requirements of electrons are divided into three different levels; **loose**, **medium** and **tight**. Objects passing the **medium** requirement have also passed the **loose** one, and particles passing **tight** have passed both **medium** and **loose**. This classification is done through a likelihood algorithm, which makes use of probability distribution functions for the relevant variables, such as  $E/p$  and some shower profile variables. A probability for the considered signal to actually

come from an electron is then calculated. For a more detailed explanation see ref. [57].

Along with the identification requirements we also apply isolation requirements for electrons used in the analysis. This allows (to some extent) separation between real electrons and other objects that have been wrongly identified as electrons, mainly converted photons and jets. Two different isolation variables are used, called  $E_T^{cone0.2}$  and  $p_T^{varcone0.2}$ . Roughly explained  $E_T^{cone0.2}$  is the sum of transverse energies of clusters within  $\Delta R = 0.2$  from the electron candidate, while  $p_T^{varcone0.2}$  is the sum of  $p_T$  of tracks within a cone of  $\Delta R = \min(0.2, 10\text{GeV}/E_T)$ . Different isolation criteria are defined by selections on the quantities  $E_T^{cone0.2}/E_T$  and  $p_T^{varcone0.2}/E_T$ . Further details can be found in ref. [57].

### 5.2.2 Muons

The main idea of muon reconstruction is to match hits in the muon spectrometer (MS) to tracks in the ID, while also considering their energy loss in the calorimeters. Four types of muons are defined:

- **Combined (CB) muon:** A track in the ID is successfully combined with a track in the MS.
- **Segment-Tagged (ST) muon:** A track in the ID can be combined with a hit in at least one segment of the MS, like the MDT or CSC.
- **Calorimeter-Tagged (CT) muon:** A track in the ID matched with energy deposits in the calorimeter corresponding to a minimum ionizing particle.
- **Stand-Alone (SA) muon:** A track only reconstructed in the MS.

The muon identification is divided into four different selections: `loose`, `medium`, `tight` and `High- $p_T$` . The selections are (amongst other) defined by which type(s) of muons they accept, how many hits in the MS they require and compatibility between MS and ID tracks. The exact definitions of these are found in ref. [58].

In this analysis only the `medium` selection is considered, which uses only SA and CB muons. SA muons are used in the region  $2.5 < |\eta| < 2.7$ , and are required to have at least three hits in each of the three layers of the MDT or CSC. CB muons are required to have at least three hits in two of the MDT layers, unless  $|\eta| < 0.1$ , then it is sufficient with at least three hits in at least one of the MDT layers.

Isolation requirements are applied also to muons. The selection criteria are defined by  $p_T^{varcone30}/p_T$  and  $E_T^{topocone20}/p_T$ , where (roughly explained)  $p_T^{varcone30}$  is the sum of  $p_T$  of tracks within  $\Delta R = 10\text{GeV}/p_T^\mu$  (maximally 0.3) from the muon candidate, while  $E_T^{topocone20}$  is sum of energy deposits at distance  $0.1 < \Delta R < 0.2$ . Energy deposits at  $\Delta R < 0.1$  are not considered as they are likely to come from the muon itself. For more details see ref. [58].

### 5.2.3 Jets

Before explaining how jets are reconstructed and identified it is appropriate with a few words on what a jet actually is. Unlike an electron or a muon a jet is not

a single particle, but rather a bundle of particles produced by strong interactions, as a result of the confinement of quarks and gluons. A jet does however originate from a single particle, namely a parton (quark, anti-quark or gluon) produced in proton-proton collisions. Since partons are coloured objects, they can't propagate freely away from each other. As they travel in different directions the color field between them will soon have enough energy to create new quark-antiquark pairs. This process continues until the partons have low enough energy to form hadrons. The hadrons are then detected through energy deposits in the hadronic calorimeter (HCal), and the ECal for the electromagnetic part due to e.g.  $\pi^0$  decaying to two photons.

The stopping process that takes place in the HCal is somewhat similar to the electromagnetic brehmsstrahlung process described earlier. Only difference being that the former is solely due to the strong interaction, through emission of charged pions. While the brehmsstrahlung is a pure  $e\gamma$  process, the hadrons can loose energy both through the strong and electroweak interactions in the HCal.

One should be aware that jets do not only come from the hard parton-parton scattering process. They could also be caused by initial state radiation, final state radiation, the underlying event or pile-up events.

In ATLAS jets are reconstructed from clusters in the HCal using the anti- $k_t$  algorithm [59]. This algorithm takes  $R$ , which defines the width of the jet cone, as input parameter. In the SUSY group the value is chosen to be  $R = 0.4$ .

### ***b*-jets**

After a jet is reconstructed it would certainly be interesting for most physics analyses to know which type of quark the jet originated from. Unfortunately this is not possible in most cases. However, an exception occurs if the initial quark is a *b*-quark<sup>1</sup>. The procedure of identifying jets comming from *b*-quarks is called *b*-tagging.

The *b*-quark is relatively heavy, so if a  $b\bar{b}$  pair is produced in a  $pp$  collision it most likely forms a *b*-hadron. This hadron travels a short distance before it decays, and jets are produced like described above. This gives rise to a *secondary vertex*. Identifying such vertices is an important part of the *b*-tagging.

The *b*-tagging used in this analysis relies on the MV2c10 algorithm [60, 61]. In addition to secondary vertices the algorithm also makes use of impact parameters in the tagging procedure. The efficiency of the algorithm depends on cuts in the variable used in the algorithm. The requirement used in this analysis is such that the average tagging efficiency is 77%, estimated using simulated  $t\bar{t}$  events.

Being able to separate *b*-jets from light-flavoured jets is a very important ingredient in this analysis. As we will see in Section 5.6  $t\bar{t}$  production is an important part of the background, and since the top quark is most likely to decay to a *b*-quark (plus a *W*-boson) the *b*-tagging provides a nice way of dealing with the  $t\bar{t}$  background.

---

<sup>1</sup>Strictly speaking it is also possible for *c*-quarks, but this is even more difficult.

### 5.2.4 Missing transverse energy

Some particles are unfortunately not possible to detect in ATLAS, and simply escape the detector without leaving any tracks or energy deposits. Such particles must be only weakly interacting, and stable enough to leave the detector without decaying to detectable particles. In the Standard Model this concerns only the neutrinos, while in many SUSY models it also applies to the LSP, which is the neutralino in this search.

Although we can't detect these particles directly it is possible to get a hint about whether or not such particles have been present in an event. This is done by looking at the sum of transverse momenta. Since the collision takes place in the longitudinal direction, the vectorial sum of transverse momenta should be zero in an event. If this is not the case it is an indication that "invisible" particles were produced in the event, but it could also be caused by uncertainties in the determination of jet energies or other sources of mis-measurements. The definitions of missing transverse momentum and energy were given in Section 5.1.

## 5.3 Object definitions

In this section the definitions of the various physics objects used in the analysis are given. Object definitions for electrons, muons and jets are presented in Tables 5.2, 5.3 and 5.4. Specific comments to each of the tables are given in the individual sections, but first a few general comments:

- "PID" is short for "Particle IDentification".
- Several of the variables ( $z_0$ ,  $d_0$ ,  $\theta$ ) used in the tables are defined in Table 5.1, while  $p_T$  and  $\eta$  as usual represent transverse momentum and pseudo-rapidity, respectively.

### 5.3.1 Electrons

The electron object definitions are presented in Table 5.2. The LLH-part of the PID quality means "likelihood", and refers to the fact that the particle identification is done using a likelihood algorithm, as mentioned in Section 5.2.1. `LooseAndBLayer` means that a hit in the B-Layer of the detector is required, in addition to the `Loose` requirement. The definitions of the `Loose` and `Medium` identification requirements, and the `GradientLoose` isolation requirement are given in ref. [57].

### 5.3.2 Muons

The muon object definitions are presented in Table 5.3. The definitions of the PID quality requirements and the isolation requirement can be found in ref. [58].

<b>Baseline electron</b>	
Acceptance	$p_T > 10 \text{ GeV}$ , $ \eta^{\text{cluster}}  < 2.47$
PID Quality	<b>LooseAndBLayerLLH</b>
<b>Signal electron</b>	
Acceptance	$p_T > 10 \text{ GeV}$ , $ \eta^{\text{cluster}}  < 2.47$
PID Quality	<b>LLHMedium</b>
Isolation	<b>GradientLoose</b>
Impact parameter	$ z_0 \sin \theta  < 0.5 \text{ mm}$ $ d_0/\sigma_{d_0}  < 5$

Table 5.2: Object definitions for baseline and signal electrons.

<b>Baseline muon</b>	
Acceptance	$p_T > 10 \text{ GeV}$ , $ \eta  < 2.4$
PID Quality	<b>Medium</b>
<b>Signal muon</b>	
Acceptance	$p_T > 10 \text{ GeV}$ , $ \eta  < 2.4$
PID Quality	<b>Medium</b>
Isolation	<b>GradientLoose</b>
Impact parameter	$ z_0 \sin \theta  < 0.5 \text{ mm}$ $ d_0/\sigma_{d_0}  < 3$

Table 5.3: Object definitions for baseline and signal muons.

### 5.3.3 Jets

The object definitions for jets and  $b$ -jets are given in Table 5.4. `AntiKt4EMTopo` indicates that the anti- $k_t$  algorithm is used with  $R = 0.4$  and topological clusters calibrated at the electromagnetic scale [85].

JVT is short for "Jet-Vertex-Tagger" [86], which is a variable designed to discriminate between jets from the primary vertex and pile-up jets.

The MV2c10  $b$ -tagging algorithm was briefly mentioned in section 5.2.3, and details can be found in ref. [60].

<b>Baseline jet</b>	
Collection	<code>AntiKt4EMTopo</code>
Acceptance	$p_T > 20 \text{ GeV}$ , $ \eta  < 4.5$
<b>Signal jet</b>	
JVT	$ \text{JVT}  > 0.59$ for jets with $p_T < 60 \text{ GeV}$ and $ \eta  < 2.4$
<b>Signal <math>b</math>-jet</b>	
$b$ -tagger Algorithm	<code>MV2c10</code>
Efficiency	77%

Table 5.4: Object definitions for baseline jets, signal jets and  $b$ -jets.

### 5.3.4 Missing $E_T$

The missing transverse momentum is calculated by the SUSYTools method GetMet. The inputs to this method are the other object containers (electrons, muons, jets and photons) in the event. These objects are required to satisfy the baseline criteria defined in Tables 5.2, 5.3 and 5.4.

### 5.3.5 Overlap removal

In addition, to satisfy the baseline criteria given above, electrons, muons and jets must also pass an *overlap removal* before we include them in the analysis. This is to prevent that any object is counted twice in the baseline selection (see Sec. 5.7). The overlap removal is done by the `OverlapRemoval` method in SUSYTools, taking electron, muon and jet containers as input, and flags objects with "passOR" if they pass the overlap removal. The procedure is mainly based on requirements to the separation,  $\Delta R$ , between objects, and can be summarized in the following steps:

1. An electron sharing an ID track with a muon is removed.
2. A jet within  $\Delta R = 0.2$  of a lepton is removed, as they it is likely to come from electron showers or muon brehmsstrahlung. An exception to this occurs if the jet is *b*-tagged. Then the lepton is removed, since it is likely to come from weak *b*-hadron decay.
3. If a jet survived the previous step, and there is an electron within  $\Delta R = 0.4$  of the jet, the electron is removed since it is likely to come from some weak hadron decay.
4. A jet with fewer than three associated tracks, or a nearby muon that carries more than 70% of the sum of transverse momenta of the jet tracks, is removed either if it is within  $\Delta R = 0.2$  of the muon, or if the muon is matched to one of its tracks.
5. If a jet survived the previous step, and there is a muon within  $\Delta R = 0.4$  of the jet, the muon is removed as it is likely to come from a weak hadron decay.

## 5.4 Data files and software tools

This section, in a simple manner, goes through the infrastructure of the analysis. This includes what kind of data files are used and which software is used, and also the basic steps of the analysis, i.e. a short "road map" of how to get from the input files and all the way to the histograms presented later in the thesis.

The basic files used to store data produced by ATLAS are called *Analysis object data* (AOD) files. The files are made in a format called xAOD, which is readable by the ROOT data analysis framework. The AOD files contain all events that were kept by the detector during the data taking or simulations. As one can imagine these files are massive, and not suited for use by the individual analyser. For this purpose smaller samples are constructed, called derived AOD (DAOD) files. In the

derivations (i.e. the DAODs) only the information needed for a certain kind of analysis is kept. The DAODs used in this analysis are "SUSY2"-derivations, which are made specifically for SUSY multi-lepton analyses. The DAODs are labelled with a *production tag* (p-tag), indicating which software version they were produced with. The data samples used in this analysis have p-tag 2880, while the MC (background and signal) samples have p-tag 2879, but coming from the same software release (AtlasDerivation 20.7.8.2).

The first step of the analysis is to run over the DAOD files in order to produce so-called ROOT *nTuples*. In this analysis this is done using release 20.7 of the ATLAS software, with the following set-up:

- rcSetup Base,2.4.29
- SUSYTools-00-08-58

The software runs through all the events in the DAOD. If an event passes the baseline selection (see section 5.7) we keep the event, and store relevant variables and other useful information in the nTuple. A single DAOD is quite big (even though it is much smaller than an AOD), hence the full data set and the full set of background samples are way too big to store on a local computer. For this reason the first part of the analysis is done on the World-Wide LHC Computing Grid<sup>2</sup>. When the jobs are done the nTuples can be downloaded and analysed locally.

At this stage the *real* analysis begins. So far we have only been preparing the data we want to use. The files are now once again run over event by event. This is done by using the `TSelector` class in ROOT. In this part all the additional cuts we want to apply are implemented, and the relevant histograms are made.

The last part is to produce plots, which is done in a Python script, using pyROOT. Here the different backgrounds are scaled (see sec. 5.6.12) and stacked on top of each other, and then visualised along with data and/or simulated signals.

## The data set

The data set used in the analysis consists of  $36.1 \text{ fb}^{-1}$  of data from proton-proton collisions at  $\sqrt{s} = 13 \text{ TeV}$  that was recorded by the ATLAS detector during the LHC runs in 2015 and 2016. An integrated luminosity of  $3.21 \text{ fb}^{-1}$  of data suitable for analysis was collected in 2015, while a record breaking  $32.86 \text{ fb}^{-1}$  was collected in 2016.

The entire data set used appears on the *Good Runs List* (GRL). A "run" corresponds to one single filling of the LHC, and usually gives several hours of data taking for ATLAS. A run is represented on the GRL if both LHC and ATLAS were operating with sufficient precision for at least some part of the run. For the 2015 data set 65 runs with run numbers between 276262 and 284484 appears in the GRL, while in 2016 150 runs with run numbers between 297730 and 311481 made it to the GRL.

---

<sup>2</sup>Mostly just referred to as "the grid", a distributed infrastructure used for large computing and data processing jobs, as well as storage of data.

## 5.5 SUSY signal samples

In general there are several reasons for looking at simulated signals. Firstly we need to characterize the signals in order to figure out how to search for them. Then, if we observe an excess in the search it is nice to determine which model (if any) best fits the data. In the opposite case, if no excess is observed, the simulated signals are used to put exclusion limits on the parameters of the model being studied.

Simulated signal points for 49 different combinations of the slepton mass ( $m_{\tilde{\ell}}$ ) and the neutralino mass ( $m_{\tilde{\chi}_1^0}$ ) are used. Since we assume production of on-shell sleptons we must have  $m_{\tilde{\ell}} > m_{\tilde{\chi}_1^0}$ . The difference between these masses is called the *mass splitting*. Some scenarios (meaning choice of mass pairs) have high mass splittings, meaning the neutralino is relatively light ( $\sim 1$  GeV) and the slepton is heavy ( $\sim$  a few hundred GeV), while other scenarios operate with intermediate mass splitting, typically meaning that the mass difference is  $\sim 50$ -100 GeV. We do not look at scenarios where the slepton and the neutralino are very close in mass. In such scenarios the resulting leptons are likely to be *soft*, meaning that they have low momentum, and therefore difficult to study with ATLAS.<sup>3</sup> A table of the samples used, including the masses and cross sections, can be found in Appendix A.2.

The signal samples are generated with MADGRAPH v2.2.3 [78] and PYTHIA 8.186 [77]. MADGRAPH is used to simulate the production of two sleptons using leading order matrix elements. PYTHIA is used for simulation of the decay, as well as the rest of the event, like hadronisation and the underlying event.

Six different scenarios for direct slepton production are considered. The sleptons can be either  $\tilde{e}$ 's,  $\tilde{\mu}$ 's or  $\tilde{\tau}$ 's, and they can belong to supermultiplets with either left- or right-handed leptons, as mentioned in Chapter 2. The different supermultiplets couple differently to the  $Z$ -boson, which means that the cross section is different for production of "left-handed" and "right-handed" sleptons. However, it is assumed that the cross sections are the same for the different slepton flavours, and that all six sleptons are mass degenerate.

The signal samples are weighted and scaled to the right luminosity and cross section, in a similar manner that is described in the next section, once the background processes are presented.

## 5.6 Standard Model backgrounds

This section presents the Standard Model backgrounds. This include an overview of the various processes we consider and how they are simulated and reconstructed, and how the resulting events/samples are scaled and weighted. Lists of all the background samples used can be found in Appendix A.1.

The simulation of background (and signal) samples are done in two steps. First, events are simulated with an event generator. The event generators that are used for the different backgrounds are mentioned in the following when specific backgrounds are discussed. Second, the response of the ATLAS detector is simulated

---

<sup>3</sup>Dedicated methods beyond the scope of this thesis are being tried to tackle these low mass splitting scenarios.

[62]. The ATLAS simulations are based on GEANT4 [63], which is a toolkit used for simulations of particles passing through matter. Notice that for the signal samples discussed in the previous section a *fast* simulation [64] of the ATLAS calorimeter system is used. Events are reconstructed in the same way as described in Section 5.2.

Towards the end of this section we also consider the possible contributions from fake lepton background, i.e. leptons coming from decays of light and heavy flavoured jets, and in the case of electrons, from conversion processes. However, this kind of background is estimated in a different way than the other backgrounds, which is discussed in Section 6.3.2.

It is worth noting that in the following discussion of the different backgrounds the main concern is processes leading to final states with two leptons. By leptons we usually mean electrons or muons, since these are the ones targeted by the analysis. However, the simulated background samples also include corresponding processes with production of tau leptons, which subsequently decay to electrons or muons, although this might not be explicitly stated in the discussion or the Feynman graphs.

### 5.6.1 $Z + \text{jets}$

When we consider final states with two leptons with opposite charge the largest background is  $q\bar{q}$  annihilation to a  $Z$ -boson, which then leads to  $\ell^+\ell^-$ . This process is often accompanied by some jet activity. The leading order (LO) processes contributing to this kind of background are shown in Figure 5.1. A large fraction of these events produce pairs of leptons with invariant mass close to the  $Z$ -mass, but the mediator could also be off-shell ( $Z^*$  or  $\gamma^*$ ), leading to leptons with invariant mass very different from the  $Z$ -mass (or photon mass).

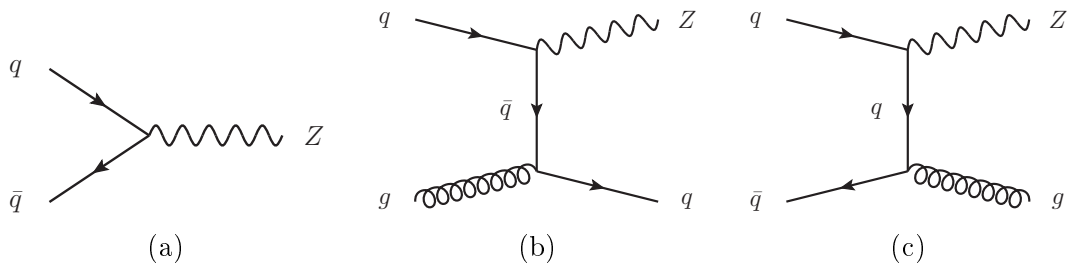


Figure 5.1: Leading order  $Z + \text{jets}$  production.

The  $Z + \text{jets}$  background events are generated with SHERPA v2.2.1 [65, 66]. SHERPA is an event generator that handles the whole process from calculation of matrix elements to parton showers and hadronization. Matrix elements for processes with hard parton emission are calculated with Comix [67], while virtual QCD corrections are calculated with OpenLoops [68]. The matrix elements are merged with SHERPA parton showers [69] according to the ME+PS@NLO prescription [70]. Notice that these specifications apply to all samples (not only  $Z + \text{jets}$ ) that are generated with SHERPA.

An event generator must also be suited with a set of Parton Distribution Functions (PDFs, discussed in Section 3.2.1) that describe the momentum distribution

amongst the different partons at given collision energy. The PDF set used for all samples generated with SHERPA v2.2.1 is called NNPDF3.0 NNLO [71].

The  $Z$ +jets background samples are produced separately for light-flavoured jets,  $c$ -jets and  $b$ -jets, because the filter efficiencies for each of these cases are different. At LO, processes with up to four partons are considered, while at next-to-leading order (NLO) processes with up to two partons are considered. Even though only LO and NLO events are simulated, they are normalized to account for next-to-next-to leading order (NNLO) contributions. This is done by multiplying the cross section for a sample with a so-called  $k$ -factor.

### 5.6.2 Di-bosons

Di-boson production is the case where a pair of weak gauge bosons ( $WW$ ,  $ZZ$  or  $WZ$ ) are produced. These processes are much rarer than the  $Z$ +jets processes, but they are very important in this analysis, as they can result in the same final state as the signal. The leading order di-boson processes are shown in Figure 5.2.

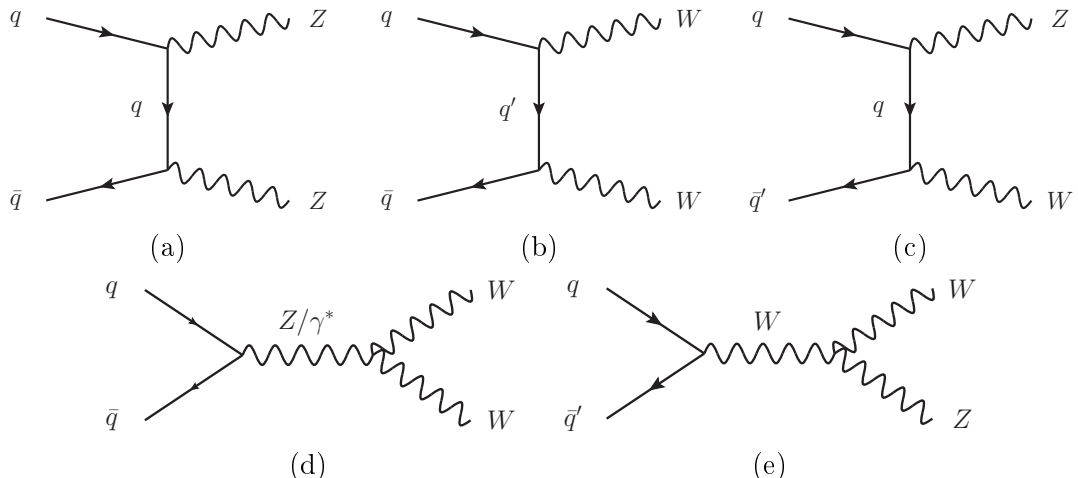


Figure 5.2: Leading order di-boson production.

Some examples on how the di-bosons could decay to give final states with two leptons are shown in Figure 5.3. Particularly the  $WW$  case (Fig. 5.3a) is important, as this could mimic the direct slepton signal process. If both  $W$ 's decay leptonically to the same lepton flavours we have exactly the same signal signature. The  $WZ$  case (Fig. 5.3c) with leptonic  $W$ -decay could also mimic the signal signature if one of the leptons from the  $Z$  fails to be reconstructed, and  $ZZ$  (Fig. 5.3b) could reproduce the signal if one of the  $Z$ 's decays to neutrinos.

Di-boson events with four electroweak vertices (like you get by combining Fig. 5.2 and Fig. 5.3) are generated with SHERPA v2.2.1 [65, 73]. Processes where both bosons decay leptonically are generated at NLO with up to one additional parton for  $4\ell$  and  $2\ell + 2\nu$  events, and no additional partons for  $3\ell + \nu$  events, and at LO with up to three additional partons. Processes where one of the bosons decay hadronically are generated with up to one additional parton at NLO, and up to three additional partons at LO.

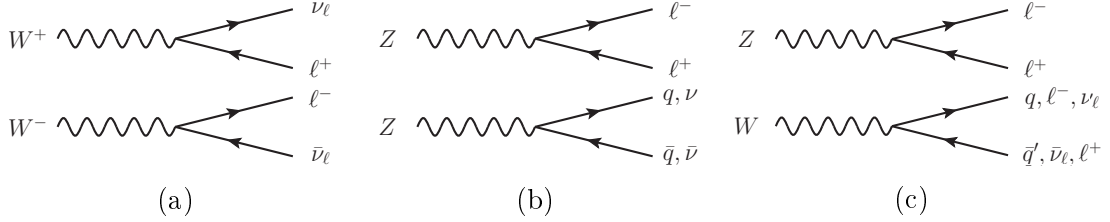


Figure 5.3: Some examples of di-bosons decaying to final states with two leptons.

Di-boson processes with six electroweak vertices are generated with SHERPA v2.1.1, using the CT10 PDF set [72]. Two examples of such processes are shown in Figure 5.4. In Figure 5.4a di-bosons are produced via a quark loop, while in Figure 5.4b di-bosons are produced along with two jets. These processes are generated at LO with up to one additional parton.

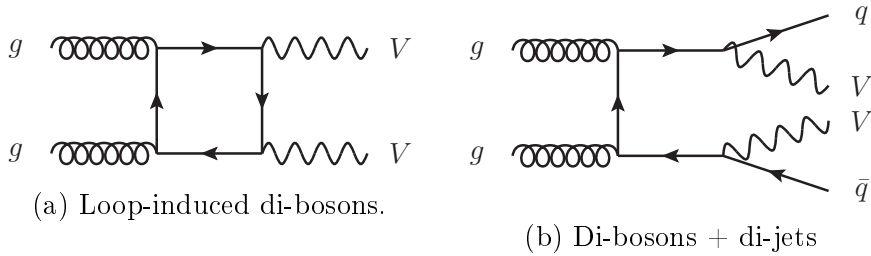


Figure 5.4: Examples of higher order production of di-bosons.

### 5.6.3 $V + \gamma$

$V + \gamma$  processes means production of a weak gauge boson ( $V$ ) along with a photon ( $\gamma$ ). At leading order this process is like  $WZ$ - or  $ZZ$ -production in Figure 5.2a and 5.2c, only replacing a  $Z$  by a  $\gamma$ . If  $V = Z$  we can get a final state with two leptons. Also if  $V = W$  and the  $W$  decays leptonically, and at the same time the photon is mis-identified as an electron (or any jet is mis-identified as a lepton), we would get something similar to the signal final state. The  $V + \gamma$  background is also simulated using the SHERPA v2.1.1 generator [65] with the CT10 PDF set [72].

### 5.6.4 Drell-Yan

Electroweak annihilation of a quark and an anti-quark leading to a lepton pair is called the Drell-Yan process, and is shown in Figure 5.5. The observant reader may notice that we have already considered this process in the section about  $Z$ +jets. However, the  $Z$ +jets samples are simulated with  $m_{\ell\ell} > 40$  GeV, while samples with  $10 < m_{\ell\ell} < 40$  GeV are simulated separately. These low- $m_{\ell\ell}$  samples are labelled "Drell-Yan", although they are not the only samples containing Drell-Yan processes. The invariant mass is kept above 10 GeV to avoid meson resonances like  $J/\psi$  ( $m_{J/\psi} \approx 3.1$  GeV) and  $\Upsilon$  ( $m_\Upsilon \approx 9.5$  GeV).

The low- $m_{\ell\ell}$  Drell-Yan samples are generated with the SHERPA v2.2.1 generator [65], following the same prescription as the other  $Z$ +jets samples.

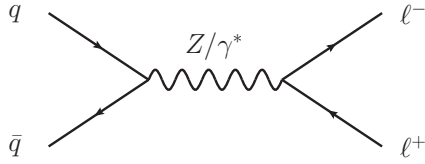


Figure 5.5: The Drell-Yan process.

### 5.6.5 $t\bar{t}$

One of the most important backgrounds we consider is  $t\bar{t}$  production. The leading order diagrams are given in Figure 5.6. The top quark nearly always decays to a  $W$ -boson and a quark, and in most cases that quark is a  $b$ -quark. So the most likely decay scenario is then  $t\bar{t} \rightarrow W^+W^-b\bar{b}$ . If both  $W$ 's decays to leptons we would end up with two leptons with opposite charge, two neutrinos and two  $b$ -jets (see Fig. 5.7). If the leptons have the same flavour, we would have something that looks a bit like the signal final state we are interested in, except from the  $b$ -jets. However, if we don't manage to tag the  $b$ -jets this process would contribute to the background in the signal regions.

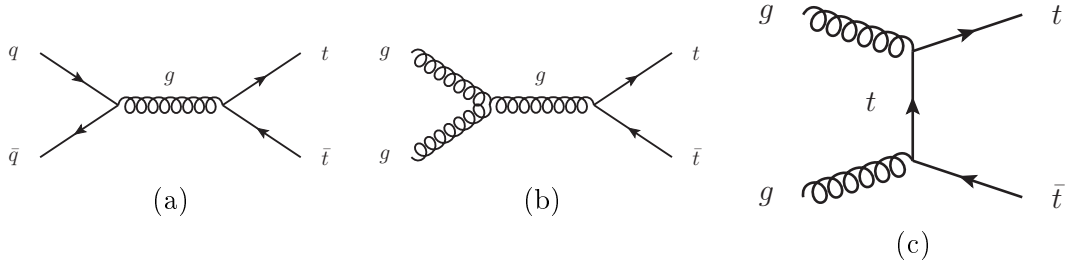


Figure 5.6: Leading order  $t\bar{t}$  production.

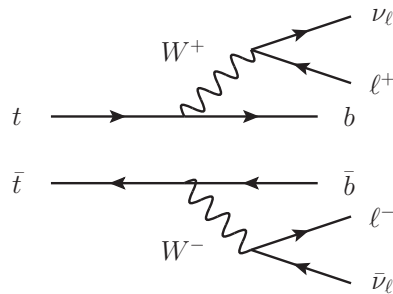


Figure 5.7:  $t\bar{t}$  decaying to  $W^+W^-b\bar{b}$ , followed by leptonic  $W$  decay.

The  $t\bar{t}$  background is simulated with POWHEG+PYTHIA6 [74]. Events are generated with the POWHEG-BOX [75] generator at NLO using the CT10 PDF set [72],

while the parton showers, hadronization and the underlying event are taken care of using PYTHIA6. The top quark mass is assumed to be  $m_t = 172.5$  GeV.

### 5.6.6 $W+\text{jets}$

The  $W+\text{jets}$  processes are the processes where a single  $W$ -boson is produced, possibly accompanied by jets. The leading order diagrams are shown in Figure 5.8. Since the  $W$  decays either to  $\ell\nu$  or quarks, no final states with two charged leptons are expected from these processes. However, if a jet is mis-identified as a lepton or in presence of electrons from conversions, these events could populate the signal region. The mis-identified jet (or conversion electron) would then be a so-called fake lepton, further discussed in Section 5.6.11.

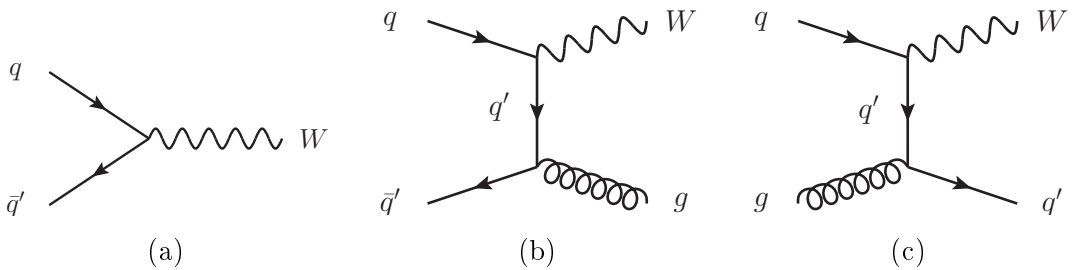


Figure 5.8: Leading order  $W+\text{jets}$  production.

The  $W+\text{jets}$  background is generated with SHERPA v2.2.1 [65, 66]. The simulation follows a similar prescription as the  $Z+\text{jets}$  generation, considering up to four jets at LO and up to two jets at NLO, and separate samples for light-flavour jets,  $c$ -jets and  $b$ -jets.

### 5.6.7 Single top

As the name suggests the single top processes are processes where a single top (or anti-top) quark is produced. The most interesting scenario for the purpose of this analysis is when the single top quark is accompanied by a  $W$ -boson, as pictured in Figure 5.9. This could lead to final states with two real leptons, which means that these processes are an important part of the background. The single top background is simulated by the same prescription as  $t\bar{t}$  with POWHEG+PYTHIA6 [74, 75].

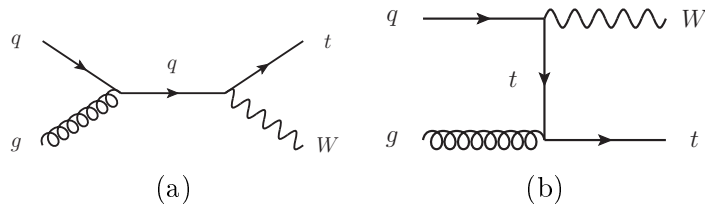


Figure 5.9: Production of a single top quark, together with a  $W$ -boson.

### 5.6.8 $t\bar{t} + V$

The  $t\bar{t} + V$  processes are processes where  $t\bar{t}$  is created together with a weak gauge boson. An example of such a process is given in Figure 5.10a. This process could of course lead to final states with two (real) charged leptons, but the cross sections for these processes are low. Taken into account that the final state most likely includes  $b$ -jets, this is not the kind of background we are most concerned with.

In this section we should also briefly mention the process where  $t\bar{t}$  is produced along with two  $W$ 's, as pictured in Figure 5.10b. Samples with such processes are included in the analysis, but in plots they are grouped together with  $t\bar{t} + V$  and labelled "ttV".

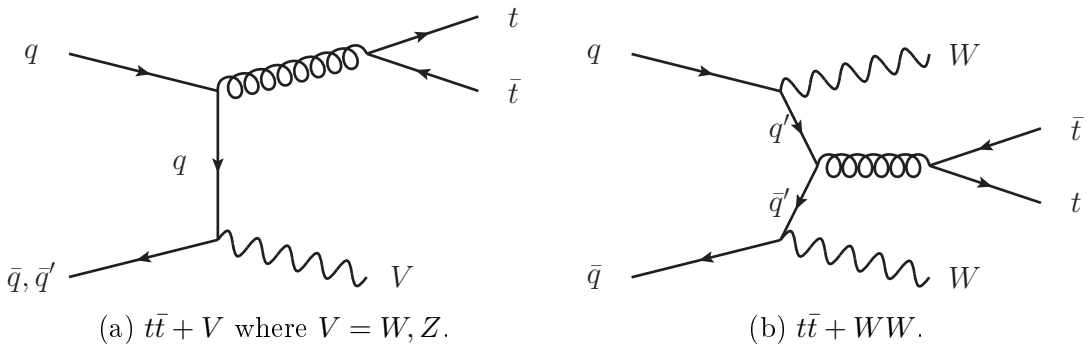


Figure 5.10:  $t\bar{t}$  produced together with one or two weak gauge bosons.

The  $t\bar{t}+V$  and  $t\bar{t}+WW$  processes are generated at LO using MADGRAPH v2.2.2 [78] for generating the matrix elements, and PYTHIA 8.186 [77] for parton showers and hadronisation. Up to one and two extra partons are included in the matrix elements for  $t\bar{t}+W$  and  $t\bar{t}+Z$  respectively, while no extra partons are included for the  $t\bar{t}+WW$  process. The samples are normalized to NLO. More details about the  $t\bar{t}+V$  processes can be found in ref. [76].

### 5.6.9 Higgs

As we know it took quite some time and effort to discover the Higgs boson, so processes involving the Higgs boson are obviously quite rare, hence do not make up a huge part of the background. However, they could lead to final states looking very much like the SUSY signal we are looking for, which is why it is important to include them in the background estimation. The various Higgs production channels are given in Figure 5.11. Note that the quarks involved in the diagrams in Figure 5.11a and 5.11d are likely to be top quarks.

If a Higgs boson is produced by gluon fusion via a quark loop (Fig. 5.11a) and decays through the decay mode shown in Figure 5.12, we would get exactly the same final state as the direct slepton production would give. The Higgs boson can also decay directly to two tau leptons which would also be included in the Higgs background samples. The samples are generated using POWHEG [79] with PYTHIA8 [77].

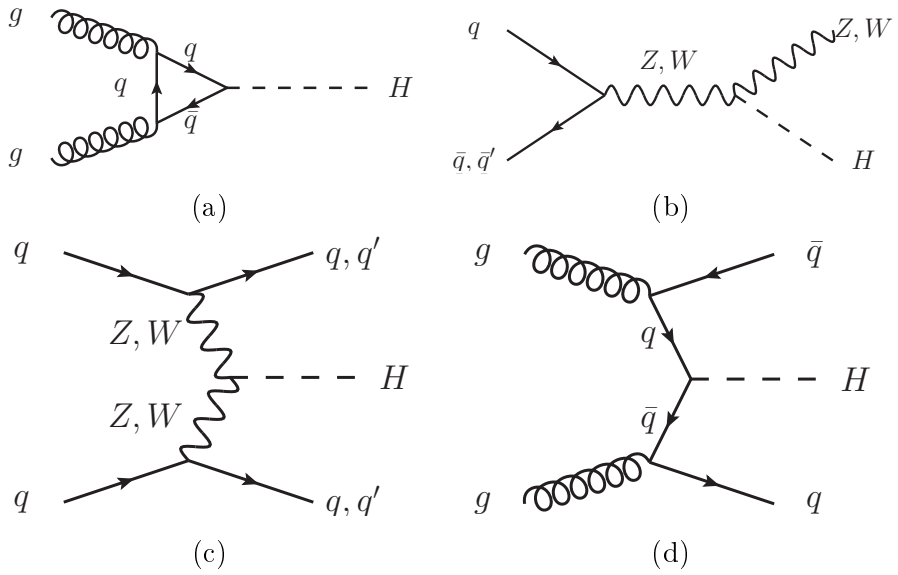


Figure 5.11: Higgs production channels.

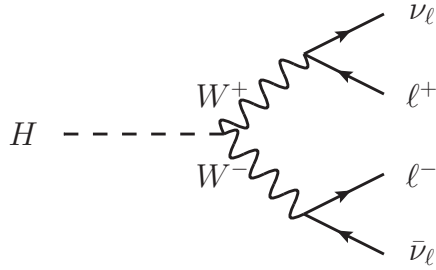


Figure 5.12: Higgs decaying to  $WW$ , and the  $W$ 's decaying to leptons.

### 5.6.10 Tri-bosons

The last Standard Model background to be considered is the very rare case where three weak gauge bosons are produced. Two examples are shown in Figure 5.13. The tri-boson samples are generated with SHERPA v2.2.1 [65, 73]. Matrix elements are calculated at LO for fully leptonic processes with up to two additional partons.

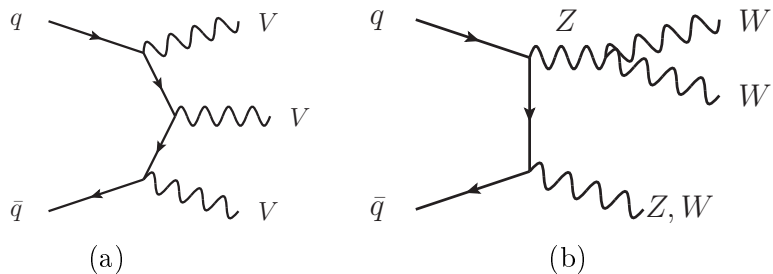


Figure 5.13: Examples of tri-boson production.

### 5.6.11 Fake leptons

The term *fake lepton* has been mentioned a couple of times during this chapter, and it is now time to explain what we mean by this. Up until now we have seen that the processes contributing to the background are processes where  $W$ 's,  $Z$ 's, top quarks or (in some rare cases) a Higgs boson decays leptonically. By fake leptons we simply mean reconstructed leptons that do *not* come from these kinds of processes, nor from the tau lepton.

Fake leptons can roughly be divided into two categories. The first category is the case where the reconstructed object actually is a lepton, but simply not of the kind we are interested in. These could for instance originate from weak decays of hadrons, like pions or kaons, or from  $c$ - or  $b$ -quarks. One of the purposes of the previously discussed isolation criteria is to deal with non-isolated leptons. However, some of these leptons occasionally pass the isolation requirements, and are taken into account in the analysis.

Another process creating "uninteresting" leptons are the so-called  $\gamma$ -conversions. This can occur if a charged lepton radiates a photon. If the photon is real it can only materialise as  $e^+e^-$  when it interacts with the detector material. This is called *external conversion*. If the radiated photon is virtual it could lead to  $e^+e^-$  or  $\mu^+\mu^-$  without any material interactions. This is called *internal conversion*.

The other category of fake leptons are objects that are wrongly identified as leptons. This could for instance occur if a jet deposits energy in the ECal, and this by coincidence is matched to a track in the ID. It could also happen if an energy deposit from a photon in the ECal accidentally matches a track in the ID.

Amongst the different background processes discussed in this chapter some are more likely to contribute to the fake background than others. The  $W+jets$  background would for instance only contribute if it contains a fake lepton, and likewise for the  $V + \gamma$  if  $V = W$ . The other main contributors to the fake backgrounds are the semi-leptonic  $t\bar{t}$  and single top processes, given that a real lepton is reconstructed along with a fake one. Other processes like di-bosons and  $Z+jets$  could also contribute to the fake background if a lepton fails to be reconstructed, but instead for instance a jet is reconstructed as a lepton.

### 5.6.12 Weighting and scaling

In order to account for differences between the simulated and real data the simulated samples needs to be weighted and scaled accordingly. Implementing this correctly is a very important part of the background estimation. In the following *event weights* and *scale factors* are discussed separately.

#### Event weights

Each simulated event is provided with a set of event weights, which are related to for instance physics objects or triggers. A brief explanation of the weights used in this analysis is given in this section.

The first to be mentioned are the electron and muon weights. These weights are meant to adjust for differences in efficiencies between data and MC when it comes

to particle identification, track reconstruction and track quality. The electron and muon weights are extracted using the SUSYTools methods `GetTotalElectronSF` and `GetTotalMuonSF` respectively, with the electron and muon containers as input. Correspondingly there is also a jet weight to account for differences in reconstruction and identification of jets. This is extracted with the `GetTotalJetSF` in SUSYTools with the jet container as input.

Next we have the trigger weights. The trigger efficiencies in the simulated samples might differ from the real trigger efficiencies, and these weight are meant to correct for this difference. Two trigger weights are used for each event; an electron trigger weight and a muon trigger weight. Like the electron and muons weights the trigger weights are also extracted with the `GetTotalElectronSF` and `GetTotalMuonSF` methods, only with the relevant di-electron and di-muon trigger as additional input arguments.

In addition to applying the above mentioned weights we also need to do something called *pile-up re-weighting*. As the MC usually is produced before the data is recorded it is hard to tell how the pile-up (i.e. average number of interaction per bunch crossing) in data will be. The MC is therefore generated with a pile-up that possibly differs from the data, and this needs to be accounted for by re-weighting each event with a pile-up weight.

At last we also need to add an event weight retrieved from the `EventInfo` class called `mcEventWeight`, which is associated with the simulation of the event. This weight is particularly important for `Sherpa` generated events, while for most other generators it is usually very close to one.

Once all the event weights are extracted they are multiplied and applied for each event when making histograms.

## Scale factors

When the MC background is simulated a certain number of events is generated. Each MC sample is related to a specific process, and is therefore accompanied by a given cross section. (See Appendix A.1.) The number of expected events is found by multiplying the integrated luminosity ( $\mathcal{L} = 36.1 \text{ fb}^{-1}$ ) by this cross section. Each MC sample therefore needs to be scaled, and the scale factor is calculated simply by taking the number of expected events ( $N_{\text{exp}}$ ) for a given cross section and luminosity, and divide it by the number of simulated events ( $N_{\text{sim}}$ ). So for a given sample the scale factor is found as

$$\text{sf} = \frac{N_{\text{exp}}}{N_{\text{sim}}} = \frac{\sigma \mathcal{L}}{N_{\text{sim}}}. \quad (5.10)$$

## 5.7 Baseline selection

When we are producing nTuples to use in the analysis there are certain requirements that needs to be fulfilled in order to include the event. This set of criteria is called the *baseline selection*. The purpose of the baseline selection is partly to ensure that the quality of the data set is good, and partly to reduce the data set to a size that

is more manageable (without throwing away potentially interesting events), and to limit ourselves to the final state processes we are interested in.

Some of the cuts in the baseline selection apply only to real data, and they are typically related to the state of the ATLAS detector and the LHC at the time of the data taking. These cuts follow the recommendations from the ATLAS Data Preparation group [81] for analysis of Run 2 data, and are summarised in the following three bullet points:

- **Good runs list (GRL):** All events must be part of a luminosity block that appears in the GRL.
- **LAr/Tile error:** Events with noise burst and data integrity errors in the LAr calorimeter are rejected.
- **Tile trip:** Events with Tile trips must be removed.

The rest of the baseline selection is applied to both data and Monte Carlo, and these cuts are in general more motivated by physical properties of the event, i.e. that the particles in the event actually come from a hard proton-proton scattering. These cuts follows the prescriptions in ref. [82], except from the last cut, which is a more "analysis specific" cut.

- **Bad muons:** Skip events containing muons that do not originate from a proton-proton collision. Muons are decorated as "bad" in SUSYTools if  $\sigma(q/p)/|q/p| > 0.2$ . These objects could, for instance, come from background activity in the cavern.
- **Cosmic muons:** Another type of muons not originating from the proton-proton collision is *cosmic* muons. Events containing such muons are rejected. Muons are decorated as "cosmic" in SUSYTools if  $|z_0^{\text{PV}}| < 1 \text{ mm}$  and  $|d_0^{\text{PV}}| < 0.2 \text{ mm}$ .
- **Bad jets:** Processes that do not come from a  $pp$  collision can also lead to energy deposits in the hadronic calorimeter, which are then reconstructed as jets. Jets are decorated as "bad" in SUSYTools if they are LooseBad<sup>4</sup> and have  $p_T > 20 \text{ GeV}$ , and events containing such jets are rejected.
- **Primary Vertex:** Each event must contain a primary vertex. The primary vertex must have at least two associated tracks with  $p_T > 400 \text{ MeV}$ . If there are several such vertices in an event the one with largest sum of squared momenta ( $\sum p_T^2$ ) of the outgoing particles is chosen. The primary vertex is identified by the GetPrimVtx method in SUSYTools.
- **Baseline leptons:** In this analysis it is chosen to only keep events with at least two baseline leptons (as defined in Tables 5.2 and 5.3). In the end we will anyway require two signal leptons, which is a stricter requirement, hence we don't loose any interesting events by doing this cut, and the data set is reduced to a more manageable size.

---

<sup>4</sup>The LooseBad jet selection is the selection recommended by the Jet/Etmiss working group in ref. [83]. The details on how the selection is defined can be found in ref. [84].

## 5.8 Pre-selection

When we have done the baseline selection and downloaded the nTuples we start to further narrow down the data set. First we will define a so-called *pre-selection* of events, which is a basic selection of events done before the real analysis begins. The pre-selection is based partly on physical properties of the final state we are looking at, and partly on detector specifics, such as the triggers.

For instance we have already mentioned that the final state must contain two leptons of same flavour (SF) and opposite sign (OS) charge, so we want to require events to contain two SF OS signal leptons. The lepton with the highest transverse momentum is called the *leading lepton*, while the one with lowest transverse momentum is called the *sub-leading lepton*. We require the leading lepton to have  $p_T > 25$  GeV and the sub-leading lepton to have  $p_T > 20$  GeV. This is to make sure we are on the *trigger efficiency plateau*, i.e. in the  $p_T$ -area where the triggers are close to 100% efficient.

Then we also want to check if the individual event has passed certain triggers. This is done with a "OR"-statement in the code, meaning that we accept the event if it passed *one* of the triggers. The specific triggers used are listed in Table 5.6. Note that when we require SF leptons only the SF triggers are checked.

The last part of the pre-selection makes use of two different invariant mass cuts. The first accepts events containing two leptons with invariant mass above 40 GeV. This is mainly to get rid of hadronic activity in the low- $m_{\ell\ell}$  region. The second is a  $Z$ -veto. A large amount of events include production of a  $Z$ -boson, which then decays to two leptons. These are clearly events we are not interested in, and a way to get rid of a lot of these is to throw away events with  $m_{\ell\ell}$  in the  $Z$ -peak area, e.g. within 20 GeV of the  $Z$ -mass.

Notice that all cuts in the pre-selection are *always* applied, unless they are in conflict with the definition of the particular region we are looking at. Such conflicts occurs only in certain control and validation regions, where we require different flavour (DF) leptons, which is the reason why also the DF triggers are listed in Table 5.6.

Pre-selection
Exactly 2 SF OS signal leptons
$p_T^{lep1} > 25$ GeV & $p_T^{lep2} > 20$ GeV
Lowest unprescaled di-electron and di-muon triggers
$m_{\ell\ell} > 40$ GeV
$Z$ – veto: $ m_Z - m_{\ell\ell}  > 20$ GeV

Table 5.5: Summary of the pre-selection.

The plots in Figure 5.14 show some distributions after the pre-selection cuts are applied, with exception of the  $Z$ -veto. As expected we can see that the  $m_{\ell\ell}$ -distribution (Fig. 5.14b) has a very prominent peak around the  $Z$ -mass. The  $Z$ -veto removes this, and therefore a great amount of events. As we can see, this affects the

	2015	2016
Di-electron channel		
	HLT 2e12 lhloose L12EM10VH	HLT 2e15 lhvloose nod0 L12EM13VH (HLT 2e17 lhvloose nod0)
Di-muon channel		
	HLT mu18 mu8noL1	HLT mu20 mu8noL1 (HLT mu22 mu8noL1)
Electron-muon channel		
	HLT e17 lhloose mu14	HLT e17 lhloose nod0 mu14

Table 5.6: Trigger selection. The 2016 triggers in parenthesis are high luminosity trigger, which were used in a number of runs in the late part of the 2016 data taking.

$Z+jets$  background the most, which is reduced from  $\sim 39$  million events to  $\sim 2.3$  million events. Even though the  $Z+jets$  is still the dominating background after the  $Z$ -veto, it is nice to see whether or not the modelling is fine before we remove that many events.

Figure 5.15 shows the same variables as Figure 5.14, but now with the full pre-selection applied. We see that the  $Z$ -peak is greatly reduced (Fig. 5.15b), as it should be, and the  $Z+jets$  background in general is lower in the other distributions. However,  $Z+jets$  is still the dominating background, together with various top backgrounds and  $V + \gamma$ . The di-bosons, which we expect to be the most difficult background to deal with, can be seen towards the end of the distributions, but they are not very prominent at this stage.

All distributions, both the ones presented in this section and in the next chapter, contains a shaded area. This area represents the *statistical uncertainties* of the estimated background, which for each bin is calculated as the sum of event weights, which were introduced in Section 5.6.12. Notice that some of these areas are quite large, even when the statistics is relatively high. This is caused by events with large `mcEventWeight` in some of the `Sherpa` samples.

The general impression from Figures 5.14 and 5.15 is that the SM MC background describes the data rather well.

## 5.9 Comparison of Sherpa versions

During the work with this analysis there was a switch from using MC samples generated with `Sherpa` v2.1.1 to using samples generated with `Sherpa` v2.2.1. This regards the  $Z+jets$ ,  $W+jets$ , Drell-Yan, tri-bosons and some of the di-boson samples. Some of the updates in `Sherpa` v2.2.1 are given in ref. [87], and include for example a new set of PDFs (changed from CT10 [72] to NNPDF3.0 [71]), and a new module for parton shower simulations [88].

A comparison between the new and the old samples was done in order to see

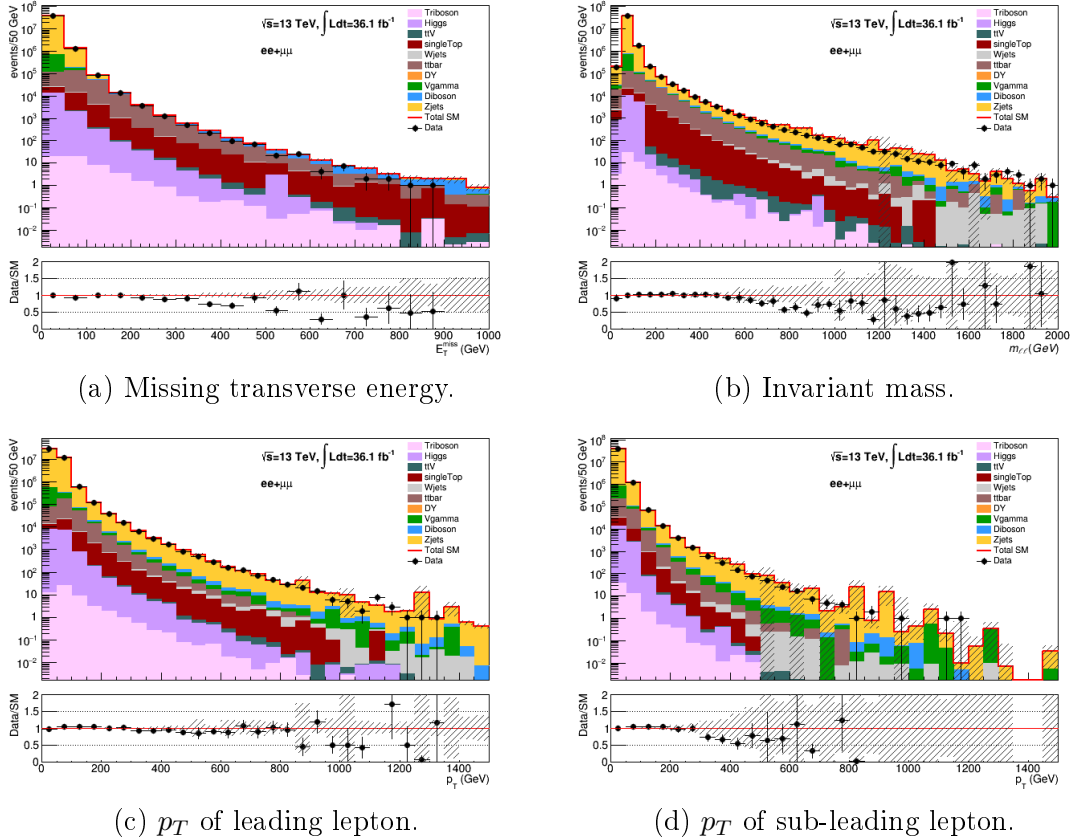
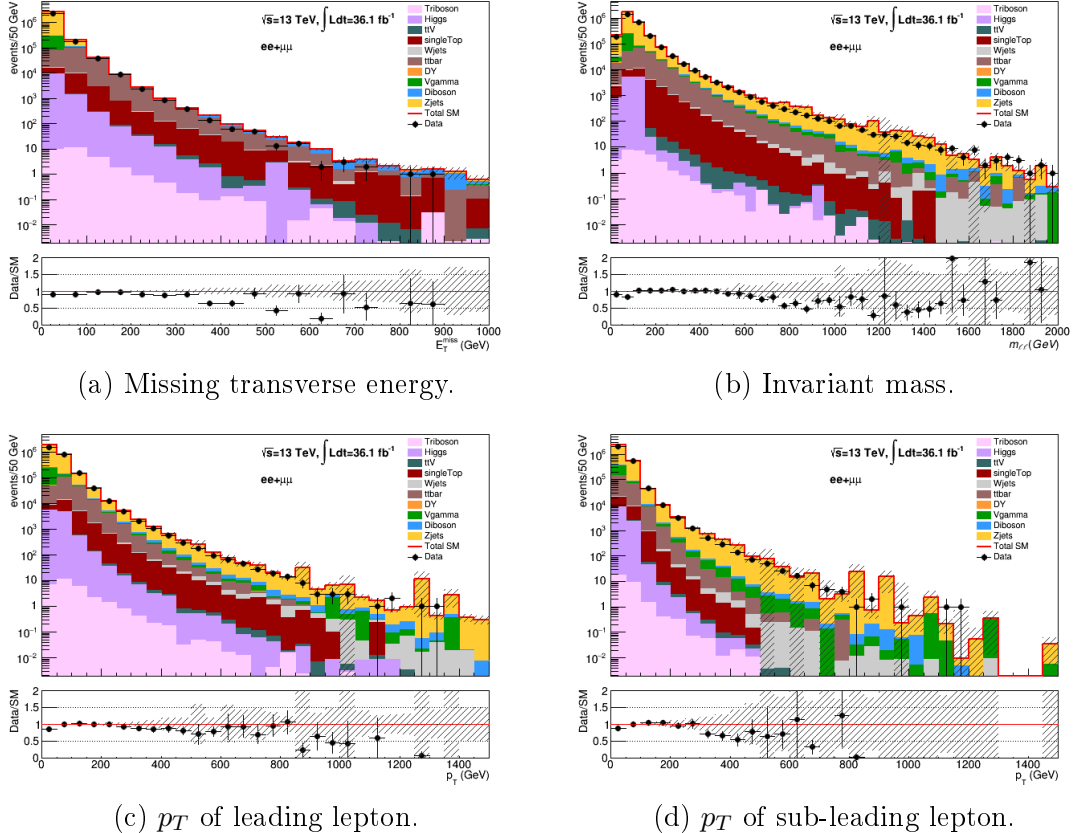


Figure 5.14: Distributions for some of the most important variables before the  $Z$ -veto is applied.

how they differed. These comparisons were done only for the  $Z$ +jets and di-bosons, and the results of these studies are given in Figures 5.16 and 5.17 respectively. Note the histograms in these figures are normalised to unity, and that the pre-selection cuts in Table 5.5, with exception of the  $Z$ -veto, are applied in these plots. The variables considered in the distributions are  $p_T$  of the leading lepton and  $E_T^{miss}$ .

The tendency for both di-bosons and  $Z$ +jets seems to be that the agreement is good in the beginning of the distributions (i.e. up to  $\sim 100$  GeV), while after that the new samples seems to be overshooting the old ones. The question is whether or not the differences improve the modelling of the data.

The  $M_{T2}$  distributions when using the two different SHERPA version for  $Z$ +jets and di-bosons are shown in Figure 5.18. We see that there is a definite improvement in the modelling when using SHERPA v2.2.1, at least for the  $Z$ +jets, which is the dominating background in these distributions. Notice that  $M_{T2}$  is presented here because the improvement was most visible in this variable. Some other variables also showed improvement, but less obvious than  $M_{T2}$ , while some variables looked about the same with the two versions of SHERPA.



(c)  $p_T$  of leading lepton.

(d)  $p_T$  of sub-leading lepton.

Figure 5.15: Distributions after the full pre-selection is applied.

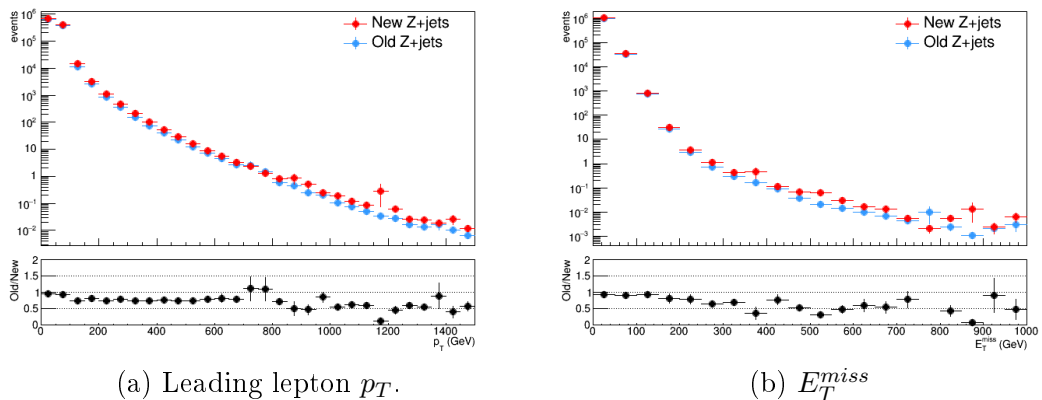


Figure 5.16: Comparison plots for the  $Z+jets$  background. "Old" means Sherpa 2.1.1, and "New" means Sherpa 2.2.1.

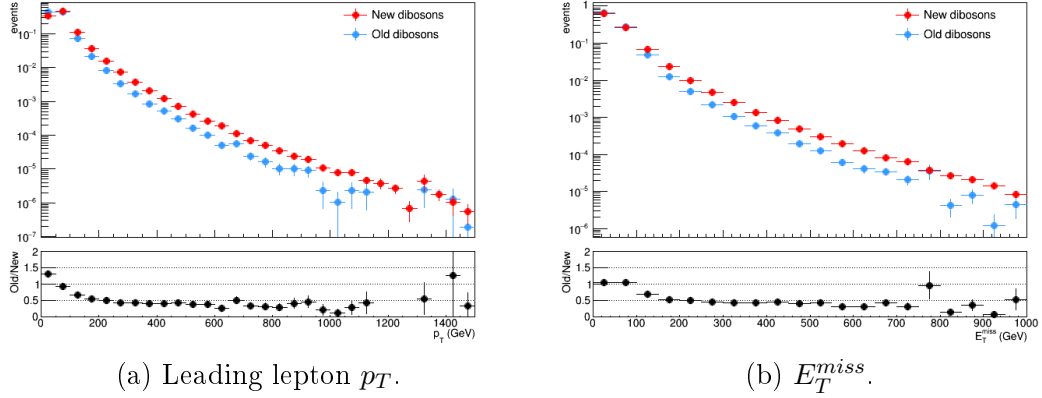


Figure 5.17: Comparison plots for the Di-boson background. "Old" means Sherpa 2.1.1, and "New" means Sherpa 2.2.1.

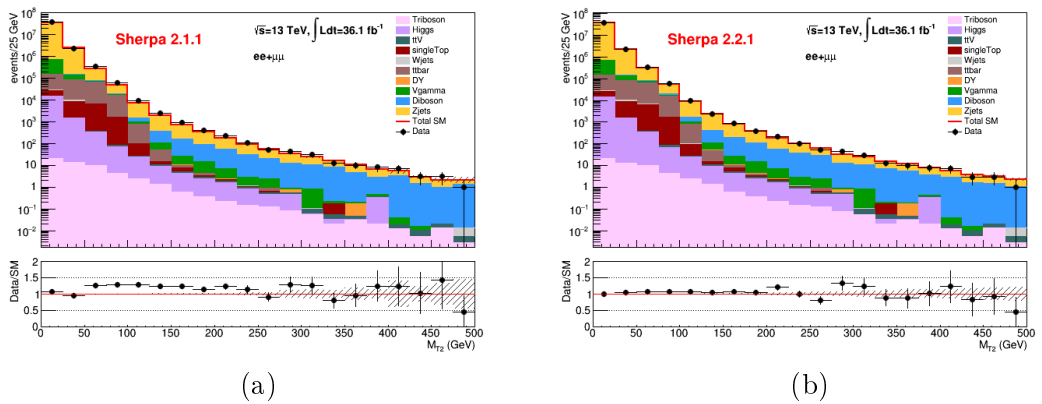


Figure 5.18:  $M_{T2}$  distributions for a) old and b) new SHERPA samples for the  $Z + \text{jets}$  and di-boson background.

# Chapter 6

## Results of the Search for Direct Production of Sleptons

In the previous chapter we arrived to a pre-selected set of di-lepton events that define the starting point for the further analysis, and we saw that the data are rather well reproduced by the simulated SM background. This chapter gives the details on how the search for direct production of sleptons is done. We define a set of signal regions, which should make us sensitive to direct slepton signals, work out the expected sensitivities, and look at some possibilities for optimisation of these signal regions. The most exciting bit of the analysis is of course to compare data and SM predictions in the signal regions to see whether or not they agree. This will be done at the end of the chapter, but first we need to make sure that the background is well estimated. This is done by using so-called control and validation regions. Before proceeding with final cuts and discussing the direct slepton signal regions, let us first start by introducing some statistical tools that will help us optimizing the signal regions and interpret the final results.

### 6.1 How to interpret results

When interpreting the results of the analysis it is important to keep in mind that what we do is simply a counting experiment. The essence of the whole analysis is to count number of data events and compare it to the expected number of events, which is estimated by Standard Model MC (and/or data driven) backgrounds.

A certain process takes place with a probability given by the cross section for that particular process. The expected number of times this processes would show up in the data is given by the cross section times the integrated luminosity. However, as we are talking about probabilities, we must be aware that this number can deviate from the expectations, and that such deviations do not necessarily mean that the background model is wrong. For this reason it is always desirable to have as much statistics as possible, since more data means that large deviations from the expectations are less probable, assuming that the background model is correct. On top of these statistical fluctuations there are of course also other possible sources of mismatch between data and MC. This includes measurement uncertainties, inaccuracy in cross section estimations and not to mention bugs in the code, either

the one written by the individual analysers or the one written centrally e.g. for production or derivation of MC samples.

When we arrive to the final comparisons between data and MC we can imagine two possible scenarios. The first one (and most exciting!) is that there is an excess of data events compared to the expected number of events. In such a situation one must be able to judge if this is likely to come from a fluctuation, or if it is something that most probably can't be explained by the Standard Model. The second scenario is of course that the data is well explained by the SM background. In this case we would like to know whether or not we can actually rule out the possibility of a specific beyond SM scenario, i.e. one or several SUSY signal models. Since we are dealing with probabilities we need to involve tools from probability theory and statistics. The ways of tackling these two scenarios are discussed in the following two sections, which are heavily based on section 8.1 of ref. [25].

### 6.1.1 Significance

When searching for new physics we do a certain selection of events, which is designed to ensure that we are sensitive to new physics. Such a selection is called a *signal region*. A single event will then with a certain probability either pass or fail the event selection requirements, and therefore the number of observed events in a signal region follows the binomial distribution

$$P(n|N, p) = \frac{N!}{n!(N-n)!} p^n (1-p)^{N-n}, \quad (6.1)$$

which is the probability of getting  $n$  events in the signal region, given that we have  $N$  events in total, and each event has a true probability  $p$  of passing the event selection. In the limit where  $N \rightarrow \infty$ ,  $p \rightarrow 0$  and  $Np \rightarrow \nu$ , where  $\nu$  is a constant, the binomial distribution can be approximated by the Poisson distribution. This is indeed the case for us, since we have a huge amount of events, but only a few of them get into the final selection of events. The Poisson distribution is given as

$$P(n|\nu) = \frac{\nu^n}{n!} e^{-\nu}, \quad (6.2)$$

which is the probability of observing  $n$  events when we expect to observe  $\nu$  events, where  $\nu$  is given by the hypothesis we are testing the observations against. Examples of relevant hypotheses are the *background-only* hypothesis, which is that the Standard Model is able to describe our data, and the *signal+background* hypothesis, which is that we also need some additional physics to describe the observed data.

Now assume that the number of events,  $q_{obs}$ , we observe in our signal region is higher than the number of events,  $b$ , predicted by the Standard Model. We would then like to know the probability of observing at least  $q_{obs}$  events, given that the background-only hypothesis is true. This probability is called the *p-value*, and is given as

$$p = P(n \geq q_{obs} | b) = \sum_{n=q_{obs}}^{\infty} \frac{b^n}{n!} e^{-b}. \quad (6.3)$$

The  $p$ -value is often translated to a significance,  $z$ , defined as

$$z = \Phi^{-1}(1 - p), \quad (6.4)$$

where  $\Phi$  is the standard Gaussian distribution. In high energy physics it is common practice to express  $z$  as number of standard deviations ( $\sigma$ ) from the centre of the Gaussian distribution, and the general rule is that the significance must be at least  $5\sigma$  in order to reject the background-only hypothesis, which corresponds to  $p = 2.87 \cdot 10^{-7}$ .

### 6.1.2 Exclusion

No SUSY searches done so far have shown any significant excesses. When this is the case we would like to know whether or not we actually can rule out certain signal models. This is also done using a  $p$ -value, which in this case is called  $CL_{s+b}$ . This is the probability of observing a maximum of  $q_{obs}$  events if the signal+background hypothesis actually is true, and is given by

$$CL_{s+b} = P(n \leq q_{obs} | s + b) = \sum_{n=0}^{q_{obs}} \frac{(s + b)^n}{n!} e^{-(s+b)}. \quad (6.5)$$

A common practice is to exclude the signal+background hypothesis if  $CL_{s+b} \leq 5\%$ , which means that there is 5% chance of wrongly excluding a signal model.

When optimising a search we use the significance,  $Z_N$ , defined as

$$Z_N = \Phi^{-1}(1 - CL_{s+b}) \quad (6.6)$$

as optimisation parameter, and  $CL_{s+b} = 5\%$  corresponds to  $Z_N = 1.64$ . All significance values and sensitivities presented in this thesis are calculated using the `RooStats::NumberCountingUtils::BinomialExpZ` function in ROOT, with number of signal and background events as input, together with the uncertainty of the background estimate, in this analysis assumed to be a 30% flat systematic uncertainty. Notice that in the following sections this assumption is *only* applied in sensitivity calculations, while the uncertainties indicated in distributions of kinematic variables and in tables are purely statistical, as discussed in Section 5.8.

## 6.2 Final selection and definition of signal regions

After the pre-selection we are left with a basic selection of events that can be regarded as "interesting" to the analysis. But, of course, the Standard Model background is still huge, so we need to apply some additional cuts that would make us sensitive to SUSY signals. A set of such cuts is called a *signal region* (SR).

In this analysis two different approaches are used. We have two so-called *inclusive* SRs, and 13 orthogonal *exclusive* SRs. The inclusive SRs targets a wide range of signal points, while the exclusive SRs are more focused on specific areas of the signal grid. Also, since the exclusive SRs are orthogonal, the sensitivity in these regions can be added up to give a combined sensitivity for all 13 SRs. This

is not the case for the inclusive ones. Throughout the rest of this section both the inclusive and exclusive SRs will be defined and discussed in detail. We will start with a short discussion of the cuts that are common to all the SRs, namely the jet vetoes.

## Jet vetoes

With exception of the possibility of initial state radiation (ISR) the final state is not expected to contain jets, which is why we want to introduce some jet vetoes. Because of ISR there is a possibility that we loose some interesting events through the jet vetoes, but it is very difficult to deal with some of the backgrounds (like  $Z+jets$  and  $t\bar{t}$ ) without introducing such vetoes. Two different jet vetoes are applied:

- Central b-jet veto with  $p_T > 20$  GeV.
- Central light jet (CLJ) veto with  $p_T > 60$  GeV.

To make it clear, this means that if an event contains at least one central b-jet with  $p_T > 20$  GeV or at least one CLJ with  $p_T > 60$  GeV we reject the event, where "central" means  $|\eta| < 2.4$ . The jets are required to be signal jets (see Tab. 5.4). We do *not* cut on forward jets (i.e.  $|\eta| > 2.4$ ), since this region is expected to contain ISR jets.

The main purpose of the b-jet veto is to get rid of the  $t\bar{t}$  background. As discussed in Section 5.6.5  $t\bar{t}$  is an important part of the background, and at this point we make use of the b-tagging discussed in Section 5.2.3. The CLJ veto is introduced to deal with background processes containing lighter jets, meaning jets that originate from  $u$ -,  $d$ -,  $s$ - and (to less extent)  $c$ -quarks.

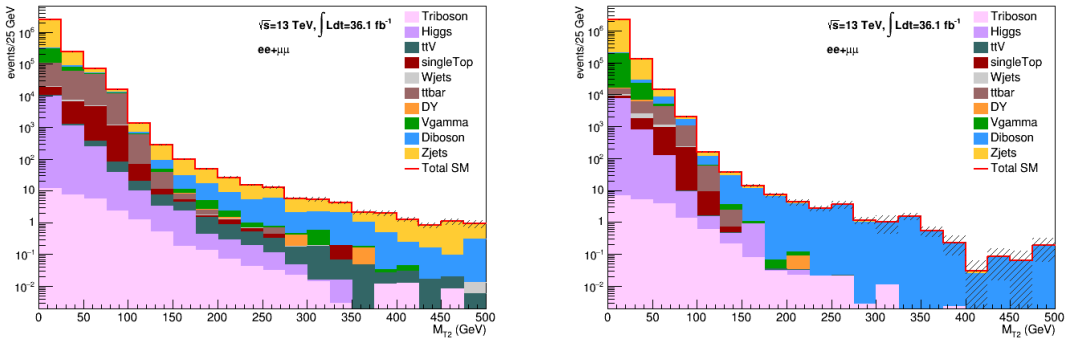
Figure 6.1 shows the MC background distribution for the  $M_{T2}$  variable before and after the jet vetoes are applied, and we can clearly see the effects of these cuts. First, we see that the top background (both  $t\bar{t}$ , single top and  $t\bar{t}V$ ) is strongly reduced, which is exactly what we expected by applying the b-veto. The remaining top background is likely to be due to the limited b-tagging efficiency. Second, we see that the  $Z+jets$  background (together with  $V+\gamma$  and DY) in the region  $M_{T2} \gtrsim 100$  GeV have almost vanished. However, the  $Z+jets$  background in the lowest bins is not affected by these cuts.

### 6.2.1 Inclusive SRs

The definitions of the inclusive SRs are given in Table 6.1. They are called *SR-loose* and *SR-tight*, and are defined by cuts in  $m_{\ell\ell}$  and  $M_{T2}$ . As the names suggest SR-tight involves tighter cuts in these variables than SR-loose.

#### SR-loose

SR-loose is designed to target the part of the signal grid with lower slepton masses, i.e. up to about 300 GeV. After the jet vetoes the main backgrounds are  $Z+jets$ ,  $V+\gamma$  and di-bosons, together with the "left-over" top background. The first cut in this SR is  $m_{\ell\ell} > 111$  GeV (or  $m_{\ell\ell} - m_Z > 20$  GeV). Remember that we have already



(a) Background before jet vetoes.

(b) Background after jet vetoes.

Figure 6.1

Inclusive signal regions		
	SR-loose	SR-tight
$m_{\ell\ell}$ (GeV)	> 111	> 300
$M_{T2}$ (GeV)	> 100	> 130

Table 6.1: Inclusive signal region definitions.

removed all events with  $m_{\ell\ell}$  between 71 GeV and 111 GeV with the  $Z$ -veto, meaning that this cut really only affects events with  $m_{\ell\ell} < 71$  GeV. The  $m_{\ell\ell}$  distribution before the cut is applied is shown in Figure 6.2, and we see that the dominating background at  $m_{\ell\ell} < 111$  GeV is  $Z + \text{jets}$  and  $V + \gamma$ .

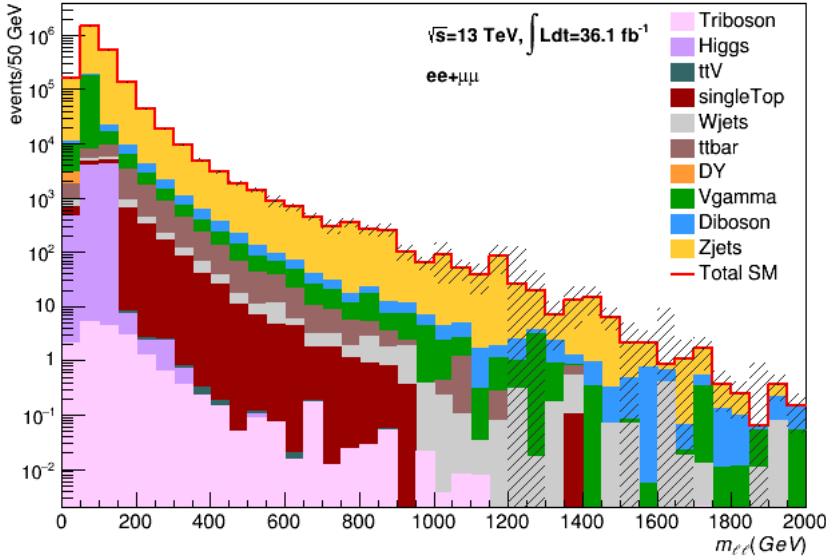


Figure 6.2: Background before  $m_{\ell\ell}$  cut in SR-loose.

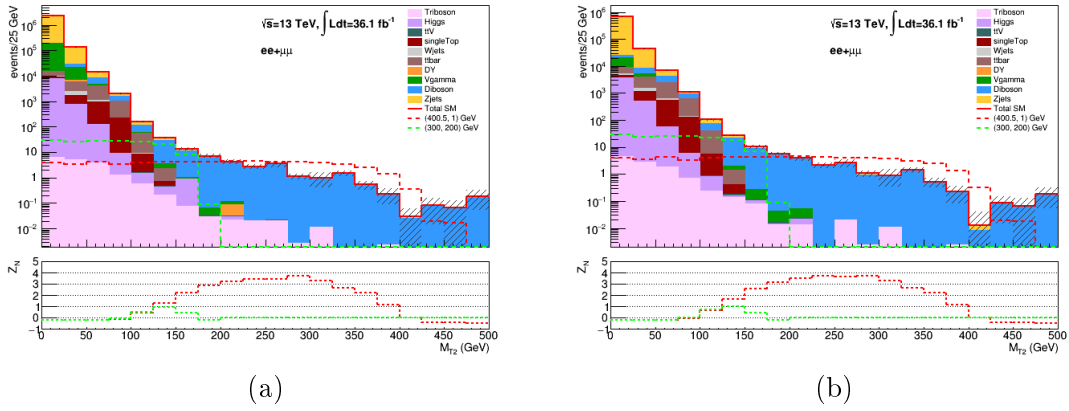


Figure 6.3: The plots shows the  $M_{T2}$  distribution a) before and b) after the  $m_{\ell\ell} > 111$  GeV cut is applied, with the expected sensitivity to the signal benchmark points.

Figure 6.3 shows the  $M_{T2}$  distribution before and after the  $m_{\ell\ell}$  cut. We see that this cut affects mainly the  $Z + \text{jets}$  and  $V + \gamma$  backgrounds in the low  $M_{T2}$  region. However, this region is still dominated by these backgrounds together with the different top backgrounds. The high  $M_{T2}$  region is dominated by di-bosons. In this figure we have also introduced two so-called *benchmark points* for the signal samples introduced in Section 5.5. These are added to get an impression of whether or not we are sensitive to SUSY signals, and they are chosen to be points that have not been excluded in previous searches (see Fig. 2.5). They are also chosen from different parts of the signal grid, so we have one point with intermediate mass splitting ( $m_{\tilde{\ell}} = 300$  GeV,  $m_{\tilde{\chi}_1^0} = 200$  GeV), and one point with high mass splitting ( $m_{\tilde{\ell}} = 400.5$  GeV,  $m_{\tilde{\chi}_1^0} = 1$  GeV).

The lower plots of Figure 6.3 indicate the expected sensitivity,  $Z_N$ , to the benchmark points, and is calculated as described in Section 6.1.2. The sensitivity to a signal point indicates at which significance level we can exclude this point given that the data is well explained by the MC background. The value of  $Z_N$  in a particular bin is obtained by cutting away everything at the left side of that bin.

By fixing the cut at  $M_{T2} > 100$  GeV we gain some sensitivity to both the intermediate and the high mass splitting points, and we remove a lot of  $Z + \text{jets}$  and top background. It is noteworthy that we could have gained a lot higher sensitivity to the high mass splitting point through a harder  $M_{T2}$  cut, but (as stated earlier) SR-loose is designed to target the point with lower slepton masses, which is the first concern.

The sensitivity to the full direct slepton signal grid in this SR is given in Figure 6.4. In these sensitivity plots the slepton mass is given on the  $x$ -axis, while the neutralino mass is given on the  $y$ -axis, and each square represents a signal point from Table A.11. The number in the square gives the sensitivity ( $Z_N$ ) to this signal point, and if a signal point is not included in the plot it means that we have no sensitivity to the point in this SR. The colours are meant to give an impression of which area(s) of the grid we are more or less sensitive to, and we can see that SR-loose is most sensitive to the area with lower slepton masses.

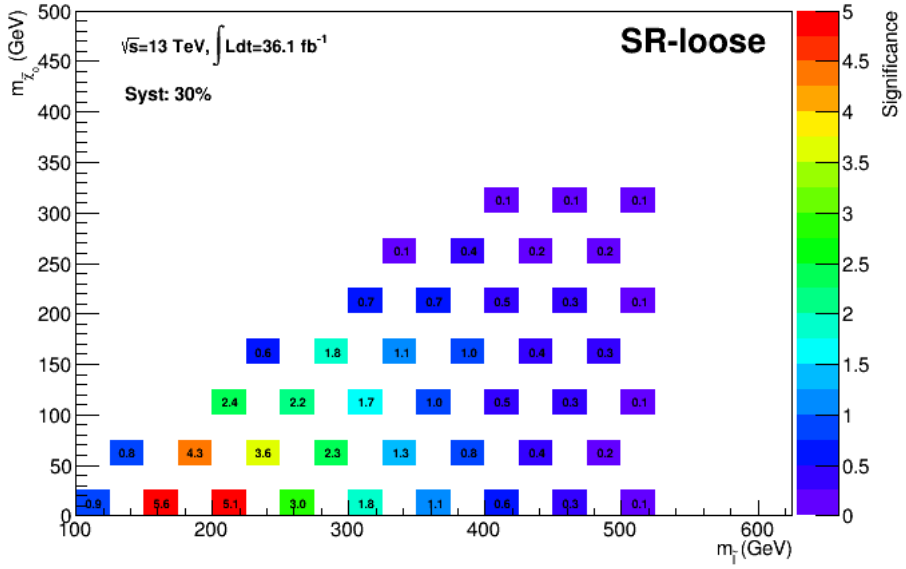


Figure 6.4: Sensitivity to the direct- $\tilde{l}$  signal grid with SR-loose.

### SR-tight

The second inclusive signal region is called SR-tight. This is designed to target the higher slepton masses. In SR-loose we still have a lot of background events left, which suggests that we can allow ourselves to cut harder in  $m_{\ell\ell}$  and/or  $M_{T2}$ . The  $m_{\ell\ell}$  cut is increased to 300 GeV, which leaves us with the  $M_{T2}$  distribution in Figure 6.5. We see that good sensitivity to the high mass splitting benchmark point can be obtained by cutting at  $M_{T2}$  at for example 130 GeV. After this cut we expect a sensitivity to the full signal grid as given in Figure 6.6, which shows that we expect good sensitivity (i.e.  $Z_N > 1.64$ ) to a very large part of the signal grid, and we have good sensitivity to a lot of points with high slepton masses that have not been excluded previously (see Fig. 2.5). The fact that we have relatively good sensitivity to the points with high slepton masses also suggests that the signal grid should be extended. In fact new signal samples with slepton masses up to  $\sim 700$  GeV have been generated, but unfortunately cross sections and filter efficiencies are (at the moment of writing) not available, so they could not be included in the analysis.

### Expected background (inclusive SRs)

To finish the presentation of the inclusive SRs the expected signal and background yields are given in Table 6.2. The first row of the table shows the total number of expected background events, while the following rows show how the background is composed, and the last two rows show the yields for the two signal benchmark points. As expected we see that the di-bosons make up the largest part of the background, followed by top and  $Z+jets$  in SR-loose, while the background in SR-tight is almost pure di-bosons. Notice that this table does not include the fake

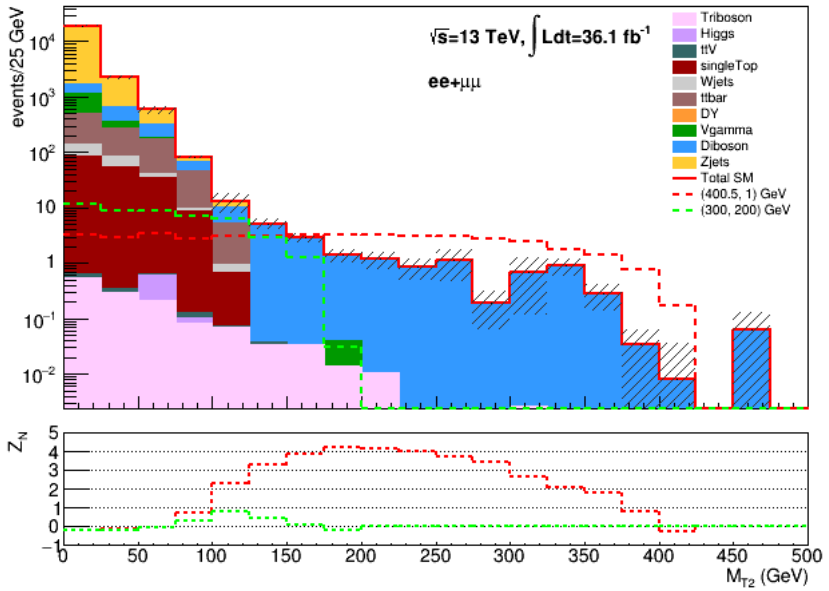


Figure 6.5:  $M_{T2}$  distribution in SR-tight before the cut on this variable.

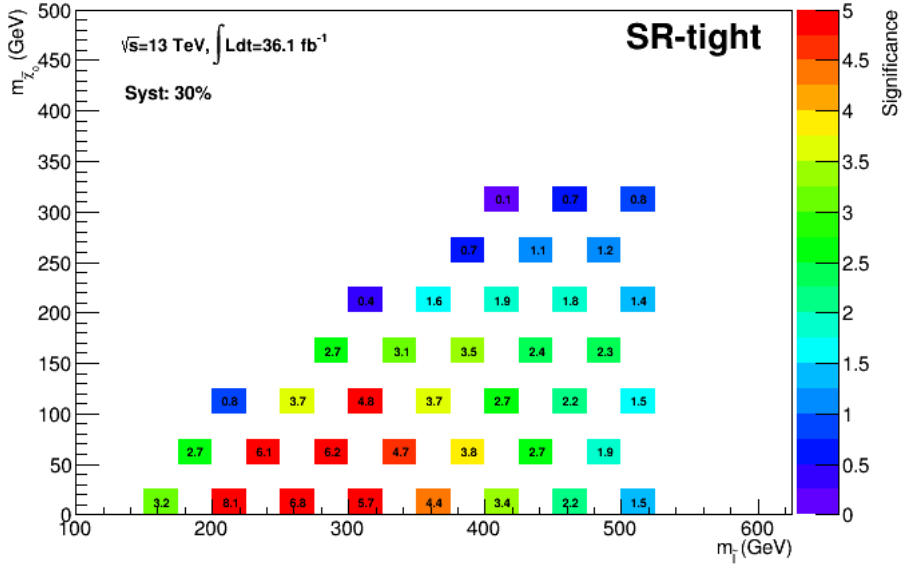


Figure 6.6: Expected sensitivity to the direct slepton signal grid in SR-tight.

lepton background, which will be discussed in more detail in the section 6.3.2.

### 6.2.2 Optimisation of inclusive SRs

The signal regions described above were defined and agreed on collectively in the SUSY 2/3 lepton working group. Some work has however been done during the

	SR-loose	SR-tight
Expected background	$154.04 \pm 8.85$	$12.86 \pm 1.63$
$Z + \text{jets}$	$31.76 \pm 4.89$	$0.36 \pm 0.23$
Diboson	$79.10 \pm 6.23$	$12.38 \pm 1.62$
$t\bar{t}$	$35.20 \pm 3.56$	$0.00 \pm 0.00$
Other	$7.99 \pm 3.04$	$0.12 \pm 0.06$
$m = (300, 200)$ GeV	$48.33 \pm 1.64$	$27.81 \pm 0.69$
$m = (400.5, 1)$ GeV	$44.86 \pm 0.85$	$3.53 \pm 0.36$

Table 6.2: Expected background and signal yields in inclusive SRs.

analysis to see if extra cuts could be added to optimise and improve these signal regions. This is done by choosing some signal points we would like to gain sensitivity to, and then do a scan over a two dimensional parameter space of interest. The points that were chosen are the same points as were used as benchmark points in the previous sections.

In this analysis the scans are done inside the existing SRs, meaning that we keep the previous cuts (pre-selection, jet vetoes and SR definitions in Tab. 6.1), and investigate whether or not it is beneficial with some additional cuts. Some "trying and failing" was done in order to find out which variables to use in the optimisation. Eventually it was decided to do the scans on  $E_T^{\text{miss}}$  and effective mass, as neither of these variables are used yet, and there seemed to be more to gain with these variables compared to other variables that were tested.

### SR-loose optimisation

The correlation scans in SR-loose for the two benchmark points are given in Figures 6.7 and 6.8. In these plots the  $x$ -axis is effective mass and the  $y$ -axis is  $E_T^{\text{miss}}$ . Each square contains a significance value ( $Z_N$ ) which corresponds to the sensitivity we expect when cutting in  $E_T^{\text{miss}}$  or  $M_{\text{eff}}$  (or both) at that squares coordinate values. As an example on how to understand these plots let us consider the high mass splitting point in Figure 6.8. If we choose to cut at  $E_T^{\text{miss}} > 200$  GeV (and no cuts in  $M_{\text{eff}}$ ) we expect  $Z_N = 2.7$ , which is the value found in the square above  $E_T^{\text{miss}} = 200$  GeV and  $M_{\text{eff}} = 0$  GeV. Correspondingly, if we choose to cut at  $M_{\text{eff}} > 500$  GeV (and no cuts in  $E_T^{\text{miss}}$ ) we expect  $Z_N = 2.9$ . If we do both of these cuts we expect  $Z_N = 3.5$ .

As mentioned SR-loose is designed to target the signal points with somewhat low slepton masses, so in this optimisation it is really the (300, 200) GeV point that is most interesting to look at, also because the other point is well covered by SR-tight. However, both plots are included for the sake of completeness.

As can be seen in Figure 6.7 it is possible to reach higher sensitivity for the  $m = (300, 200)$  GeV point by requiring minimum values of both  $E_T^{\text{miss}}$  and  $M_{\text{eff}}$ . However, one has to keep in mind that if we optimise very specifically for one point we might lose sensitivity to other points. In addition we might be throwing away almost all the background by cutting too hard, which is undesirable. Therefore it

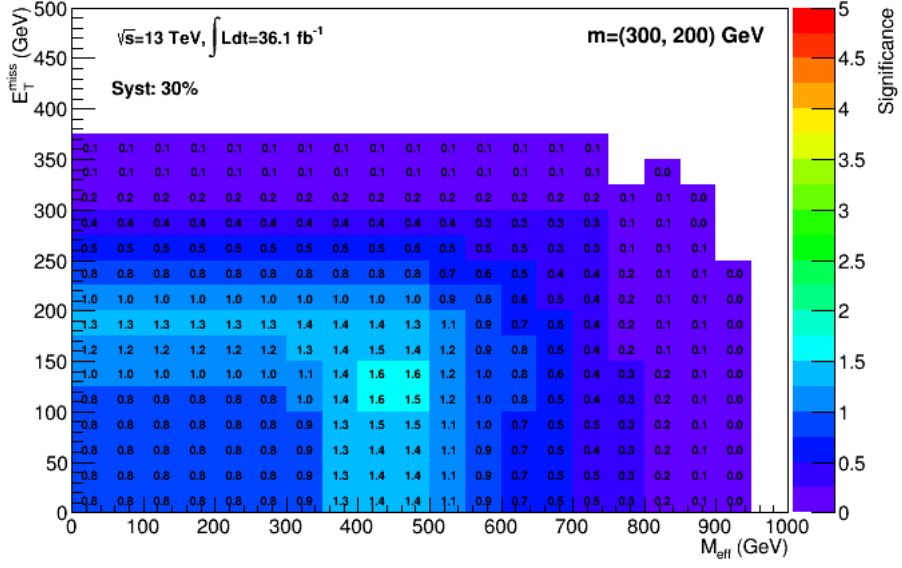


Figure 6.7: Correlation scan on  $E_T^{miss}$  and  $M_{eff}$  in SR-loose for the intermediate mass spitting point.

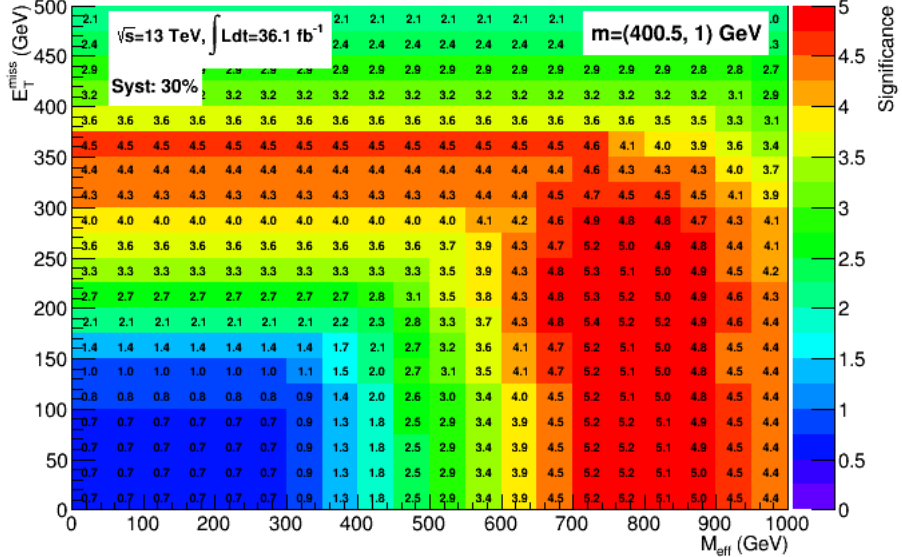


Figure 6.8: Correlation scan on  $E_T^{miss}$  and  $M_{eff}$  in SR-loose for the high mass spitting point.

was decided to try with a cut in  $E_T^{miss}$  at 125 GeV. The expected background yields with this cut are given in Table 6.3, and the sensitivities for the whole signal grid are given in Figure 6.9. We can see that we have gained sensitivity to several of the points in the middle and low areas of the grid, in addition to the benchmark

points, and the background yields are still quite high.

	SR-loose (optimised)
Expected background	$75.98 \pm 4.14$
$Z + \text{jets}$	$2.72 \pm 0.74$
Diboson	$61.55 \pm 3.40$
$t\bar{t}$	$9.04 \pm 1.75$
Other	$2.67 \pm 2.30$
$m = (300, 200) \text{ GeV}$	$38.69 \pm 0.84$
$m = (400.5, 1) \text{ GeV}$	$43.69 \pm 1.42$

Table 6.3: Expected background yields in SR-loose with additional cut at  $E_T^{miss} > 125 \text{ GeV}$ .

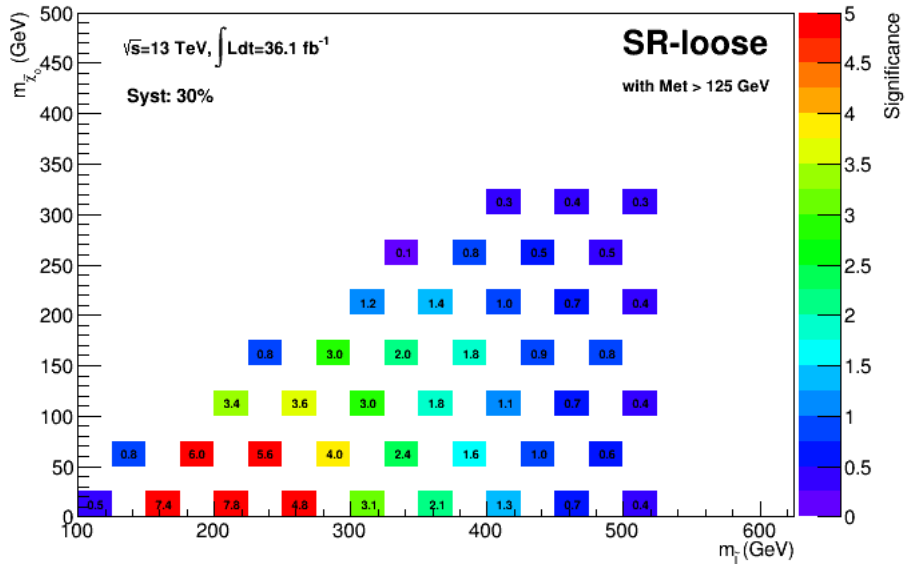


Figure 6.9: Expected sensitivity in optimised SR-loose.

### SR-tight optimisation

Correlation scans for SR-tight are given in Figures 6.10 and 6.11. From Figure 6.10 we can see that the  $(300, 200) \text{ GeV}$  point is very hard to deal with in this signal region. On the other hand, for the  $(400.5, 1) \text{ GeV}$  point we already have quite good sensitivity, but it is possible to gain something here as well by cutting in one or the other of the variables. It is also interesting to see if we can gain sensitivity for some of the signal points with even higher slepton masses by doing an additional cut.

It is chosen to try with a cut at  $M_{eff} > 600 \text{ GeV}$ . The background and signal yields after this cut are listed in Table 6.4. We see that the background yields are

now starting to get quite low, as we might would have expected since the yields were already relatively low, and we are adding a quite hard cut in  $M_{eff}$ . However, the yield for the high mass splitting signal point is quite high, which makes it clear why we have gained sensitivity to this point. Figure 6.12 shows that we have gained sensitivity to several of the other signal point with high slepton masses as well, and for some of them we have increased the sensitivity to above  $Z_N = 1.64$  by adding the  $M_{eff}$  cut.

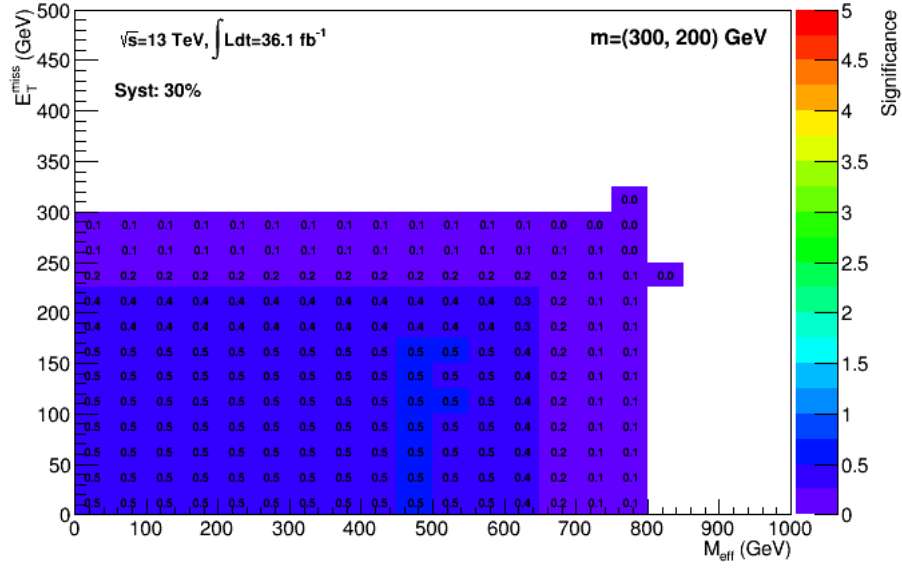


Figure 6.10: Correlation scan on  $E_T^{miss}$  and  $M_{eff}$  in SR-tight for the intermediate mass splitting point.

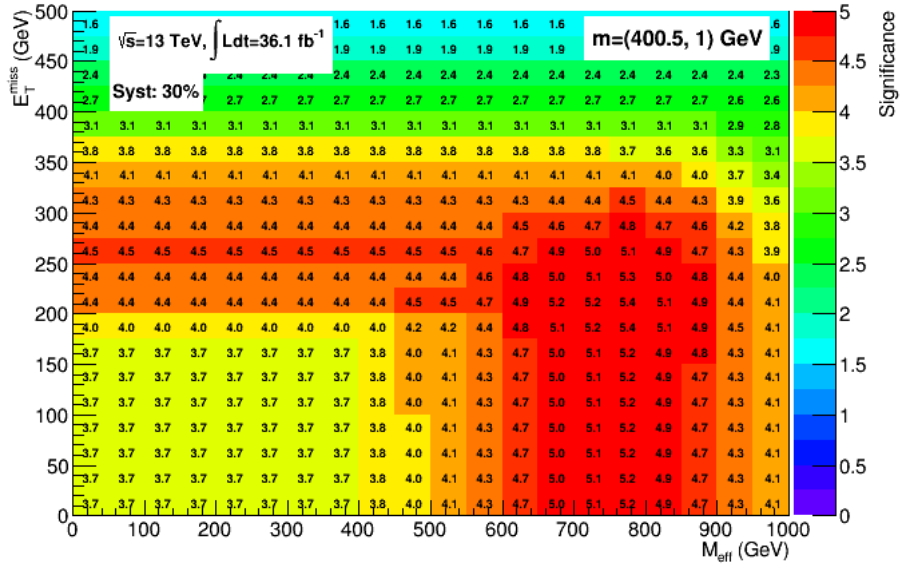


Figure 6.11: Correlation scan on  $E_T^{miss}$  and  $M_{eff}$  in SR-loose for the high mass splitting point.

SR-tight (optimised)	
Expected background	$6.77 \pm 1.19$
$Z + \text{jets}$	$0.15 \pm 0.14$
Diboson	$6.55 \pm 1.18$
$t\bar{t}$	$0.00 \pm 0.00$
Other	$0.07 \pm 0.05$
$m = (300, 200) \text{ GeV}$	$1.47 \pm 0.24$
$m = (400.5, 1) \text{ GeV}$	$25.74 \pm 0.67$

Table 6.4: Expected background and signal yields in SR-tight with additional cut at  $M_{eff} > 600 \text{ GeV}$ .

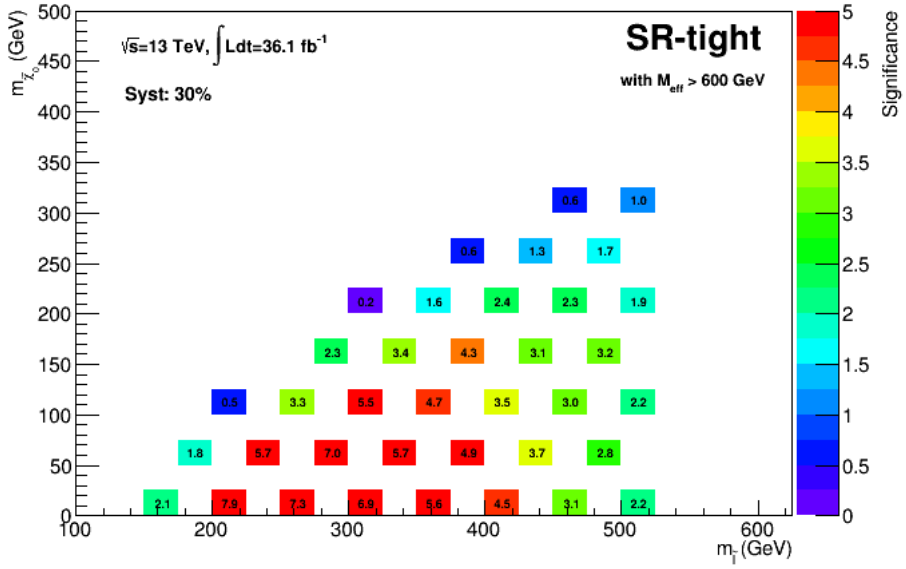


Figure 6.12: Expected sensitivity in optimised SR-tight.

### 6.2.3 Exclusive SRs

The definitions of the exclusive SRs are given in Table 6.5.  $M_{T2}$  is divided into four bins, and each of these are divided into four  $m_{\ell\ell}$  bins, except for last  $M_{T2}$  bin, where we only do one cut in  $m_{\ell\ell}$ . This is because such a hard cut in  $M_{T2}$  removes too many events, and if we apply a hard cut in  $m_{\ell\ell}$  as well we might not have anything left. The bin numbers given in Table 6.5 is just to have a way of labelling the bins, so that we don't always have to state which cuts are made, but rather which bin we are looking at.

Figures 6.13 and 6.14 show the expected sensitivity for all the 13 binned signal regions are given. As mentioned previously we see that several of these SRs only address a few points in the signal grid, but since these regions are orthogonal we can add up the sensitivities. This is done by adding the squares of the sensitivities, and then taking the square root of this. So the sensitivity,  $Z_{tot}$ , for a signal point is given as

$$Z_{tot} = \sqrt{Z_1^2 + Z_2^2 + \cdots + Z_{13}^2}, \quad (6.7)$$

where  $1, 2, \dots, 13$  denotes the bin numbers of Table 6.5. The total sensitivities are shown in Figure 6.15. With the assumed 30% flat systematic uncertainty<sup>1</sup> we can see that we now are able to exclude 37 of our 49 signal points if the data is accurately described by the background. The expected number of background events for each bin is listed in Table 6.6, as well as number of signal events for the two benchmark points.

---

<sup>1</sup>For some of the bins this is actually *not* a good approximation, which will be briefly commented in Section 6.4.3, while for other bins the assumption is reasonable. This means that the relatively high sensitivities in some of the signal points are probably not very realistic.

Exclusive signal regions		
Bin number	$M_{T2}$ (GeV)	$m_{\ell\ell}$ (GeV)
1	100 – 150	111 – 150
2		150 – 200
3		200 – 300
4		> 300
5	150 – 200	111 – 150
6		150 – 200
7		200 – 300
8		> 300
9	200 – 300	111 – 150
10		150 – 200
11		200 – 300
12		> 300
13	> 300	> 111

Table 6.5: Exclusive signal region definitions.

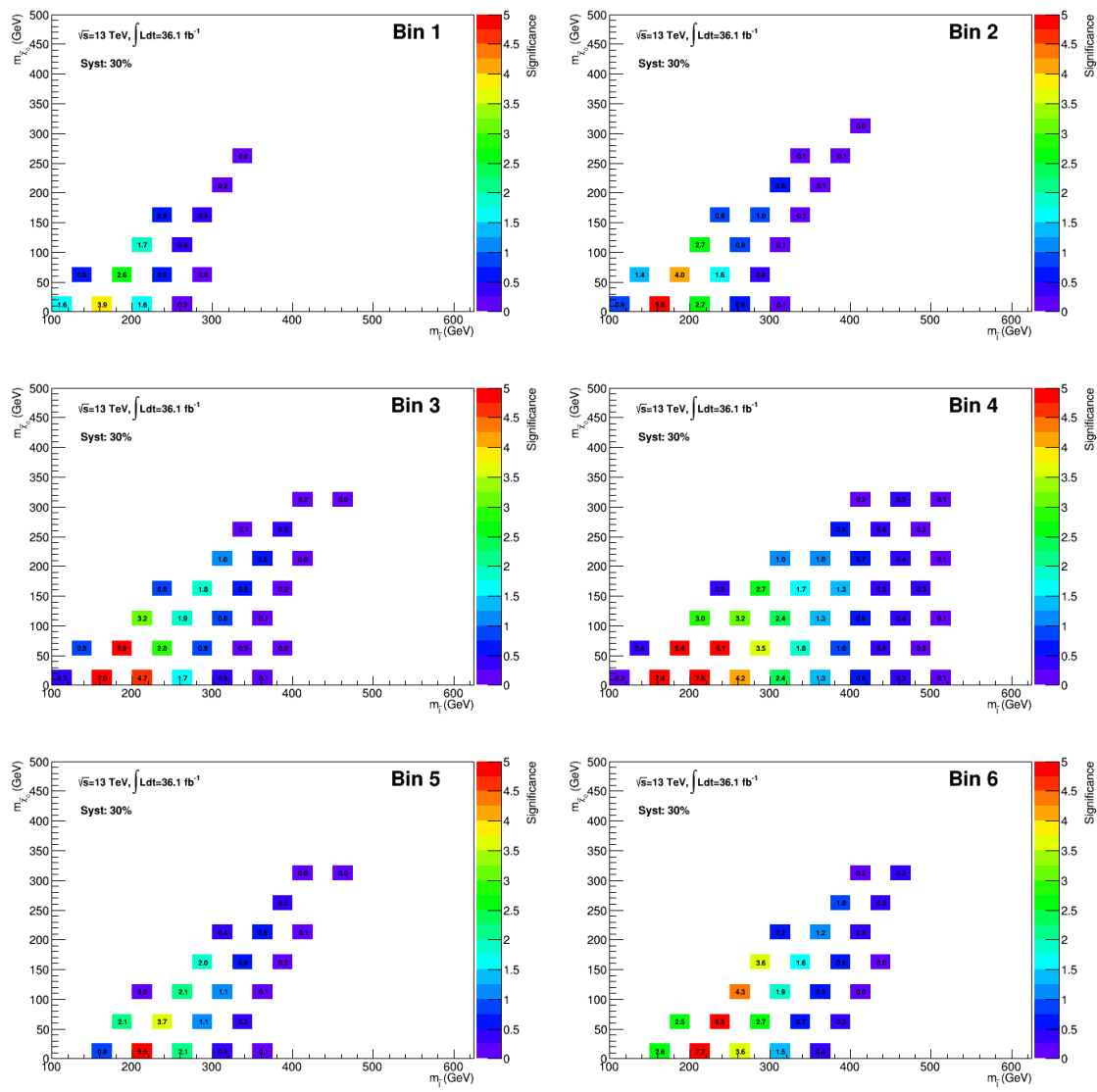


Figure 6.13: Expected sensitivities for bin 1-6.

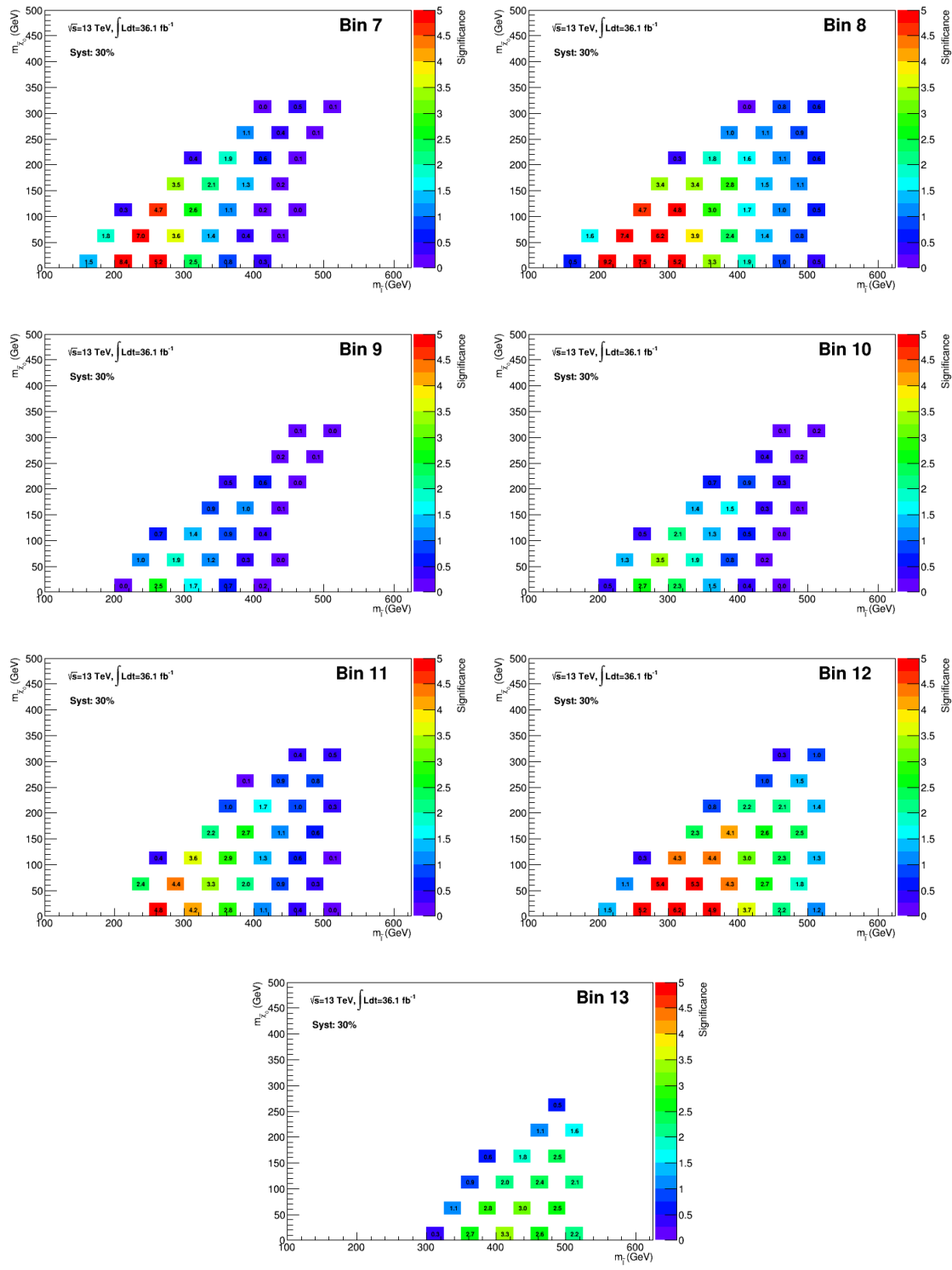


Figure 6.14: Expected sensitivities for bin 7-13.

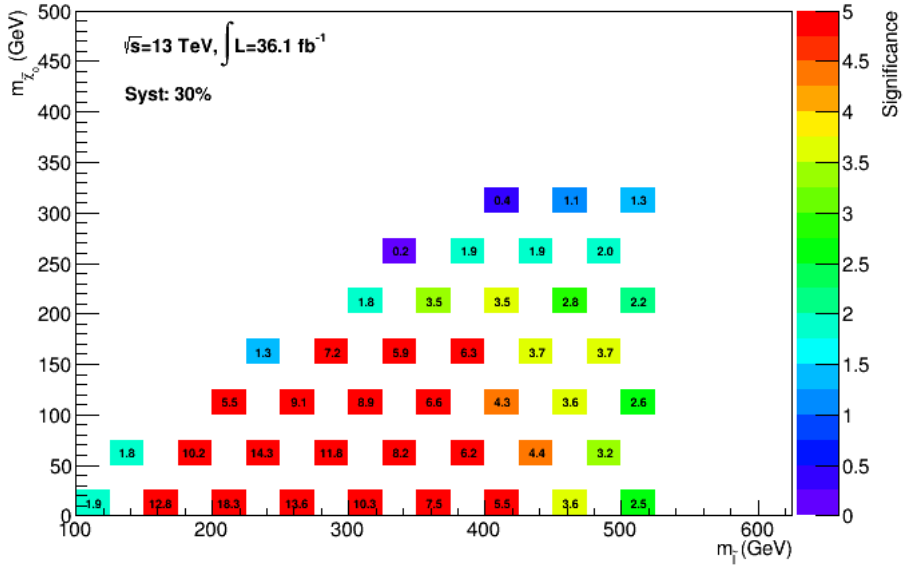


Figure 6.15: Total sensitivity for the binned signal regions.

Exclusive signal regions			
Bin number	Expected background	$m = (300, 200)$ GeV	$m = (400.5, 1)$ GeV
1	$56.10 \pm 4.96$	$8.37 \pm 0.67$	$0.22 \pm 0.06$
2	$33.75 \pm 3.50$	$10.49 \pm 0.76$	$0.44 \pm 0.07$
3	$26.06 \pm 2.69$	$12.90 \pm 0.84$	$1.16 \pm 0.13$
4	$17.70 \pm 5.36$	$9.43 \pm 0.74$	$6.26 \pm 0.29$
5	$6.59 \pm 1.18$	$2.16 \pm 0.43$	$0.27 \pm 0.06$
6	$2.46 \pm 0.58$	$2.09 \pm 0.33$	$0.45 \pm 0.08$
7	$4.02 \pm 0.84$	$1.60 \pm 0.26$	$1.33 \pm 0.13$
8	$4.08 \pm 0.69$	$1.29 \pm 0.22$	$6.45 \pm 0.34$
9	$2.45 \pm 0.82$	$0.00 \pm 0.00$	$0.92 \pm 0.11$
10	$2.15 \pm 0.62$	$0.00 \pm 0.00$	$1.27 \pm 0.14$
11	$2.15 \pm 0.49$	$0.00 \pm 0.00$	$2.55 \pm 0.20$
12	$2.89 \pm 0.85$	$0.00 \pm 0.00$	$12.25 \pm 0.46$
13	$3.62 \pm 0.79$	$0.00 \pm 0.00$	$11.22 \pm 0.42$

Table 6.6: Expected signal and background yields in exclusive SRs.

### 6.3 Background estimation

The analysis is done as a so-called *blind* analysis, which means that we must make sure that the background modelling is reasonable before we unblind the data in the SRs, which is why we need *control regions* (CRs) and *validation regions* (VRs).

These will be discussed and defined in the following, and we will also have a look at how the fake background is estimated using a data driven method.

### 6.3.1 Control regions

CRs are designed to ensure that the most important backgrounds in the analysis are well modelled. It is important that the CRs are orthogonal to the SRs<sup>2</sup>, so that we can check the background modelling independently from where we are looking for signal. But it is also a point that the CRs at the same time should be relatively close to the signal regions, because we would like to study the same kind of backgrounds that show up in the SRs, meaning that the kinematics of CRs and SRs should be as close as possible. In Section 5.8 we had a first look at data and MC background after the pre-selection was applied, and it is of course nice and important to see that the data is well modelled at that stage, but these distributions are dominated by other backgrounds than the signal regions. Hence we need to design some special control regions with a composition as signal-like as possible.

For this analysis there are two relevant control regions. The most important one is the CR for di-bosons (*CRVV-SF*), since this is the main background in the signal regions studied. There is also a CR specially designed for the  $t\bar{t}$  background (*CR-Top*), which is the second most important background.

The CRs are then used to extract additional scale factors for the respective backgrounds, i.e. one scale factor for the di-boson background and one for the  $t\bar{t}$  background, which hopefully improves the background description/modelling by correcting the MC prediction. For this reason it is important that the CRs have high purity in the kind of backgrounds they are designed for.

The definitions of the two CRs are given in Table 6.7. Notice that the subscript on the number of jets indicates the  $p_T$  threshold, so i.e. "0<sub>60</sub> central light jets" means "zero central light jets with  $p_T > 60$  GeV". The CR VV-SF requires SF lepton and the same jet vetoes as the SRs, but has an inverted  $Z$ -veto. The  $M_{T2}$  cut ensures high purity in di-bosons. The CR-Top requires DF leptons, which ensures low contamination from the  $Z+jets$  background, and by requiring at least one central b-jet we ensure high purity in top background.

	CR VV-SF	CR-Top
lepton flavour	SF	DF
central light jets	0 <sub>60</sub>	0 <sub>60</sub>
central b-jets	0 <sub>20</sub>	> 0
$ m_{\ell\ell} - m_Z $ (GeV)	< 20	—
$M_{T2}$ (GeV)	> 130	[75, 100]

Table 6.7: Control region definitions.

Figures 6.16 and 6.17 show the distributions of  $E_T^{miss}$  and sum of lepton  $p_T$  for

---

<sup>2</sup>When working in a group (like the SUSY EWK 2/3L group) there are even stricter requirements to orthogonality, because a CRs/VRs also must be orthogonal to SRs of other analyses within the group.

CR  $VV$ -SF and CR-Top respectively, and we see that the data in general seems to be quite well described by the background. Table 6.8 summarises the data and background yields in CR  $VV$ -SF, as well as the background composition. We see that the di-bosons constitutes about 85% of the total background in CR  $VV$ -SF, while the  $t\bar{t}$  background makes up about 91% of CR-Top. The scale factors are found simply by dividing number of data events by number of background events, and are of the order of 0.95, as given in Table 6.9.

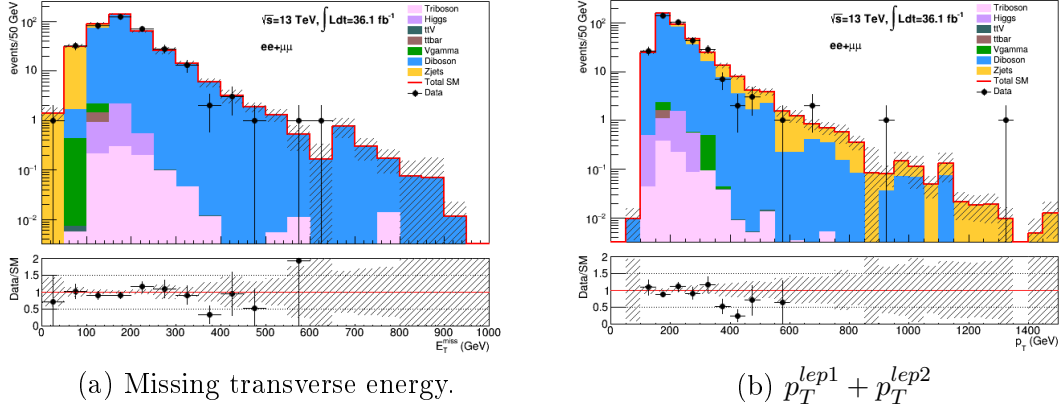


Figure 6.16: Distributions for the di-boson control region.

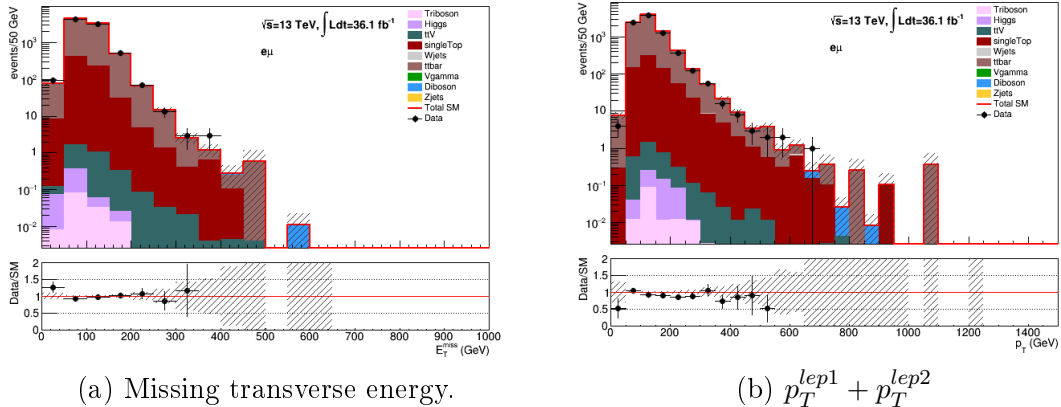


Figure 6.17: Distributions for the top control region.

## Alternative CR $VV$ -SF

While optimising the SRs and CRs the effect of an additional variable,  $\Delta\phi_b$ , was studied. Originally CR  $VV$ -SF was defined with an  $M_{T2}$  cut at 100 GeV instead of 130 GeV. This gives high  $Z+jets$  contamination, and it was discussed how to get rid of this. Before it was decided to raise the  $M_{T2}$  cut it was suggested to instead add a cut at a variable called  $\Delta\phi_b$ , which is defined as the separation in  $\phi$  between the di-lepton system and  $\mathbf{p}_T^{miss}$ . Figure 6.18 shows the distribution of this variable in CR  $VV$ -SF, with the  $M_{T2}$  cut still at 100 GeV. We can see that a cut at  $\Delta\phi_b > 2$

	CR VV-SF	CR-Top
Data	359	8170
Expected background	$377.67 \pm 9.25$	$8551.98 \pm 59.61$
$Z+jets$	$51.78 \pm 4.11$	$0.49 \pm 0.20$
Di-boson	$320.38 \pm 8.18$	$17.42 \pm 1.24$
$t\bar{t}$	$0.51 \pm 0.60$	$7819.85 \pm 58.44$
Other	$5.00 \pm 1.69$	$714.22 \pm 12.44$

Table 6.8: Background yields in control regions.

Background	Scale factor
Di-bosons	$0.9506 \pm 0.0551$
$t\bar{t}$	$0.9553 \pm 0.0125$

Table 6.9: Scale factors with uncertainties extracted from the control regions.

throws away a large fraction of the  $Z+jets$  background. The resulting background is given in Table 6.10. The di-bosons purity is about 83%, which is marginally lower than the purity achieved by raising the  $M_{T2}$  cut, hence the  $M_{T2}$  cut was preferred, also because  $M_{T2}$  is a more conventional variable used in the rest of the analysis.

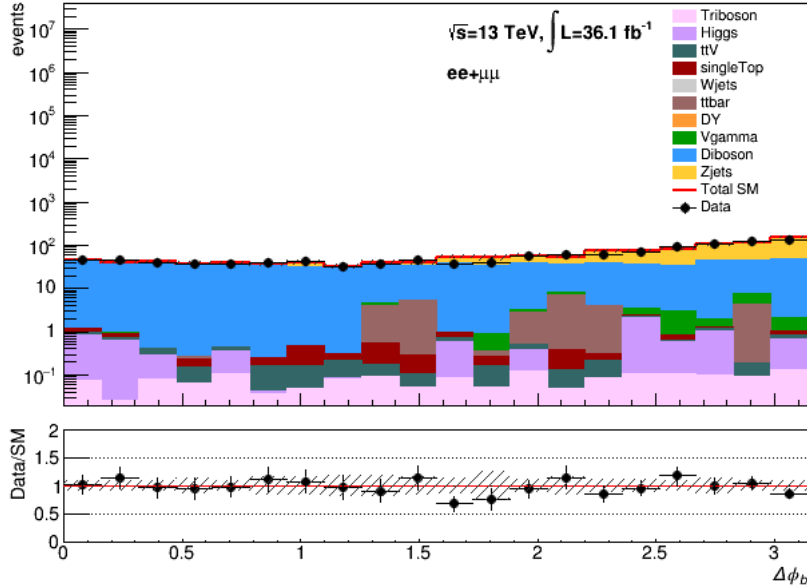


Figure 6.18:  $\Delta\phi_b$  distribution in CR VV-SF with  $M_{T2}$  cut at 100 GeV.

	CR VV-SF
Data	522
Expected background	$535.59 \pm 16.65$
$Z + \text{jets}$	$68.60 \pm 13.49$
Di-boson	$447.29 \pm 9.44$
$t\bar{t}$	$12.66 \pm 2.06$
Other	$7.04 \pm 2.40$

Table 6.10: Background yields in the alternative CR VV-SF with  $\Delta\phi_b > 2$ .

### 6.3.2 Fake background estimation

The technique used to estimate the fake background of this analysis is called the *matrix method*. Only a brief introduction is given here. More details can be found in references [25] and [26], which this summary is based on.

The matrix method requires two different selection criteria called *loose* and *tight*. The loose selection corresponds to the baseline selection of electrons and muons, while the tight selection corresponds to the signal lepton selections. (See section 5.3 for the exact definitions of these selections.)

A lepton that has passed the loose selection is referred to as *inclusive loose*, while a lepton that has passed the loose selection but *not* the tight is referred to as *exclusive loose*. The number of inclusive loose, exclusive loose and tight leptons are denoted  $N_L$ ,  $N_l$  and  $N_T$  respectively, hence  $N_L = N_l + N_T$ . A superscript  $F$  or  $R$  is added to indicate if we are talking about fake or real leptons respectively.

Two key figures in the matrix method are the fake rate ( $f$ ) and the real efficiency ( $r$ ), which are defined as

$$f = \frac{N_T^F}{N_L^F} \quad \text{and} \quad r = \frac{N_T^R}{N_L^R}, \quad (6.8)$$

where  $f$  is the probability that a fake lepton which has passed the loose selection also passes the tight selection, and  $r$  the corresponding probability for a real lepton. These can be used to express the total number of (fake and real) leptons passing the tight selection as

$$N_T = rN_L^R + fN_L^F, \quad (6.9)$$

and similarly the number of exclusive loose leptons as

$$N_l = N_L^R(1 - r) + N_L^F(1 - f). \quad (6.10)$$

The next step is to extend Equation 6.9 and 6.10 to be valid for final states with two leptons. Instead of the two equations we will now get four equations, which can be expressed by a matrix equation as

$$\begin{bmatrix} N_{TT} \\ N_{Tl} \\ N_{lT} \\ N_{ll} \end{bmatrix} = \begin{bmatrix} r_1 r_2 & r_1 f_2 & f_1 r_2 & f_1 f_2 \\ r_1(1 - r_2) & r_1(1 - f_2) & f_1(1 - r_2) & f_1(1 - f_2) \\ (1 - r_1)r_2 & (1 - r_1)f_2 & (1 - f_1)r_2 & (1 - f_1)f_2 \\ (1 - r_1)(1 - r_2) & (1 - r_1)(1 - f_2) & (1 - f_1)(1 - r_2) & (1 - f_1)(1 - f_2) \end{bmatrix} \begin{bmatrix} N_{LL}^{RR} \\ N_{LL}^{RF} \\ N_{LL}^{FR} \\ N_{LL}^{FF} \end{bmatrix} \quad (6.11)$$

where the first subscript (and superscript) represents the leading lepton and the second the sub-leading lepton, so e.g.  $N_{Tl}$  means that the leading lepton passed the tight selection and the sub-leading lepton passed only the loose selection. The efficiency and rate subscripts 1, 2 also denotes leading and sub-leading leptons respectively.

By inverting equation 6.11 we can find the number of events with two real leptons ( $N_{LL}^{RR}$ ), two fake leptons ( $N_{LL}^{FF}$ ), and one real and one fake lepton ( $N_{LL}^{RF}$  and  $N_{LL}^{FR}$ ) when we select events with two inclusive loose leptons. By multiplying by the appropriate fake rates and real efficiencies we can obtain the corresponding numbers when selecting events with two tight leptons as

$$N_{TT}^{RR} = r_1 r_2 N_{LL}^{RR} \quad (6.12)$$

$$N_{TT}^{RF} = r_1 f_2 N_{LL}^{RF} \quad (6.13)$$

$$N_{TT}^{FR} = f_1 r_2 N_{LL}^{FR} \quad (6.14)$$

$$N_{TT}^{FF} = f_1 f_2 N_{LL}^{FF}, \quad (6.15)$$

and hence the total number of events containing at least one fake lepton is given as

$$N_{\text{fake}}^{\text{tot}} = N_{TT}^{RF} + N_{TT}^{FR} + N_{TT}^{FF}. \quad (6.16)$$

In order to get something useful out of this the fake rates and the real efficiencies needs to be measured. These are usually obtained from data (and *not* MC) in some control regions with high purity in either real or fake leptons. High purity in real leptons is ensured by picking events where the two leptons have invariant mass close to (or compatible with) the  $Z$ -mass, and  $r$  is then simply the number of loose leptons divided by number of tight leptons in this region.

Control regions are also constructed for estimation of  $f$ . However, for QCD processes it is difficult to design control regions with high purity in fake leptons, especially at high  $p_T$ . In this case one has to involve Monte Carlo *truth* information. By using this information one can find out how many simulated events with two real leptons that appear in this data-based control region. Then one can subtract this number from the number of data events, and get a more realistic picture of how many fake events we actually have in the control region.

Note that  $f$  and  $r$  depend on  $p_T$  and  $\eta$ , and is therefore calculated as a function of these important variables. They must of course also be calculated separately for muons and electrons. The fake lepton background is estimated centrally in the SUSY EWK 2/3L working group, and nTuples are provided for use in analyses. In the following section we go on to validate the background estimates, both the fake and the real ones.

### 6.3.3 Validation regions

When we have extracted scale factors from the control regions we would like to construct some regions where we can validate the effect of these scale factors, i.e. that the background modelling still is good after the new scale factors are applied. Such regions are (for obvious reasons) called *validation regions*. We have one VR

for each of the control regions (VR  $VV$ -SF for di-bosons and VR-Top for  $t\bar{t}$ ), and one validation region for the fake lepton background (VR2Lfake). The validation regions must be orthogonal to the respective control regions, and of course also to the signal regions.

The definitions of the VRs are given in Table 6.11. The  $Z$ -veto makes VR  $VV$ -SF orthogonal to the corresponding control region, while the  $M_{T2}$  window makes it orthogonal to the SRs. In VR-Top we keep the requirement of DF leptons and least one b-jet from CR-Top (which ensures orthogonality to the SRs and purity in top background), and we change the  $M_{T2}$  cut to be orthogonal to CR-Top. In VR2Lfake there are no requirements to lepton flavour, but we require same sign (SS) leptons, and we also do a  $Z$ -veto and a cut in  $M_{T2}$ . It should be noted that VRs don't necessarily have to be as pure as the CRs in the targeted backgrounds, since we don't use them to extract scale factors, but rather to validate the effect of the scale factors.

Distributions for VR  $VV$ -SF, VR-Top and VR2Lfake are shown in Figures 6.19, 6.20 and 6.21 respectively, and the data and MC background yields are given in Table 6.12. It is noteworthy that in both CR  $VV$ -SF and CR-Top we had more data events than background events, while in VR  $VV$ -SF and VR-Top it is the other way around. However, the agreement between data and background still seem to be quite good, at least in the bins with somewhat high statistics. Also the fake lepton background seem to be quite well modelled.

	VR $VV$ -SF	VR-Top	VR2Lfake
lepton	$\ell^+\ell^-$	$\ell^+\ell^-$	$\ell^\pm\ell^\pm$
lepton flavour	SF	DF	all
central light jets	$0_{60}$	$0_{60}$	—
central b-jets	$0_{20}$	$> 0$	—
$ m_{\ell\ell} - m_Z $ (GeV)	$> 20$	—	$> 20$
$M_{T2}$ (GeV)	[75, 100]	$> 100$	$> 40$

Table 6.11: Validation region definitions.

	VR $VV$ -SF	VR-Top	VR2Lfake
Data	2068	345	4290
Estimated background	$1986.39 \pm 46.57$	$324.46 \pm 12.98$	$4617.95 \pm 89.67$
$Z + \text{jets}$	$390.05 \pm 31.84$	$0.17 \pm 0.11$	$157.92 \pm 24.19$
Di-boson	$522.63 \pm 10.23$	$1.80 \pm 0.32$	$702.32 \pm 6.97$
$t\bar{t}$	$779.45 \pm 17.53$	$289.60 \pm 11.41$	$293.69 \pm 10.72$
Fake	$37.53 \pm 25.99$	$1.91 \pm 5.70$	$3250.99 \pm 85.10$
Other	$256.73 \pm 12.66$	$30.99 \pm 2.48$	$213.03 \pm 13.86$

Table 6.12: Data and background yields in validation regions.

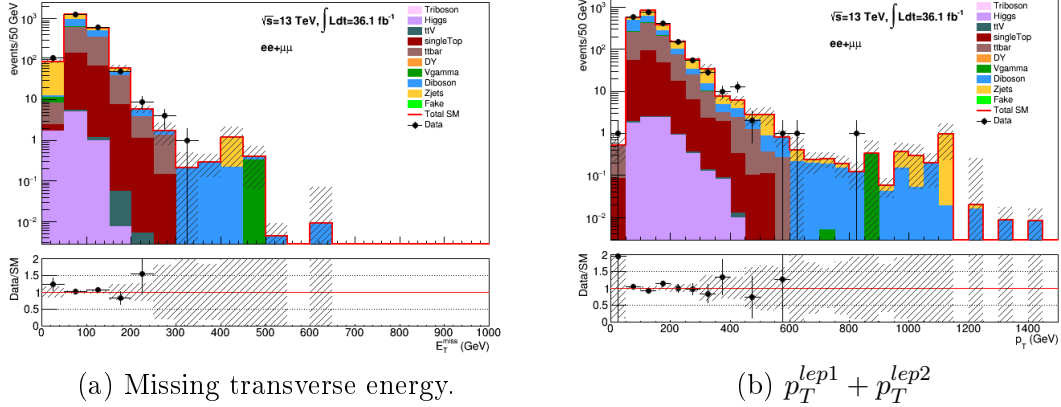


Figure 6.19: Distributions for the di-boson validation region.

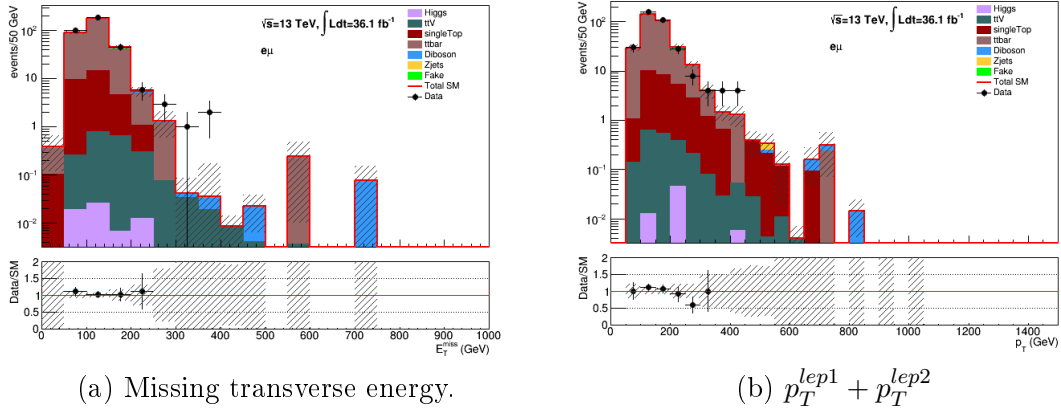


Figure 6.20: Distributions for the top validation region.

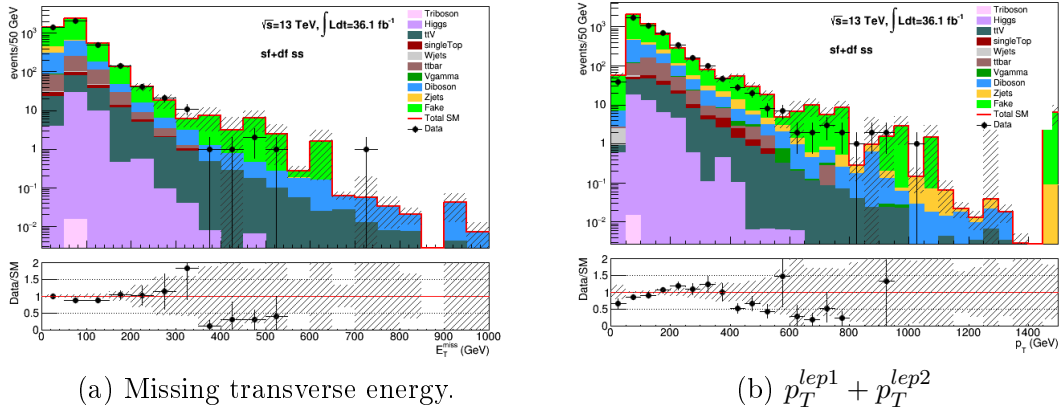


Figure 6.21: Distributions for the fake lepton validation region.

## 6.4 Results

In this section the unblinded results of the search for direct production of sleptons are presented. This includes comparisons between data and the estimated back-

ground both for the inclusive and the exclusive SRs. The background yields have now been updated to include the estimated fake background, and also the scale factors from Table 6.9 are applied to the di-boson and  $t\bar{t}$  background. Notice that the inclusive SRs used here are those defined in Table 6.1, and *not* the ones defined in the further optimisation studies.

#### 6.4.1 Inclusive SRs

Table 6.13 gives the number of observed events together with the estimated background yields for SR-loose and SR-tight, while the corresponding  $E_T^{miss}$  distributions are shown in Figure 6.22. All in all we can conclude that the data are well described by the estimated background. In SR-tight the background "overshoots" the data a little bit, while in SR-loose there is a small excess of data. By using the ROOT function `RooStats.NumberCountingUtils.BinomialObsZ` and assuming 30% systematic uncertainty the excess in SR-loose can be calculated to be  $0.09\sigma$ , or in other words *very* small. It is however worth noting that the tail of the  $E_T^{miss}$  distribution in both SRs have some discrepancies between data and background, but the statistics is of course extremely low in these areas, and systematic uncertainties are not taken into account.

	SR-loose	SR-tight
Observed events	163	9
Estimated background	$149.46 \pm 14.23$	$11.62 \pm 1.54$
$Z + \text{jets}$	$31.65 \pm 4.89$	$0.36 \pm 0.23$
Diboson	$74.02 \pm 5.90$	$11.21 \pm 1.44$
$t\bar{t}$	$33.36 \pm 3.39$	$0.00 \pm 0.00$
Fakes	$4.07 \pm 11.46$	$0.05 \pm 0.50$
Other	$6.36 \pm 1.62$	$0.01 \pm 0.00$

Table 6.13: Observed data events and estimated background yields in inclusive SRs.

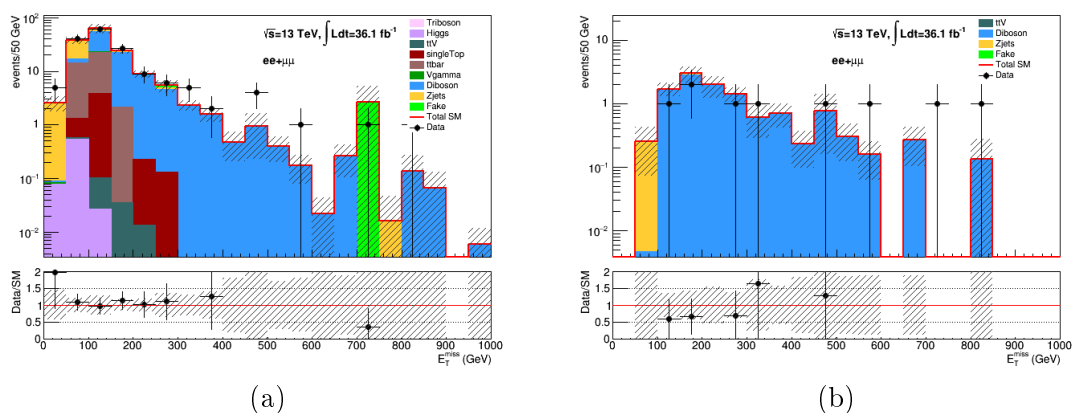


Figure 6.22:  $E_T^{miss}$  distributions for a) SR-loose and b) SR-tight.

### 6.4.2 Exclusive SRs

The observed number of events and the estimated number of background events for the exclusive SRs are shown in Table 6.14. The observed number of events mostly agrees well with the predictions. There are however some small excesses in some of the bins, where the largest ones occur in Bin 5, 6 and 13. The significance of the (local) excesses in these bins are calculated (assuming 30% systematic uncertainties) to be  $1.34\sigma$ ,  $1.54\sigma$  and  $1.93\sigma$  respectively, meaning that they are nowhere near being significant. It is also noteworthy that, because of the very limited statistics in some of the bins, the systematics uncertainties might even be larger than 30%, so the significance values given here should be taken with a "grain of salt".

Exclusive signal regions		
Bin number	Observed events	Estimated background
1	60	$55.48 \pm 7.85$
2	31	$32.93 \pm 8.63$
3	19	$26.51 \pm 3.98$
4	13	$23.06 \pm 6.65$
5	12	$6.32 \pm 1.16$
6	6	$2.34 \pm 0.67$
7	6	$4.68 \pm 1.31$
8	0	$3.80 \pm 0.66$
9	1	$2.28 \pm 0.78$
10	3	$2.13 \pm 0.61$
11	2	$2.04 \pm 0.52$
12	2	$2.75 \pm 0.93$
13	8	$2.84 \pm 0.57$

Table 6.14: Observed data events and estimated background yields in exclusive SRs.

### 6.4.3 Concluding remarks

To summarize the result section we have seen no significant excess above the expected background in any of the signal regions considered. The natural next step of the analysis would be to put new limits on the slepton and neutralino masses. However, the unblinding approval for the SRs was given quite close to the deadline for delivery of this thesis, which meant that there was unfortunately not enough time to contribute to the extraction of the limits.

Another important part that is not included in this analysis is systematic uncertainties. It was agreed upon that this was beyond the scope of this thesis, both because of the level of difficulty this introduces, but also because of the limited time of the project. The largest contributions to systematic uncertainties comes from resolution and energy scale of jets and  $E_T^{miss}$ , efficiency of the algorithms for identification of objects, uncertainties in weights, scale factors and luminosity, the fake background estimation and theoretical uncertainties (cross sections of signal and SM background processes).

In the analysis done in the SUSY EWK 2/3L working group the total systematic uncertainties are estimated to be  $\sim 15\%$  in SR-loose and  $\sim 30\%$  in SR-tight, while they vary between  $\sim 15\%$  and  $\sim 65\%$  in the binned SRs. This means that the assumption of 30% flat systematic uncertainties used in this analysis sometimes is conservative, and sometimes rather optimistic. In particular the assumption is optimistic in some of the binned SRs, which is why significances and sensitivities given for these should maybe be taken as indicative.

The new exclusion limits are of course also included in the official analysis, and they are presented in Figure 6.23 below. We can see that for a light neutralino the limit on the slepton mass has been extended from about 350 GeV to about 450 GeV, and the upper limit of the slepton mass is excluded up to a neutralino mass of about 200 GeV, compared to about 150 GeV in Run 1. These limits, and other results from the working group, are presented at the LHCP conference in Shanghai 15th-20th May 2017 [89], and included in the associated conference note.

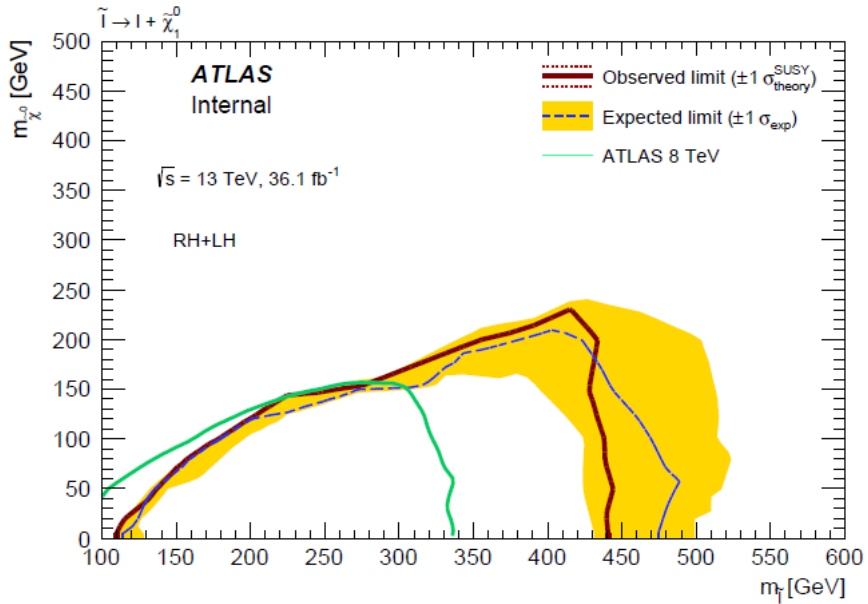


Figure 6.23: Exclusion limits on the slepton and neutralino mass, as presented in the official analysis by the SUSY EWK 2/3L working group.

# Summary and Conclusions

In 2015 the LHC collided, for the first time, two proton beams at a centre-of-mass energy,  $\sqrt{s} = 13$  TeV, which is (by far) the highest energy ever achieved in a particle collider. During the LHC runs of 2015 and 2016 the ATLAS experiment has collected a total of  $36.1 \text{ fb}^{-1}$  of data from these proton-proton collisions. The main objective when studying such collisions is to find hints of so-called "new physics", which in high energy particle physics means observations that cannot be explained by the Standard Model.

In this thesis the data set collected by ATLAS has been used in a search for Supersymmetry, which is a possible extension of the Standard Model predicting the existence of (approximately) twice as many elementary particles as we know exists today. The specific supersymmetric process that was targeted by the analysis was direct production of sleptons, which decay to their lepton partners and neutralinos. No significant excess of data above the expected Standard Model background was observed.

For two more years (2017 and 2018) the LHC is expected to continue delivering proton-proton collisions at the same energy and about the same luminosity as it has for the last two years. Then a long shut-down is scheduled, with upgrades of both the accelerator and the experiments, which will be followed by runs with even higher luminosity than now, as well as collision energies up to 14 TeV. This will give sensitivity to larger and larger parts of the parameter space of Supersymmetry, and hence extend the opportunities for discoveries.

However, there is of course also the possibility that neither Supersymmetry nor other kinds of physics beyond the Standard Model are to be discovered with the LHC. This unfortunate scenario would lead to a need for new experimental (and maybe also theoretical) approaches, because we know that there must be something more than the Standard Model, the question is simply what it is and how to find it.

# Appendix A

## Lists of MC samples

### A.1 Background samples

Di-bosons			
Sample ID	Name	Generator	$\sigma$ [pb]
363490	$Z\ell\ell Z\ell\ell$	SHERPA	1.255570
363491	$Z\ell\ell W\ell\nu$	SHERPA	4.58770
363492	$\ell\ell\nu\nu$	SHERPA	12.465
361071	$\ell\ell\ell\nu jj$ _EW6	SHERPA	0.042
361072	$\ell\ell\ell\nu jj$ _EW6	SHERPA	0.031
361073	$g\ell\ell\ell\ell$	SHERPA	0.021
361077	$g\ell\ell\ell\nu\nu$	SHERPA	0.854
361094	$WqqZ\ell\ell$	SHERPA	3.423
361096	$ZqqZ\ell\ell$	SHERPA	2.353

Table A.1: Di-boson background samples.

Tri-bosons			
Sample ID	Name	Generator	$\sigma$ [pb]
407311	$6\ell 0\nu$	SHERPA	0.00010235
407312	$5\ell 1\nu$	SHERPA	0.00056766
407313	$4\ell 2\nu$	SHERPA	0.0043684
407314	$3\ell 3\nu$	SHERPA	0.015846

Table A.2: Tri-boson background samples

<b><math>Z + \text{jets}</math></b>				
Sample ID	Name	Generator	$\sigma$ [pb]	
Unfiltered slices				
364112	Zmumu_MAXHTPTV500_1000	SHERPA	1.7881	
364113	Zmumu_MAXHTPTV1000_E_CMS	SHERPA	0.14769	
364126	Zee_MAXHTPTV500_1000	SHERPA	1.8081	
364127	Zee_MAXHTPTV1000_E_CMS	SHERPA	0.14857	
364140	Ztautau_MAXHTPTV500_1000	SHERPA	1.8096	
364141	Ztautau_MAXHTPTV1000_E_CMS	SHERPA	0.14834	
B-filtered slices				
364102	Zmumu_MAXHTPTV0_70	SHERPA	1982.2	
364105	Zmumu_MAXHTPTV70_140	SHERPA	108.91	
364108	Zmumu_MAXHTPTV140_280	SHERPA	39.908	
364111	Zmumu_MAXHTPTV280_500	SHERPA	8.4932	
364116	Zee_MAXHTPTV0_70	SHERPA	1981.7	
364119	Zee_MAXHTPTV70_140	SHERPA	110.31	
364122	Zee_MAXHTPTV140_280	SHERPA	40.643	
364125	Zee_MAXHTPTV280_500	SHERPA	8.6766	
364130	Ztautau_MAXHTPTV0_70	SHERPA	1981.8	
364133	Ztautau_MAXHTPTV70_140	SHERPA	110.87	
364136	Ztautau_MAXHTPTV140_280	SHERPA	40.761	
364139	Ztautau_MAXHTPTV280_500	SHERPA	8.6804	
C-filtered slices				
364101	Zmumu_MAXHTPTV0_70	SHERPA	1978.4	
364104	Zmumu_MAXHTPTV70_140	SHERPA	109.42	
364107	Zmumu_MAXHTPTV140_280	SHERPA	39.795	
364110	Zmumu_MAXHTPTV280_500	SHERPA	8.5403	
364115	Zee_MAXHTPTV0_70	SHERPA	1980.8	
364118	Zee_MAXHTPTV70_140	SHERPA	110.63	
364121	Zee_MAXHTPTV140_280	SHERPA	40.67	
364124	Zee_MAXHTPTV280_500	SHERPA	8.6711	
364129	Ztautau_MAXHTPTV0_70	SHERPA	1978.8	
364132	Ztautau_MAXHTPTV70_140	SHERPA	110.51	
364135	Ztautau_MAXHTPTV140_280	SHERPA	40.74	
364138	Ztautau_MAXHTPTV280_500	SHERPA	8.6707	
L-filtered slices				
364100	Zmumu_MAXHTPTV0_70	SHERPA	1983.0	
364103	Zmumu_MAXHTPTV70_140	SHERPA	108.92	
364106	Zmumu_MAXHTPTV140_280	SHERPA	39.878	
364109	Zmumu_MAXHTPTV280_500	SHERPA	8.5375	
364114	Zee_MAXHTPTV0_70	SHERPA	1981.8	
364117	Zee_MAXHTPTV70_140	SHERPA	110.5	
364120	Zee_MAXHTPTV140_280	SHERPA	40.731	
364123	Zee_MAXHTPTV280_500	SHERPA	8.6743	
364128	Ztautau_MAXHTPTV0_70	SHERPA	1981.6	
364131	Ztautau_MAXHTPTV70_140	SHERPA	110.37	
364134	Ztautau_MAXHTPTV140_280	SHERPA	40.781	
364137	Ztautau_MAXHTPTV280_500	SHERPA	8.5502	

Table A.3:  $Z + \text{jets}$  background samples.

<b><math>V + \gamma</math></b>			
Sample ID	Name	Generator	$\sigma$ [pb]
301535	$ee + \gamma$ _Pt10_35	SHERPA	52.706
301536	$\mu\mu + \gamma$ _Pt10_35	SHERPA	52.708
301890	$e\nu + \gamma$ _Pt35_70	SHERPA	15.348
301891	$e\nu + \gamma$ _Pt70_140	SHERPA	1.5282
301892	$e\nu + \gamma$ _Pt140	SHERPA	0.24155
301893	$\mu\nu + \gamma$ _Pt35_70	SHERPA	15.272
301894	$\mu\nu + \gamma$ _Pt70_140	SHERPA	1.5235
301895	$\mu\nu + \gamma$ _Pt140	SHERPA	0.24183
301896	$\tau\nu + \gamma$ _Pt35_70	SHERPA	15.297
301897	$\tau\nu + \gamma$ _Pt70_140	SHERPA	1.529
301898	$\tau\nu + \gamma$ _Pt140	SHERPA	0.2426
301899	$ee + \gamma$ _Pt35_70	SHERPA	5.242
301900	$ee + \gamma$ _Pt70_140	SHERPA	0.38455
301901	$ee + \gamma$ _Pt140	SHERPA	0.047209
301902	$\mu\mu + \gamma$ _Pt35_70	SHERPA	5.2455
301903	$\mu\mu + \gamma$ _Pt70_140	SHERPA	0.38548
301904	$\mu\mu + \gamma$ _Pt140	SHERPA	0.04724
301905	$\tau\tau + \gamma$ _Pt35_70	SHERPA	5.249
301906	$\tau\tau + \gamma$ _Pt70_140	SHERPA	0.38482
301907	$\tau\tau + \gamma$ _Pt140	SHERPA	0.047025

Table A.4:  $V + \gamma$  background samples.

<b>Drell-Yan</b>			
Sample ID	Name	Generator	$\sigma$ [pb]
364198	Zmm_Mll10_40_MAXHTPTV0_70_BVeto	SHERPA	2413.7
364199	Zmm_Mll10_40_MAXHTPTV0_70_BFilter	SHERPA	2414.7
364200	Zmm_Mll10_40_MAXHTPTV70_280_BVeto	SHERPA	50.318
364201	Zmm_Mll10_40_MAXHTPTV70_280_BFilter	SHERPA	50.285
364202	Zmm_Mll10_40_MAXHTPTV280_E_CMS_BVeto	SHERPA	3.2355
364203	Zmm_Mll10_40_MAXHTPTV280_E_CMS_BFilter	SHERPA	3.28
364204	Zee_Mll10_40_MAXHTPTV0_70_BVeto	SHERPA	2415.7
364205	Zee_Mll10_40_MAXHTPTV0_70_BFilter	SHERPA	2416.9
364206	Zee_Mll10_40_MAXHTPTV70_280_BVeto	SHERPA	50.456
364207	Zee_Mll10_40_MAXHTPTV70_280_BFilter	SHERPA	50.427
364208	Zee_Mll10_40_MAXHTPTV280_E_CMS_BVeto	SHERPA	3.2538
364209	Zee_Mll10_40_MAXHTPTV280_E_CMS_BFilter	SHERPA	3.2519
364210	Ztt_Mll10_40_MAXHTPTV0_70_BVeto	SHERPA	2417.9
364211	Ztt_Mll10_40_MAXHTPTV0_70_BFilter	SHERPA	2414.2
364212	Ztt_Mll10_40_MAXHTPTV70_280_BVeto	SHERPA	50.37
364213	Ztt_Mll10_40_MAXHTPTV70_280_BFilter	SHERPA	50.44
364214	Ztt_Mll10_40_MAXHTPTV280_E_CMS_BVeto	SHERPA	3.2834
364215	Ztt_Mll10_40_MAXHTPTV280_E_CMS_BFilter	SHERPA	3.2788

Table A.5: Drell-Yan (low- $m_{\ell\ell}$ ) background samples.

<b><math>W+jets</math></b>				
Sample ID	Name	Generator	$\sigma$ [pb]	
Unfiltered slices				
364168	Wmunu_MAXHTPTV500_1000	SHERPA	15.01	
364169	Wmunu_MAXHTPTV1000_E_CMS	SHERPA	1.2344	
364182	Wenu_MAXHTPTV500_1000	SHERPA	15.224	
364183	Wenu_MAXHTPTV1000_E_CMS	SHERPA	1.2334	
364196	Wtaunu_MAXHTPTV500_1000	SHERPA	15.046	
364197	Wtaunu_MAXHTPTV1000_E_CMS	SHERPA	1.2339	
Bfiltered slices				
364158	Wmunu_MAXHTPTV0_70_BFilter	SHERPA	19135.0	
364161	Wmunu_MAXHTPTV70_140_BFilter	SHERPA	944.63	
364164	Wmunu_MAXHTPTV140_280_BFilter	SHERPA	339.54	
364167	Wmunu_MAXHTPTV280_500_BFilter	SHERPA	72.045	
364172	Wenu_MAXHTPTV0_70_BFilter	SHERPA	19135.0	
364175	Wenu_MAXHTPTV70_140_BFilter	SHERPA	945.15	
364178	Wenu_MAXHTPTV140_280_BFilter	SHERPA	339.48	
364181	Wenu_MAXHTPTV280_500_BFilter	SHERPA	72.113	
364186	Wtaunu_MAXHTPTV0_70_BFilter	SHERPA	19163.0	
364189	Wtaunu_MAXHTPTV70_140_BFilter	SHERPA	943.30	
364192	Wtaunu_MAXHTPTV140_280_BFilter	SHERPA	339.54	
364195	Wtaunu_MAXHTPTV280_500_BFilter	SHERPA	72.026	
Cfiltered slices				
364157	Wmunu_MAXHTPTV0_70_CFilterBVeto	SHERPA	19121.0	
364160	Wmunu_MAXHTPTV70_140_CFilterBVeto	SHERPA	937.78	
364163	Wmunu_MAXHTPTV140_280_CFilterBVeto	SHERPA	340.06	
364166	Wmunu_MAXHTPTV280_500_CFilterBVeto	SHERPA	72.198	
364171	Wenu_MAXHTPTV0_70_CFilterBVeto	SHERPA	19130.0	
364174	Wenu_MAXHTPTV70_140_CFilterBVeto	SHERPA	945.67	
364177	Wenu_MAXHTPTV140_280_CFilterBVeto	SHERPA	339.87	
364180	Wenu_MAXHTPTV280_500_CFilterBVeto	SHERPA	72.128	
364185	Wtaunu_MAXHTPTV0_70_CFilterBVeto	SHERPA	19153.0	
364188	Wtaunu_MAXHTPTV70_140_CFilterBVeto	SHERPA	946.73	
364191	Wtaunu_MAXHTPTV140_280_CFilterBVeto	SHERPA	339.63	
364194	Wtaunu_MAXHTPTV280_500_CFilterBVeto	SHERPA	71.976	
Lfiltered slices				
364156	Wmunu_MAXHTPTV0_70_CVetoBVeto	SHERPA	19143.0	
364159	Wmunu_MAXHTPTV70_140_CVetoBVeto	SHERPA	944.85	
364162	Wmunu_MAXHTPTV140_280_CVetoBVeto	SHERPA	339.54	
364165	Wmunu_MAXHTPTV280_500_CVetoBVeto	SHERPA	72.067	
364170	Wenu_MAXHTPTV0_70_CVetoBVeto	SHERPA	19127.0	
364173	Wenu_MAXHTPTV70_140_CVetoBVeto	SHERPA	942.58	
364176	Wenu_MAXHTPTV140_280_CVetoBVeto	SHERPA	339.81	
364179	Wenu_MAXHTPTV280_500_CVetoBVeto	SHERPA	72.084	
364184	Wtaunu_MAXHTPTV0_70_CVetoBVeto	SHERPA	19152.0	
364187	Wtaunu_MAXHTPTV70_140_CVetoBVeto	SHERPA	947.65	
364190	Wtaunu_MAXHTPTV140_280_CVetoBVeto	SHERPA	339.36	
364193	Wtaunu_MAXHTPTV280_500_CVetoBVeto	SHERPA	72.065	

Table A.6:  $W+jets$  background samples.

$t\bar{t}$			
Sample ID	Name	Generator	$\sigma$ [pb]
410009	PowhegPythiaEvtGen_P2012_ttbar_hdamp172p5_dil	POWHEGPYTHIA6	696.12

Table A.7:  $t\bar{t}$  background sample.

Single top			
Sample ID	Name	Generator	$\sigma$ [pb]
410015	$Wt$	POWHEGPYTHIA	3.584
410016	$W\bar{t}$	POWHEGPYTHIA	3.581
410011	$t$ -channel top	POWHEGPYTHIA	43.739
410012	$t$ -channel anti-top	POWHEGPYTHIA	25.778
410025	$s$ -channel top	POWHEGPYTHIA	2.052
410026	$s$ -channel anti-top	POWHEGPYTHIA	1.262

Table A.8: Single top background samples.

$t\bar{t}+V$			
Sample ID	Name	Generator	$\sigma$ [pb]
410218	$t\bar{t}+ee$	AMC@NLO+PYTHIA8	0.036888
410219	$t\bar{t}+\mu\mu$	AMC@NLO+PYTHIA8	0.036895
410220	$t\bar{t}+\tau\tau$	AMC@NLO+PYTHIA8	0.036599
410155	$t\bar{t}+W$	AMC@NLO+PYTHIA8	0.54830
410081	$t\bar{t}+WW$	MADGRAPH+PYTHIA8	0.0081
407321	$t\bar{t}+WW$	MADGRAPH+PYTHIA8	0.000266

Table A.9:  $t\bar{t} + V$  background samples.

Higgs			
Sample ID	Name	Generator	$\sigma$ [pb]
341079	ggH125_WWlrv	POWHEGPYTHIA8	0.9902
341122	ggH125_tautaull	POWHEGPYTHIA8	1.9081
341195	ggH125_mumu	POWHEGPYTHIA8	0.0066
342178	ggH125_ee	POWHEGPYTHIA8	1.5469e-07
341080	VBFH125_WWlrv	POWHEGPYTHIA8	0.0848
341155	VBFH125_tautaull	POWHEGPYTHIA8	0.2420
341206	VBFH125_mumu	POWHEGPYTHIA8	0.0008
342189	VBFH125_ee	POWHEGPYTHIA8	1.9628e-08
342284	WH125_inc	PYTHIA8	1.1021
342285	ZH125_inc	PYTHIA8	0.6007
341270	ttH125_inc_semil	AMC@NLO+HERWIGPP	0.5085

Table A.10: Higgs background samples.

## A.2 Signal samples

Sample ID	$m_{\tilde{\ell}} [\text{GeV}]$	$m_{\tilde{\chi}_1^0} [\text{GeV}]$	$\sigma_R [\text{pb}]$	$\sigma_L [\text{pb}]$
392916	100.5	1.0	0.2669	0.0952
392917	150.5	1.0	0.0627	0.0231
392918	200.5	1.0	0.0216	0.0081
392919	250.5	1.0	0.0091	0.0034
392920	300.5	1.0	0.0044	0.0017
392921	350.5	1.0	0.0023	0.0009
392922	400.5	1.0	0.0013	0.0005
392923	450.5	1.0	0.0008	0.0003
392924	500.5	1.0	0.0005	0.0002
392925	100	50	0.2708	0.0965
392926	125	50	0.1316	0.0477
392927	175	50	0.0373	0.0138
392928	225	50	0.0142	0.0053
392929	275	50	0.0064	0.0024
392930	325	50	0.0032	0.0012
392931	375	50	0.0017	0.0007
392932	425	50	0.0010	0.0004
392933	475	50	0.0006	0.0002
392934	125	100	0.1316	0.0477
392935	150	100	0.0633	0.0233
392936	200	100	0.0218	0.0081
392937	250	100	0.0092	0.0035
392938	300	100	0.0044	0.0017
392939	350	100	0.0023	0.0009
392940	400	100	0.0013	0.0005
392941	450	100	0.0008	0.0003
392942	500	100	0.0005	0.0002
392943	175	150	0.0373	0.0138
392944	225	150	0.0142	0.0053
392945	275	150	0.0064	0.0024
392946	325	150	0.0032	0.0012
392947	375	150	0.0017	0.0007
392948	425	150	0.0010	0.0004
392949	475	150	0.0006	0.0002
392950	250	200	0.0092	0.0035
392951	300	200	0.0044	0.0017
392952	350	200	0.0023	0.0009
392953	400	200	0.0013	0.0005
392954	450	200	0.0008	0.0003
392955	500	200	0.0005	0.0002
392956	275	250	0.0064	0.0024
392957	325	250	0.0032	0.0012
392958	375	250	0.0017	0.0007
392959	425	250	0.0010	0.0004
392960	475	250	0.0006	0.0002
392961	350	300	0.0023	0.0009
392962	400	300	0.0013	0.0005
392963	450	300	0.0008	0.0003
392964	500	300	0.0005	0.0002

Table A.11: Direct slepton signal samples.

# Bibliography

- [1] S. Glashow (1961). Partial-symmetries of weak interactions, *Nuclear Physics*, Vol. 22, p. 579-588.  
<http://www.sciencedirect.com/science/article/pii/0029558261904692>
- [2] S. Weinberg (1967). A Model of Leptons, *Phys. Rev. Letters*, Vol. 19, p. 1264-1266.  
<https://journals.aps.org/prl/abstract/10.1103/PhysRevLett.19.1264>
- [3] A. Salam (1968). N. Svartholm, ed. Elementary Particle Physics: Relativistic Groups and Analyticity. Eighth Nobel Symposium. Stockholm: Almqvist and Wiksell. p. 367-377.
- [4] P. Higgs (1964). Broken Symmetries and the Masses of Gauge Bosons, *Phys. Rev. Letters*, Vol. 13, p. 508-509.  
<https://journals.aps.org/prl/abstract/10.1103/PhysRevLett.13.508>
- [5] R. Brout, F. Englert (1964). Broken Symmetry and the Mass of Vector Mesons, *Phys. Rev. Letters*, Vol. 13, p. 321-323.  
<https://journals.aps.org/prl/pdf/10.1103/PhysRevLett.13.321>
- [6] D. Gross, F. Wilczek (1973). Ultraviolet Behavior of Non-Abelian Gauge Theories, *Phys. Rev. Letters*, Vol. 30, p. 1343-1346.  
<https://journals.aps.org/prl/abstract/10.1103/PhysRevLett.30.1343>
- [7] D. Spergel (2015). The dark side of cosmology: Dark matter and dark energy, *Science*, Vol. 347, p. 1100-1102.  
<http://science.sciencemag.org/content/347/6226/1100.full>
- [8] A. Djouadi (2007). The Anatomy of Electro-Weak Symmetry Breaking. II: The Higgs bosons in the Minimal Supersymmetric Model, *Physics Reports*, Vol. 459, p. 1-241.  
<https://arxiv.org/pdf/hep-ph/0503173.pdf>
- [9] M. Thomson (2013). *"Modern Particle Physics"*. Cambridge University Press (UK).
- [10] D. Griffiths (2008). *"Introduction to Elementary Particles"*. Wiley-VCH (Germany).
- [11] M. Peskin, D. Schroeder (1995). *"An Introduction to Quantum Field Theory"*. Westview Press (US).

- [12] *Standard Model*, University of Zurich.  
<http://www.physik.uzh.ch/groups/serra/StandardModel.html> (7/4-2017)
- [13] The Super-Kamiokande Collaboration (1998). Evidence for oscillation of atmospheric neutrinos, *Phys.Rev.Lett*, Vol. 81, p. 1562-1567.  
<https://arxiv.org/pdf/hep-ex/9807003.pdf>
- [14] *Why does the Higgs field have a Mexican hat shape?*, Quora.  
<https://www.quora.com/Why-does-the-Higgs-field-have-a-Mexican-hat-shape> (19/4-2017)
- [15] J. Goldstone (1961), Field theories with "Superconductor" solutions, *Il Nuovo Cimento*, Vol. 19, p. 154–164.  
<http://link.springer.com/article/10.1007%2FBF02812722>
- [16] F. Hasert et al. (1973). Observation of neutrino-like interactions without muon or electron in the Gargamelle neutrino experiment, *Physics Letters B*, Vol. 46, p. 138-140.  
<http://www.sciencedirect.com/science/article/pii/0370269373904991>
- [17] G. Arnison et al. (1983). Experimental Observation of Isolated Large Transverse Energy Electrons with Associated Missing Energy at  $\sqrt{s} = 540$  GeV, *Physics Letters B*, Vol. 122, p. 103-116.  
<http://www.sciencedirect.com/science/article/pii/0370269383911772>
- [18] G. Arnison et al. (1983). Experimental observation of lepton pairs of invariant mass around  $95 \text{ GeV}/c^2$  at the CERN SPS collider , *Physics Letters B*, Vol. 126, p. 398-410.  
<http://www.sciencedirect.com/science/article/pii/0370269383901880>
- [19] M. Banner et. al. (1983). Observation of single isolated electrons of high transverse momentum in events with missing transverse energy at the CERN pp collider, *Physics Letters B*, Vol. 122, p. 476-485.  
<http://www.sciencedirect.com/science/article/pii/0370269383916052>
- [20] ATLAS Collaboration (2012). Observation of a new particle in the search for the Standard Model Higgs boson with the ATLAS detector at the LHC, *Physics Letters B*, Vol. 716, p. 1-29.  
<https://arxiv.org/abs/1207.7214>
- [21] CMS Collaboration (2012). Observation of a new boson at a mass of 125 GeV with the CMS experiment at the LHC, *Physics Letters B*, Vol. 716, p. 30-61.  
<https://arxiv.org/abs/1207.7235>
- [22] *The Nobel Prize in Physics 2004*, The Official Web Site of the Nobel Prize.  
[https://www.nobelprize.org/nobel\\_prizes/physics/laureates/2004/popular.html](https://www.nobelprize.org/nobel_prizes/physics/laureates/2004/popular.html) (21/4-2017)

- [23] P. Batzing, A. Raklev (2015). *Supersymmetry*, Lecture notes for FYS5190/FYS9190, University of Oslo.  
<http://www.uio.no/studier/emner/matnat/fys/FYS5190/h15/resurser/notes.pdf>
- [24] S. Martin (2016). *A Supersymmetry Primer*.  
<https://arxiv.org/pdf/hep-ph/9709356.pdf>
- [25] E. Gramstad (2013). *Searches for Supersymmetry in di-Lepton Final States with the ATLAS Detector at  $\sqrt{s} = 7$  TeV*. PhD thesis, University of Oslo.
- [26] M. Pedersen (2014). *Fake lepton determination, Supersymmetry searches in di-lepton final states, and sharing ATLAS research with young students*. PhD thesis, University of Oslo.
- [27] J. Alwall (2009). *Simplified Models for a First Characterization of New Physics at the LHC*.  
<https://arxiv.org/pdf/0810.3921.pdf>
- [28] ATLAS Collaboration (2016). *Reconstruction of hadronic decay products of tau leptons with the ATLAS experiment*.  
<https://arxiv.org/pdf/1512.05955.pdf>
- [29] Particle Data Group (2016). Review of Particle Physics, *Chin. Phys. C*, Vol. 40.  
<http://pdg.lbl.gov/>
- [30] ATLAS Collaboration (2014). *Search for direct production of charginos, neutralinos and sleptons in final states with two leptons and missing transverse momentum in pp collisions at  $\sqrt{s} = 8$  TeV with the ATLAS detector*.  
<https://arxiv.org/pdf/1403.5294.pdf>
- [31] *Pseudorapidity*, Wikipedia.  
<https://en.wikipedia.org/wiki/Pseudorapidity> (31/3-2017)
- [32] E. Halkiadakis (2010). *Proceedings for TASI 2009 Summer School on "Physics of the Large and the Small": Introduction to the LHC experiments*.  
<https://arxiv.org/pdf/1004.5564.pdf>
- [33] A.D. Martin et al. (2009). *Parton distributions for the LHC*.  
<https://arxiv.org/pdf/0901.0002.pdf>
- [34] ATLAS Collaboration (2016). *Measurement of the Inelastic Proton-Proton Cross Section at  $\sqrt{s} = 13$  TeV with the ATLAS Detector at the LHC*.  
<https://arxiv.org/pdf/1606.02625.pdf>
- [35] B. Isildak (2013). *Measurement of the differential dijet production cross section in proton-proton collisions at  $\sqrt{s} = 7$  TeV*.  
<https://arxiv.org/pdf/1308.6064.pdf>
- [36] *About CERN*, CERN. <http://home.cern/about> (5/3-2017)

- [37] OPAL Collaboration (2000). *Precise Determination of the Z Resonance Parameters at LEP: “Zedometry”*.  
<https://arxiv.org/pdf/hep-ex/0012018.pdf>
- [38] G. Baur et al. (1996). Production of antihydrogen, *Physics Letters B*, Vol. 368, p. 251-258.  
<http://www.sciencedirect.com/science/article/pii/0370269396000056>
- [39] ALPHA Collaboration (2011). Confinement of antihydrogen for 1,000 seconds, *Nature Physics*, Vol. 7, p. 558-564.  
<http://www.nature.com/nphys/journal/v7/n7/full/nphys2025.html>
- [40] Tim Berners-Lee’s proposal, CERN.  
<http://info.cern.ch/Proposal.html> (3/5-2017)
- [41] *The Large Hadron Collider*, CERN. <http://home.cern/topics/large-hadron-collider> (11/3-2017)
- [42] *The CERN Accelerator Complex*, CERN.  
<https://cds.cern.ch/record/2197559> (12/3-2017)
- [43] *The accelerator complex*, CERN.  
<https://home.cern/about/accelerators> (12/3-2017)
- [44] *Radiofrequency cavities*, CERN.  
<http://home.cern/about/engineering/radiofrequency-cavities> (11/3-2017)
- [45] *Opinion: LHC smashes targets for 2016 run*, Frédéric Bordry, CERN.  
<https://home.cern/about/opinion/2016/11/lhc-smashes-targets-2016-run-0> (12/3-2017)
- [46] G. Aad et al. (2008). The ATLAS Experiment at the CERN Large Hadron Collider. *Journal of instrumentation*, Vol. 3, S08003.  
<http://iopscience.iop.org/article/10.1088/1748-0221/3/08/S08003>
- [47] CERN Document Server, ATLAS photos - Computer Generated Images.  
<https://cds.cern.ch/search?cc=ATLAS+Photos&p=keyword%3A%22Computer%20Generated%20Images%22> (April-May 2017)
- [48] G. Aad et al. (2008). ATLAS pixel detector electronics and sensors. *Journal of instrumentation*, Vol. 3, P07007.  
<http://iopscience.iop.org/article/10.1088/1748-0221/3/07/P07007/>
- [49] M. Capeans et al. (2010). *ATLAS Insertable B-Layer Technical Design Report*, ATLAS TDR 19, CERN/LHCC 2010-013.  
<https://cds.cern.ch/record/1291633>
- [50] ATLAS Collaboration (2014). *Operation and performance of the ATLAS semiconductor tracker*.  
<https://arxiv.org/abs/1404.7473>

- [51] The ATLAS TRT collaboration (2008). The ATLAS Transition Radiation Tracker (TRT) proportional drift tube: design and performance. *Journal of instrumentation*, Vol. 3, P02013.  
<http://iopscience.iop.org/article/10.1088/1748-0221/3/02/P02013>
- [52] ATLAS Collaboration (2016). *Performance of the ATLAS Trigger System in 2015*.  
<https://arxiv.org/pdf/1611.09661.pdf>
- [53] A. Zlobin (2014). Superconducting Magnets - Principles, Operation, and Applications, *Wiley Encyclopedia of Electrical and Electronics Engineering*, p. 1-19.  
[https://www.researchgate.net/figure/269698566\\_fig14\\_Figure-17-ATLAS-detector-magnet-system-Courtesy-of-CERN](https://www.researchgate.net/figure/269698566_fig14_Figure-17-ATLAS-detector-magnet-system-Courtesy-of-CERN)
- [54] C. G. Lester, D. J. Summers (1999). Measuring masses of semi-invisibly decaying particles pair produced at hadron colliders. *Physics letters B*, Vol. 463, p. 99-103. <https://arxiv.org/abs/hep-ph/9906349>
- [55] C. G. Lester, B. Nachman (2015). *Bisection-based asymmetric MT2 computation: a higher precision calculator than existing symmetric methods*.  
<https://arxiv.org/pdf/1411.4312.pdf>
- [56] A. Barr et al. (2003).  *$m_{T2}$ : the truth behind the glamour*.  
<https://arxiv.org/pdf/hep-ph/0304226.pdf>
- [57] ATLAS Collaboration (2016). *Electron efficiency measurements with the ATLAS detector using the 2015 LHC proton-proton collision data*, ATLAS-CONF-2016-024, CERN.  
<https://cds.cern.ch/record/2157687>
- [58] ATLAS Collaboration (2015). *Muon reconstruction performance in early  $\sqrt{s} = 13$  TeV data*, ATL-PHYS-PUB-2015-037, CERN.  
<https://cds.cern.ch/record/2047831>
- [59] M. Cacciari, G. P. Salam, G. Soyez (2008) *The anti-kt jet clustering algorithm*,  
<https://arxiv.org/pdf/0802.1189.pdf>
- [60] ATLAS Collaboration (2016). *Optimisation of the ATLAS b-tagging performance for the 2016 LHC Run*, ATL-PHYS-PUB-2016-012, CERN.
- [61] ATLAS Collaboration (2016). *Performance of b-Jet Identification in the ATLAS Experiment*.  
<https://arxiv.org/pdf/1512.01094.pdf>
- [62] ATLAS Collaboration (2010). *The ATLAS Simulation Infrastructure*.  
<https://arxiv.org/pdf/1005.4568.pdf>
- [63] S. Agostinelli et al. (2003). GEANT4 - simulation toolkit, *Nuclear Instruments and Methods in Physics Research A*, Vol. 506, p. 250-303.  
<http://www.sciencedirect.com/science/article/pii/S0168900203013688>

- [64] ATLAS Collaboration (2010). *The simulation principle and performance of the ATLAS fast calorimeter simulation FastCaloSim*, ATL-PHYS-PUB-2010-013, CERN.  
<https://cds.cern.ch/record/1300517>
- [65] T. Gleisberg et al. (2009). *Event generation with SHERPA1.1*  
<https://arxiv.org/pdf/0811.4622.pdf>
- [66] ATLAS Collaboration (2016). *Monte Carlo Generators for the Production of a W or Z/ $\gamma^*$  Boson in Association with Jets at ATLAS in Run 2*, ATL-PHYS-PUB-2016-003, CERN. <http://cds.cern.ch/record/2120133>
- [67] T. Gleisberg, S. Höche (2008). *Comix, a new matrix element generator*.  
<https://arxiv.org/pdf/0808.3674.pdf>
- [68] F. Cascioli et al. (2012). Scattering Amplitudes with Open Loops, *Phys. Rev. Letters*, Vol. 108, 111601.  
<https://journals.aps.org/prl/abstract/10.1103/PhysRevLett.108.111601>
- [69] S. Schumann, F. Krauss (2007). *A parton shower algorithm based on Catani-Seymour dipole factorisation*.  
<https://arxiv.org/pdf/0709.1027.pdf>
- [70] S. Höche et al. (2012). *QCD matrix elements + parton showers The NLO case*  
<https://arxiv.org/pdf/1207.5030.pdf>
- [71] R. Ball et al. (2015). *Parton distributions for the LHC Run II*.  
<https://arxiv.org/pdf/1410.8849.pdf>
- [72] R. Ball et al. (2012). *Parton distributions with LHC data*.  
<https://arxiv.org/pdf/1207.1303.pdf>
- [73] ATLAS Collaboration (2016). *Multi-boson simulation for 13 TeV ATLAS analyses*, ATL-PHYS-PUB-2016-002, CERN. <http://cds.cern.ch/record/2119986>
- [74] ATLAS Collaboration (2016). *Simulation of top-quark production for the ATLAS experiment at  $\sqrt{s} = 13$  TeV*, ATL-PHYS-PUB-2016-004, CERN. <http://cds.cern.ch/record/2120417>
- [75] E. Re (2010). *Single-top Wt-channel production matched with parton showers using the POWHEG method*.  
<https://arxiv.org/pdf/1009.2450.pdf>
- [76] ATLAS Collaboration (2016). *Modelling of the  $t\bar{t}H$  and  $t\bar{t}V$  ( $V = W, Z$ ) processes for  $\sqrt{s} = 13$  TeV ATLAS analyses*, ATL-PHYS-PUB-2016-005, CERN. <https://cds.cern.ch/record/2120826>
- [77] T. Sjöstrand et al. (2007). *A Brief Introduction to PYTHIA 8.1*  
<https://arxiv.org/pdf/0710.3820.pdf>

- [78] J. Alwall et al. (2011). *MadGraph 5: Going Beyond*  
<https://arxiv.org/pdf/1106.0522.pdf>
- [79] P. Nason (2004). *A New Method for Combining NLO QCD with Shower Monte Carlo Algorithms.*  
<https://arxiv.org/pdf/hep-ph/0409146.pdf>
- [80] ATLAS Collaboration (2010). *The ATLAS Simulation Infrastructure*  
<https://arxiv.org/pdf/1005.4568.pdf>
- [81] *Data Preparation Check List For Physics Analysis*, ATLAS Data Preparation group.  
[https://twiki.cern.ch/twiki/bin/viewauth/Atlas/DataPreparationCheckListForPhysicsAnalysis#CoreFlags\\_Checks\\_in\\_Run\\_2](https://twiki.cern.ch/twiki/bin/viewauth/Atlas/DataPreparationCheckListForPhysicsAnalysis#CoreFlags_Checks_in_Run_2)
- [82] *SUSY Object Definitions (Rel 20)*, ATLAS SUSY Working group.  
<https://twiki.cern.ch/twiki/bin/view/AtlasProtected/SusyObjectDefinitionsr2013TeV>
- [83] *How To Clean Jets 2016*, ATLAS Jet/Etmiss working group.  
<https://twiki.cern.ch/twiki/bin/view/AtlasProtected/HowToCleanJets2016>
- [84] ATLAS Collaboration (2015). *Selection of jets produced in 13 TeV proton-proton collisions with the ATLAS detector*, ATLAS-CONF-2015-029, CERN.  
<https://cds.cern.ch/record/2037702>
- [85] ATLAS Collaboration (2016). *Jet Calibration and Systematic Uncertainties for Jets Reconstructed in the ATLAS Detector at  $\sqrt{s} = 13$  TeV*, ATLAS-PHYS-PUB-2015-015, CERN.  
<https://cds.cern.ch/record/2028594>
- [86] ATLAS Collaboration (2014). *Tagging and suppression of pileup jets with the ATLAS detector*, ATLAS-CONF-2014-018, CERN.  
<https://cds.cern.ch/record/1700870>
- [87] M. Schönherr, University of Zurich, *SHERPA-2.2.1: overview, developments and usage*. [http://www.physik.uzh.ch/~marek/talks/20160829\\_CERN.pdf](http://www.physik.uzh.ch/~marek/talks/20160829_CERN.pdf)
- [88] S. Höche, S. Prestel (2015). *The midpoint between dipole and parton showers*.  
<https://arxiv.org/pdf/1506.05057.pdf>
- [89] The Fifth Annual Large Hadron Collider Physics conference (LHCPh2017), Timetable.  
[https://indico.cern.ch/event/517784/timetable/#20170515 \(15/5-2017\)](https://indico.cern.ch/event/517784/timetable/#20170515 (15/5-2017))